NON-LINEAR OPTICAL DIAGNOSTICS OF NON-CENTROSYMMETRIC OPTO-ELECTRONIC SEMICONDUCTOR MATERIALS

TORSTEN SCHEIDT

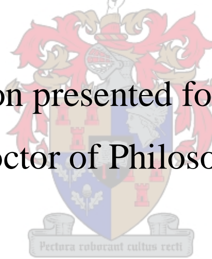

Dissertation presented for the degree
Doctor of Philosophy

University of Stellenbosch

Promoter: Prof. H. M. von Bergmann, University of Stellenbosch
Co-promoter: Dr. E. G. Rohwer, University of Stellenbosch

December 2006

Stellenbosch University http://scholar.sun.ac.za

Declaration

I, the undersigned, hereby declare that the work contained in this dissertation is my own original work and that i have not previously in its entirety or in part submitted it at any university for a degree.

31.03.2006

Signature   Date

Stellenbosch University http://scholar.sun.ac.za

Abstract

Non-linear Optical Diagnostics of Non-centro-symmetric Opto-electronic Semiconductor Materials

Optical second harmonic generation (SHG) is employed to probe the structural properties of the technologically relevant compound semiconductors silicon carbide (SiC), zinc oxide (ZnO) and lead cadmium telluride ($Pb_xCd_{1-x}Te$).
A computer automated experimental setup for SHG experiments is developped involving a commercial femtosecond laser source as well as a custom-built laser pulse diagnostics setup to quantitatively determine the relevant laser pulse parameters (782.8 nm, (75 ± 5) fs, 10 nJ, 80 MHz, TEM_{00}). The second harmonic (SH) intensity is generated in a reflection geometry by the interaction of the sample with the intense femtosecond laser pulses and measured as a function of the azimuthal sample orientation (rotational SH anisotropy) as well as the translational sample position (SH imaging).
SHG measurements performed with SiC thin films grown by chemical vapour deposition (CVD) on silicon prove suitable for polytype recognition. Polarization resolved rotational SH anisotropy measurements in combination with SH imaging identify the investigated SiC films to be the 3C-SiC polytype of homogeneous single-crystalline quality.
As a novel approach, ZnO thin layers grown by metal organic chemical vapour deposition (MOCVD) on three different substrate materials (silicon, amorphous glass and gallium arsenide) are studied by spatially resolved SH imaging. All films show comparable polycrystalline structures (grain size: 30-50 μm) irrespective of the employed substrate material. Furthermore, the SH images recorded with ZnO layers grown on gallium arsenide show that light absorbing amorphous particles are deposited, indicating that the precursor gas phase reaction during the MOCVD growth is not satisfactorily completed. The SH imaging analysis of ZnO thin films deposited with different growth times of 30, 150 and 300 min yielding different average thicknesses (1, 5, 10 μm, respectively) allow statements about the temporal development of the growth process as well as the influence of the reactor tube geometry on the growth efficiency.
$Pb_xCd_{1-x}Te$ wafers grown by the vertical Bridgman method are for the first time investigated by SHG. Consistently with scanning electron microscopy (SEM), SH imaging resolves a segregation within $Pb_xCd_{1-x}Te$ wafers into Pb-rich and Cd-rich

Stellenbosch University http://scholar.sun.ac.za

phases. The latter is found to dominate the SH response of the ternary alloy. Cd-rich microcrystallites embedded in the Pb-rich phase are visualized by SH imaging. Slow cooling rates (2°C/h) during the crystal growth process lead to the coalescence of these microcrystalites resulting in a regular layer-by-layer accomodation of Pb-rich and Cd-rich material. Hence, a periodic alternation of the SH response is observed on the 10 μm length scale, potentially being of technological interest. SH imaging at different azimuthal angles as well as polarization resolved SH imaging visualizes large coherent areas (several mm^2) within the Cd-rich phase, which have equal composition, but enclose an azimuthal SH phase shift of $\sim 30°$. These areas are attributed to macroscopic grains oriented in the (111) and (411) crystalline orientations. SHG, hence proves suitable to obtain spatially resolved mappings of the wafer surface, which are sensitive not only to the sample composition, but also to the crystalline growth orientation.

Overall, the experiments and interpretations presented in this dissertation demonstrate SHG as a powerful and non-destructive probing technique for the structural, morphological as well as non-linear optical properties of novel opto-electronic semiconductor materials.

Stellenbosch University http://scholar.sun.ac.za

Samevatting

Nie-linieêre Optiese Diagnostiek van Nie-Sentro-simmetriese Opto-elektroniese Halfgeleier Materiale

Optiese tweede harmoniese opwekking (THO) is aangewend om die strukturele eienskappe van die tegnologies relevante halfgeleiers silikon karbied (SiC), sink oksied (ZnO) en lood kadmium telluried ($Pb_xCd_{1-x}Te$) te ondersoek.
'n Rekenaar beheerde eksperimentele opstelling vir THO eksperimente is ontwikkel deur gebruik te maak van 'n kommersiële femtosekonde laser bron. 'n Self ontwikkelde opstelling vir laser puls diagnostiek is opgebou om die relevante laserpuls parameters (782.8 nm, (75±5) fs, 10 nJ, 80 MHz, TEM_{00}) te bepaal. Die tweede harmoniek (TH) intensiteit is deur die interaksie van die monster met die intense femtosekonde laserpulse gegenereer en in refleksie gemeet as 'n funksie van die asimutale monster oriëntasie (rotasionele TH anisotropie) sowel as die translasie posisie (TH beeldvorming).
THO metings van SiC dun films wat deur chemiese damp deposisie (CDD) op silikon gegroei is, blyk nuttig te wees om die politipe vas te stel. Polarisasieopgeloste rotasionele TH anisotropie metings in kombinasie met TH beeldvorming kon benut word om die SiC films wat ondersoek is te identifiseer as die 3C-SiC politipe met homogene enkelkristal kwaliteit.
ZnO dunlagies wat deur metaal organiese chemiese damp deposisie (MOCDD) op drie verskillende substrate (silikon, amorfe glas en gallium arseniet) gegroei is, is met die unieke ruimtelik-opgeloste TH beeldvormingstegniek ondersoek. Alle films vertoon vergelykbare polikristallyne strukture (grein grootte: 30-50 μm) ongeag die substraat materiaal. Verder toon die TH beelde wat opgeneem is vir ZnO lagies wat op gallium arseniet gegroei is dat amorfe deeltjies gedeponeer is wat lig absorbeer. Die absorpsie dui dat die voorloper gasfase reaksie tydens die MOCDD groei onvolledig verloop het. Die TH beeldvormingsanalise vir ZnO dun films wat oor verskillende groei tye van 30, 150 en 300 min gedeponeer is, lewer gemiddelde diktes (1, 5, 10 μm, respektiewelik) wat dit moontlik maak om die ontwikkeling van die groeiproses met tyd, asook die invloed van die reaktorbuis se geometrie op die groei effektiwiteit, te ondersoek.
$Pb_xCd_{1-x}Te$ skyfies wat deur die vertikale Bridgman metode gegroei is, is vir die eerste keer deur THO ondersoek. In ooreenstemming met skandeer elektron mikros-

Stellenbosch University http://scholar.sun.ac.za

kopie (SEM), kan die TH beelde die skeiding tussen die Pb-ryke en Cd-ryke fases in die $\mathrm{Pb_xCd_{1-x}Te}$ skyfie oplos. In die Cd-ryke fase van die ternêre allooi is die TH response dominant. Cd-ryk mikrokristalle wat in die Pb-ryk fase gebed is kan deur TH beelde gevisualiseer word. Stadige afkoeltempo's (2°C/h) gedurende kristal groeiproses lei tot die samesmelting van die mikrokristalle wat tot 'n reëlmatige lagie-vir-lagie akkommodasie van Pb-ryke en Cd-ryke materiaal tot gevolg het. 'n Periodiese afwisseling van TH response word waargeneem op 10 μm lengte skaal, wat potensieel van tegnologiese belang kan wees. TH beeldvorming teen verskillende asimutale hoeke asook polarisaie opgeloste TH beeldvorming visualiseer groot koherente gebiede (etlike mm^2) binne die Cd-ryk fase, wat dieselfde samestelling het, maar met 'n asimutale TH fase verskuiwing van $\approx 30°$ toon. Hierdie gebiede word geassosieer met makroskopiese grein oriëntasies in die (111) en (411) kristaloriëntasies. Dit is aangetoon dat THO bruikbaar is om ruimtelik opgeloste kartering van die skyfie oppervlakte te maak wat nie alleenlik sensitief is vir die monster samestelling nie, maar ook vir die kristallyne groei oriëntasie.
Samevattend, die eksperimente en die interpretasies wat in die proefskrif voorgestel is, toon dat THO 'n kragtige en nie-destruktiewe tegniek is om die strukturele, morfologiese sowel as nie-linieêre optiese eienskappe van unieke opto-elektroniese halfgeleier materiale te ondersoek.

Stellenbosch University http://scholar.sun.ac.za

Education is what remains after one has forgotten everything one learned at school.

Albert Einstein

Stellenbosch University http://scholar.sun.ac.za

Contents

Introduction **4**

1 Theoretical Background **7**

1.1 Electromagnetic Wave Propagation in Matter 7

1.2 Nonlinear Polarization 8

1.3 Nonlinear Wave Equation 9

1.4 Second Order Susceptibility Tensor 11

1.4.1 General Symmetry Properties 12

1.4.2 Contracted Notation 12

1.4.3 Spatial Symmetries 14

1.5 Second Harmonic Generation 14

1.5.1 Coupled Wave Equations 14

1.5.2 SHG in Reflection 16

1.5.3 Second Harmonic Rotational Anisotropy 18

1.6 Mathematical Framework of Modelocking 20

2 Experimental Setup and Methods **22**

2.1 The Femtosecond Laser System 22

2.2 Characterization of the Laser Beam 24

2.2.1 Temporal Pulse Duration 24

2.2.2 Spectral Composition 28

2.2.3 Spatial Fluence Distribution 29

2.2.4 Pulse Energy 29

Stellenbosch University http://scholar.sun.ac.za

2.2.5 Summary: Characteristic Laser Beam Parameters 31
2.3 Experimental Setup for SHG 31
2.4 Transverse Beam Radius at Sample: z-Scan 33
2.5 Sample Material 36
2.5.1 Material Properties and Technological Relevance 36
2.5.2 Sample Preparation 37
2.5.2.1 Chemical Vapour Deposition (CVD) 37
2.5.2.2 Vertical Bridgman Crystal Growth 38

3 Experimental Results **39**

3.1 Silicon Carbide (SiC) 39
3.2 Zinc Oxide (ZnO) 42
3.2.1 ZnO on Si(100) 42
3.2.2 ZnO on Glass 46
3.2.3 ZnO on GaAs 49
3.3 Lead Cadmium Telluride ($Pb_xCd_{1-x}Te$) 52
3.3.1 SEM in $Pb_xCd_{1-x}Te$ 52
3.3.2 SHG in CdTe and PbTe 54
3.3.3 SHG in $Pb_xCd_{1-x}Te$ 57
3.3.3.1 SHG in the Pb-rich Phase of $Pb_xCd_{1-x}Te$ 57
3.3.3.2 SHG in the Cd-rich Phase of $Pb_xCd_{1-x}Te$ 59

4 Discussion **63**

4.1 Interpretation of the SiC-Results 63
4.2 Interpretation of the ZnO-Results 65
4.2.1 ZnO on Si(100) 65
4.2.2 ZnO on Glass 67
4.2.3 ZnO on GaAs 68
4.3 Interpretation of the $Pb_xCd_{1-x}Te$-Results 71
4.3.1 SEM in $Pb_xCd_{1-x}Te$ 71

Stellenbosch University http://scholar.sun.ac.za

4.3.2 SHG in CdTe and PbTe 71

4.3.3 SHG in $Pb_{0.20}Cd_{0.80}Te$ 73

4.3.3.1 SHG in the Pb-rich phase of $Pb_{0.20}Cd_{0.80}Te$ 73

4.3.3.2 SHG in the Cd-rich phase of $Pb_{0.20}Cd_{0.80}Te$ 74

Summary and Conclusions **76**

Outlook **79**

Bibliography **81**

Stellenbosch University http://scholar.sun.ac.za

Introduction

Since the discovery of the transistor effect by John Bardeen, Walter Brattain and William Shockley in December 1947 [1–5] the "electronic age" has changed our planet enormously. Hardly any aspect of modern life is not influenced by the presence of electronic means. Some important milestones of the huge progress that has been achieved over the last decades are, for instance, the introduction of television for billions of people, the availability of computers for the private as well as industrial sectors, cell phones and the network coverage across many countries, satellite communication including the global positioning system (GPS), or the development of the internet and the world wide web. Until today the semiconductor fabrication industry is governed by silicon based technology and the number of transistors integrated on a single chip could be doubled approximately every two years as anticipated by Intel's co-founder Gordon Moore. The down-scaling of the size of an average electronic component on a silicon chip has reached the nanometer regime pushing towards the physical limitations. At those length scales a number of fundamental problems occur, for instance, insulating layers consisting of only several ten atom layers cause leakage problems and quantum effects begin to affect the functionality of electronic devices. Enormous research efforts are being conducted to develop alternative technologies. In the field of data storage, for instance, ferroelectric and polymer memory as well as the storage of data-bits in the form of electronic spin states have been proposed, optical methods like holographic memory are under investigation. Also the field of opto-electronics and sensor technology has seen great accomplishments. For instance, the entertainment sector has gained from developments like flat panel displays, CD and DVD players, data projectors or digital cameras. Data transmission by optical fibres is standard in today's telecommunication. Nevertheless, a huge variety of challenges remains also in this field. The manufacture of stable and reliable laser diodes in the green to near ultraviolet spectral region or the development of fast optical switches are only two examples.

Stellenbosch University http://scholar.sun.ac.za

The design and manufacture of future devices based on new technologies requires the development of novel electronic as well as opto-electronic materials. A profound knowledge and understanding of the physical properties of these new materials is necessary in order to control the production processes and achieve sufficiently high material quality as well as errorless operation in newly designed devices. Important issues, particularly in the field of semiconductor materials, are stable growth, defect density, crystalline structure, electronic as well as optical properties.

The need for novel materials and the investigation of their properties has driven the development of a large number of diagnostical techniques. Apart from electrical methods, particle based, or X-ray techniques, microscopy (including scanning electron, atomic force and tunneling microscopy), or spin resonance measurements, also optical techniques represent versatile tools to access a variety of material properties. Particularly, since femtosecond lasers supplying extremely high light intensities are commercially available, nonlinear optical techniques have matured and their applications have spread widely.

Among them optical second harmonic generation (SHG), which was predicted by Göppert-Mayer already in the 1930's [6] and experimentally discovered by Franken *et al.* in 1961 [7], is a powerful, non-invasive and non-destructive probe with *in situ* capability. The investigation of solid materials as well as their surfaces and interfaces by SHG has developped into a wide field of research with a huge amount of exciting results, particularly achieved over the past decade. An impressive number of metallic and semiconducting materials have been studied. For instance, SHG investigations of silver (Ag) [8], copper (Cu) [9, 10] or diamond [11] have lead to detailed statements about the surface electronic band structures. SHG has been used to monitor the molecular beam epitaxy (MBE) growth of gallium arsenide (GaAs) [12] and to analyze different surface reconstructions [13]. Quantum well and dot structures have been subject to SHG investigations [14–17], and detailed knowledge about the structural, electronic as well as nonlinear optical properties of buried interfaces has been obtained by SHG [18]. Here, the most prominent example is the Si/SiO_2 interface [19, 20] due to its outstanding importance in the semiconductor device fabrication industry [21].

SHG is particularly suitable to study non-centrosymmetric crystalline materials, such as many compound semiconductors, the broken inversion symmetry of which yields a non-vanishing electric dipole second harmonic (SH) contribution [22]. For example, SHG is sensitive to the material's composition, morphology, crystalline structure or surface orientation [21]. It has been used to detect different polytypes [23] and is applicable to thin films down to the nanometer length scale.

Stellenbosch University http://scholar.sun.ac.za

This dissertation presents SHG experiments performed with three different non-centrosymmetric material systems. The two binary compounds silicon carbide (SiC) and zinc oxide (ZnO) are both mechanically robust and chemically stable wide band gap semiconductors. This makes them not only interesting candidates for reliable high power and high temperature electronics, but also for applications in photo-luminescence and opto-electronics, such as short wavelength laser diodes, transparent conducting electrodes, waveguides or frequency converters. The third material investigated in this work is the ternary alloy lead cadmium telluride ($Pb_xCd_{1-x}Te$). Due to the different band gap energies of its underlying binary compounds CdTe and PbTe this ternary compound is suitable for band gap engineering by varying the Pb and Cd compositions. This makes it interesting for a variety of photonic applications as well as in the fields of thermophotovoltaics and infrared sensor technology.

The measurements presented in this work and the interpretations thereof demonstrate SHG as a powerful probe to access a number of material properties. Rotational SH anisotropy measurements are employed to identify SiC polytypes and to distinguish between single crystalline and polycrystalline structures.
As a novel approach, two dimensional (2D) SH imaging yields spatially resolved mappings of the structural quality of ZnO thin films at different growth stages, thicknesses and substrate materials. It is suited to resolve the micro-grain size and reveils detailed information about some aspects of the ZnO film deposition process.
SHG experiments are for the first time performed with the novel opto-electronic material $Pb_xCd_{1-x}Te$ as a complementary method to scanning electron microscopy (SEM). SH imaging resolves different crystalline phases within the semiconductor wafer, which show varying Pb and Cd contents. Furthermore, large grains of equal composition, but different crystalline orientation in $Pb_xCd_{1-x}Te$ are successfully detected and visualized by polarization resolved SH imaging and SH imaging at different azimuthal angles.

Overall, this dissertation stands in the context of the optical diagnosis of interesting novel opto-electronic semiconductor materials opening up a large field of applications in modern electronic devices. By using the three material systems SiC, ZnO and $Pb_xCd_{1-x}Te$ the here employed nonlinear optical probing technique SHG is demonstrated as a versatile and effective method to investigate semiconductor compounds. The novel results presented in this work add some interesting and technologically useful contributions to the understanding of the structural, optical and nonlinear optical properties of the investigated materials. Potentially they have direct implications on the optimization of semiconductor growth processes, including both, thin films as well as bulk material.

Stellenbosch University http://scholar.sun.ac.za

Chapter 1

Theoretical Background

The following chapter briefly summarizes the classical theory to describe the propagation of intense laser light in nonlinear dielectric media. The optical nonlinear polarization is introduced and in particular the theoretical description of optical second harmonic generation is presented. Furthermore, the standard mathematical framework describing the principle of modelocking in laser resonators is outlined, since it is of fundamental importance for the generation of intense ultrashort laser pulses, which are required for SHG experiments.

1.1 Electromagnetic Wave Propagation in Matter

In the classical wave picture light is described by the theory of electromagnetism. Maxwell's equations in matter are written in SI-units [24]:

$$\vec{\nabla} \cdot \vec{D} = \rho \tag{1.1}$$

$$\vec{\nabla} \cdot \vec{B} = 0 \tag{1.2}$$

$$\vec{\nabla} \times \vec{E} = -\frac{\partial}{\partial t}\vec{B} \tag{1.3}$$

$$\vec{\nabla} \times \vec{H} = \frac{\partial}{\partial t}\vec{D} + \vec{j} \tag{1.4}$$

Dielectric media are considered, in which no free charge is present ($\rho = 0$) and currents are neglegible ($\vec{j} = 0$). Furthermore, the medium is assumed to be non-magnetic ($\vec{B} = \mu_0 \vec{H}$). Applying these assumptions Maxwell's Eqs. 1.1-1.4 simplify and can be contracted yielding the following wave equation [24]:

Stellenbosch University http://scholar.sun.ac.za

$$\triangle \vec{E} = \mu_0 \frac{\partial^2}{\partial t^2} \vec{D} \tag{1.5}$$

The displacement field in matter is expressed as the sum of the vacuum electric field $\vec{E}$ and the polarization $\vec{P}$ within the respective medium [24].

$$\vec{D} = \epsilon_0 \vec{E} + \vec{P} \tag{1.6}$$

The macroscopic polarization $\vec{P}$ of the medium represents the sum of all microscopic electric dipole moments induced in each atom by the incident electric field $\vec{E}$. As long as the incident field is small compared to inter-atomic fields ($\ll 1\mathrm{V/Å} = 10^8\mathrm{V/cm}$) the polarization $\vec{P}$ is a linear function of the incident field $\vec{E}$. In this case, the atoms are approximated by harmonic oscillators (Lorentz model) and the electrons are assumed to be bound to the nuclei in harmonic potentials.

1.2 Nonlinear Polarization

In the case of femtosecond laser pulses, general incident field amplitudes reaching the order of inter-atomic fields have to be considered, and the above mentioned Lorentz model is no longer applicable [22, 25, 26]. Fig. 1.1 compares the harmonic potential with a typical realistic inter-atomic potential.

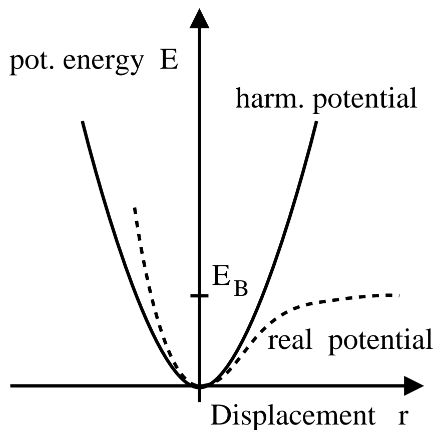

FIGURE 1.1: Comparison of the harmonic potential (Lorentz model) with a typical realistic inter-atomic potential, E_B: binding energy.

The electric field induced oscillations of the electrons in the medium are characterized by the realistic potential curve shown in Fig. 1.1. Consequently, the macroscopic polarization $\vec{P}$ is no longer a linear function of the incident electric field as in the case of the Lorentz model, but must be expanded in higher orders of $\vec{E}$ [22, 25, 26]:

Stellenbosch University http://scholar.sun.ac.za

$$P_i = \epsilon_0 \left(\sum_j \chi_{ij}^{(1)} E_j + \sum_{j,k} \chi_{ijk}^{(2)} E_j E_k + \sum_{j,k,l} \chi_{ijkl}^{(3)} E_j E_k E_l + \dots \right) \quad (1.7)$$

Here P_i represents the ith component of the polarization vector $\vec{P}$. The expansion coefficients $\chi^{(n)}$ are called n^{th} order optical susceptibilities and are tensors of rank $n+1$. Usually, the quadratic and higher order terms are summarized yielding the nonlinear contribution $\vec{P}^{NL}$. The polarization $\vec{P}$ is then expressed as the sum of the linear $\vec{P}^{(1)}$ and nonlinear $\vec{P}^{NL}$ terms:

$$\vec{P} = P^{(1)} + P^{NL} = \epsilon_0 \chi^{(1)} \cdot \vec{E} + \vec{P}_{NL} \quad (1.8)$$

In the special case of isotropic media $\chi^{(1)}$ is reduced to a scalar and related to the refractive index n as well as the absorption coefficient κ as follows:

$$1 + \chi^{(1)} = (n + i\kappa)^2 \quad (1.9)$$

The more commonly used absorption coefficient α is related to κ by $\alpha = 2\kappa\omega/c$.

1.3 Nonlinear Wave Equation

Combining Eqs. 1.6 and 1.8 the dielectric field $\vec{D}$ can be written as:

$$\vec{D} = \epsilon_0 \vec{E} + \vec{P} = \epsilon_0 \vec{E} + \vec{P}^{(1)} + \vec{P}^{NL} = \epsilon_0 (1 + \chi^{(1)}) \cdot \vec{E} + \vec{P}^{NL} = \epsilon_0 \epsilon^{(1)} \cdot \vec{E} + \vec{P}^{NL} \quad (1.10)$$

here $\epsilon^{(1)} \equiv 1 + \chi^{(1)}$ is defined as the first order dielectric tensor.

When Eq. 1.10 is inserted into the wave equation 1.5 the following equation is obtained.

$$\triangle \vec{E} - \frac{\epsilon^{(1)}}{c^2} \frac{\partial^2}{\partial t^2} \vec{E} = \frac{\partial^2}{\partial t^2} \mu_0 \vec{P}_{NL} \quad (1.11)$$

This equation (Eq. 1.11) represents the nonlinear wave equation for lossless, anisotropic, dispersive media. It is the fundamental equation for the theoretical description of the majority of all nonlinear optical effects. It is a second order differential equation and describes the propagation of electromagnetic waves in nonlinear dielectric media.

Stellenbosch University http://scholar.sun.ac.za

The electric field vector representing the incident light pulses can be expressed as the sum over n positive frequency components ω_n, each being the product of a plane carrier wave $e^{i(k_n z - \omega_n t)}$ and an envelope function $E_n(z,t)$ [25]:

$$\vec{E}(z,t) = \sum_n E_n(z,t)\vec{e}_x e^{i(k_n z - \omega_n t)} + c.c. \tag{1.12}$$

An equivalent ansatz is applicable for the nonlinear polarization vector $\vec{P}^{(NL)}$:

$$\vec{P}^{NL}(z,t) = \sum_n P_n^{NL}(z,t) e^{i(k_n z - \omega_n t)} + c.c. \tag{1.13}$$

The propagation direction was chosen to be along the z-axis and k_n are the respective wave vectors.

Often the experimental conditions allow to introduce the so-called 'slowly varying envelope approximation' (SVEA) [22], which allows linearization of the nonlinear wave equation 1.11 yielding a first order differential equation. For incident light frequencies in the visible range, as relevant in the here performed experiments, the carrier frequencies lie in the order of 10^{15} s^{-1}. In contrast to this, the temporal variations of the envelope functions $E_n(z,t)$ take place on a time scale of 10^{-13} s for the laser pulses of $\sim$ 100 fs pulse duration employed here and are, hence, approximately two orders of magnitude slower. Therefore the following approximations are satisfied for the electric field envelope functions:

$$\frac{\partial^2}{\partial t^2} E_n \ll \omega_n \frac{\partial}{\partial t} E_n \tag{1.14}$$

$$\frac{\partial^2}{\partial z^2} E_n \ll k_n \frac{\partial}{\partial z} E_n \tag{1.15}$$

For the nonlinear polarization, where higher harmonics represent the carrier waves, also the first order derivatives of the envelope functions are assumed to be neglegible [27]:

$$\frac{\partial^2}{\partial t^2} P_n^{NL} \ll \omega_n \frac{\partial}{\partial t} P_n^{NL} \ll \omega_n^2 P_n^{NL} \tag{1.16}$$

After the ansatz equations 1.12 and 1.13 are inserted into the nonlinear wave equation 1.11 and the respective derivatives are neglected according to Eqs. 1.14-1.16, it is found that each envelope function $E_n(z,t)$ must satisfy the following first order differential equation:

Stellenbosch University http://scholar.sun.ac.za

$$\left(\frac{\partial}{\partial z} + \frac{n_{\omega_n}}{c}\frac{\partial}{\partial t}\right) E_n(z,t) = i\frac{\omega_n}{2\epsilon_0 n_{\omega_n} c} P_n^{NL}(z,t)e^{-ik_n z} \tag{1.17}$$

Eq. 1.17 represents the linearized form of the general nonlinear wave equation 1.11. It describes the electric field propagation in a nonlinear dielectric medium with the above described approximations (SVEA).

The light intensity employed in the specific experiment determines up to which order the terms of the nonlinear polarization $P_n^{NL}(z,t)$ must be included in Eq. 1.17. The larger the involved electric fields, the more relevant the contributions of the $\chi^{(n)}$ $(n \geq 2)$ terms.

Sum and difference frequency generation, particularly second harmonic generation being a special case thereof, as well as parametric amplification processes are prominent examples for second order ($\chi^{(2)}$) effects, which are also called 3-photon processes. Four wave mixing, frequency tripling, self-phase modulation as well as self-focussing are third order ($\chi^{(3)}$) or 4-photon effects.

1.4 Second Order Susceptibility Tensor

The $\chi^{(2)}$-term in Eq. 1.7 describes optical second harmonic generation, which is a second order nonlinear optical effect and the key method employed in this work to investigate crystalline material systems. Through $\chi^{(2)}$ the second order nonlinear polarization of a medium is expressed in terms of the incident electric field [22, 25]:

$$P_i^{(2)} = \epsilon_0 \left(\sum_{jk} \chi_{ijk}^{(2)} E_j E_k\right) \tag{1.18}$$

Here $P_i^{(2)}$ and E_i are the ith components of the polarization and electric field vectors, respectively. $\chi^{(2)}$ forms a third rank tensor, generally consisting of 27 cartesian components. 12 tensors of rank three are required to fully describe the mutual interaction of three waves of different frequencies ω_1, ω_2 and $\omega_3 = \omega_1 + \omega_2$ [25]. Hence, 324 different complex entries need to be determined. Fortunately, many of these entries are related by symmetry properties drastically reducing the number of independent components of $\chi^{(2)}$.

Stellenbosch University http://scholar.sun.ac.za

1.4.1 General Symmetry Properties

The following general symmetry properties hold for the second order susceptibility tensor $\chi^{(2)}$ [25]:

Time reversal symmetry, due to the requirement that physical fields must be real:

$$\chi^{(2)}_{ijk}(-\omega_n-\omega_m,-\omega_n,-\omega_m)=\chi^{(2)}_{ijk}(\omega_n+\omega_m,\omega_n,\omega_m)^*=0 \tag{1.19}$$

Intrinsic permutation symmetry:

$$\chi^{(2)}_{ijk}(\omega_n+\omega_m,\omega_n,\omega_m)=\chi^{(2)}_{ikj}(\omega_n+\omega_m,\omega_m,\omega_n) \tag{1.20}$$

Full permutation symmetry, applicable in lossless media:

$$\chi^{(2)}_{ijk}(\omega_n+\omega_m,\omega_n,\omega_m)=\chi^{(2)}_{jki}(\omega_m-\omega_n,\omega_m,-\omega_n) \tag{1.21}$$

The time reversal symmetry reduces the number of independent $\chi^{(2)}$-tensor elements to 162. The intrinsic permutation symmetry further decreases the number to 81 parameters and due to the full permutation symmetry only 27 of these independent entries remain.

Usually, the experimental parameters allow the application of the so-called Kleinmann symmetry condition [22, 25]. Here, the frequency of the optical field is assumed to be much smaller than the lowest resonance of the material. This implies that the medium is practically lossless and the nonlinear susceptibility is essentially frequency independent. Using these assumptions, the full permutation symmetry (Eq. 1.21) transforms into the Kleinmann symmetry allowing for index permutation without simultanuous frequency permutation:

$$\begin{aligned}\chi^{(2)}_{ijk}(\omega_n+\omega_m,\omega_n,\omega_m)&=\chi^{(2)}_{jki}(\omega_n+\omega_m,\omega_n,\omega_m)=\chi^{(2)}_{kij}(\omega_n+\omega_m,\omega_n,\omega_m)\\&=\chi^{(2)}_{ikj}(\omega_n+\omega_m,\omega_n,\omega_m)=\chi^{(2)}_{jik}(\omega_n+\omega_m,\omega_n,\omega_m)\\&=\chi^{(2)}_{kji}(\omega_n+\omega_m,\omega_n,\omega_m)\end{aligned} \tag{1.22}$$

1.4.2 Contracted Notation

Particularly for lossless media the second order susceptibility tensor is usually written in contracted form:

Stellenbosch University http://scholar.sun.ac.za

$$d_{il} = \frac{1}{2}\chi^{(2)}_{(ijk)} \tag{1.23}$$

Here it is assumed that $\chi^{(2)}_{ijk}$ is symmetric in the last two indices, which is generally satisfied in the case of second harmonic generation, since $\omega_n \equiv \omega_m$ in Eq. 1.21. The number of independent parameters is thus reduced to 18. The indices j and k are summarized introducing the index l as follows:

$$\begin{array}{lcccccc} jk: & 11 & 22 & 33 & 23,32 & 31,13 & 12,21 \\ l: & 1 & 2 & 3 & 4 & 5 & 6 \end{array} \tag{1.24}$$

The second order nonlinear polarization can then be written as:

$$\begin{bmatrix} P_x^{(2)}(2\omega) \\ P_y^{(2)}(2\omega) \\ P_z^{(2)}(2\omega) \end{bmatrix} = 2\epsilon_0 \begin{bmatrix} d_{11} & d_{12} & d_{13} & d_{14} & d_{15} & d_{16} \\ d_{21} & d_{22} & d_{23} & d_{24} & d_{25} & d_{26} \\ d_{31} & d_{32} & d_{33} & d_{34} & d_{35} & d_{36} \end{bmatrix} \begin{bmatrix} E_x^2(\omega) \\ E_y^2(\omega) \\ E_z^2(\omega) \\ 2E_y(\omega)E_z(\omega) \\ 2E_x(\omega)E_z(\omega) \\ 2E_x(\omega)E_y(\omega) \end{bmatrix} \tag{1.25}$$

When the Kleinmann symmetry condition (Eq. 1.22), which holds in lossless media, is explicitly applied, only 10 of the 18 elements of d_{il} remain as independent entries.

When a fixed coordinate system is introduced with defined propagation and polarization directions of the electric field vector, the polarization of the fundamental as well as the SH frequencies can be expressed in terms of the scalar relationships [25]:

$$P^{(2)}(\omega) = 4\epsilon_0 d_{eff} E(2\omega)E^*(\omega) \tag{1.26}$$

$$P^{(2)}(2\omega) = 2\epsilon_0 d_{eff} E(\omega)^2 \tag{1.27}$$

Here d_{eff} is obtained by evaluating the sum $\sum_{jk}$ in the general equation (Eq. 1.18) for the respective nonlinear medium, electric field and geometry. In reference [28] a general prescription to calculate d_{eff} for the different crystal classes involving different spatial symmetries is described. The following section gives details about the form of d_{il} for specific crystal structures.

Stellenbosch University http://scholar.sun.ac.za

1.4.3 Spatial Symmetries

Generally, crystalline media can be divided in 32 crystal classes [29], showing specific spatial symmetry properties. The form of $\chi^{(2)}$ can be determined for structures of each of these crystal classes. This type of calculation was originally performed by Butcher [30] and relevant results are summarized in [25]. With one exception (PbTe), all semiconductor materials investigated in this study are non-centrosymmetric, i.e. show a broken inversion symmetry. The specific forms of the relevant d_{il}-tensors (Eq. 1.23) are given in the following:

SiC (3-C polytype), GaAs and CdTe: zinc-blende structure (crystal class $\bar{4}$3m)

$$d = \begin{bmatrix} 0 & 0 & 0 & d_{14} & 0 & 0 \\ 0 & 0 & 0 & 0 & d_{14} & 0 \\ 0 & 0 & 0 & 0 & 0 & d_{14} \end{bmatrix} \tag{1.28}$$

ZnO: wurtzite structure (crystal class 6mm)

$$d = \begin{bmatrix} 0 & 0 & 0 & 0 & d_{15} & 0 \\ 0 & 0 & 0 & d_{15} & 0 & 0 \\ d_{31} & d_{31} & d_{33} & 0 & 0 & 0 \end{bmatrix} \tag{1.29}$$

PbTe: rocksalt structure (crystal class m$\bar{3}$m)

$$d_{il} \equiv 0 \quad \forall \{i, l\} \tag{1.30}$$

1.5 Second Harmonic Generation

In the following section the mathematical framework for second harmonic generation is described [22, 25, 26]. SHG is a special case of sum frequency generation with $\omega_1 = \omega_2 = \omega$, $\omega_3 = 2\omega$ and $k_\omega = n_\omega \cdot \omega / c$, $k_{2\omega} = n_{2\omega} \cdot 2\omega / c \neq 2k_\omega$. Fig. 1.2 schematically shows the process SHG involving a second order optical nonlinear medium.

1.5.1 Coupled Wave Equations

When for SHG the scalar relations 1.26 and 1.27 are inserted into the linearized form (SVEA) of the nonlinear wave equation 1.17, a pair of coupled first order

Stellenbosch University http://scholar.sun.ac.za

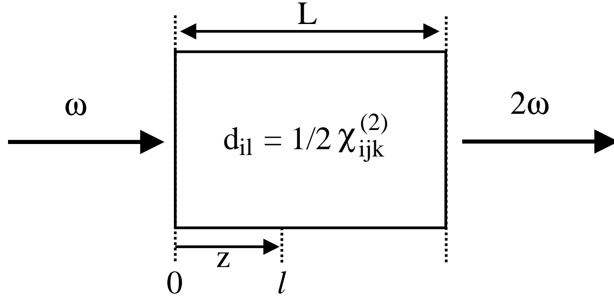

FIGURE 1.2: Schematic representation of second harmonic generation.

differential equations in the envelope functions is obtained for the fundamental and SH frequencies (with $\Delta k = k_{2\omega} - k_\omega$):

$$\left(\frac{\partial}{\partial z} + \frac{n_\omega}{c}\frac{\partial}{\partial t}\right) E_\omega(z,t) = \frac{2i\omega}{n_\omega c} d_{eff} E_{2\omega} E^*_\omega(z,t) e^{-i\Delta kz} \tag{1.31}$$

$$\left(\frac{\partial}{\partial z} + \frac{n_{2\omega}}{c}\frac{\partial}{\partial t}\right) E_{2\omega}(z,t) = \frac{2i\omega}{n_{2\omega} c} d_{eff} E^2_\omega(z,t) e^{i\Delta kz} \tag{1.32}$$

In the following, the case of low SH conversion is considered (UPA: Undepleted Pump Approximation), which is satisfied in the experiments performed here. Thus the electric field envelope $E_\omega(z,t)$ can be assumed to be constant throughout the propagation in the medium. With this assumption Eqs. 1.31 and 1.32 decouple. Using the parameter transformation $t' = t - z/v$, $z' = z$, the development of the SH envelope at a given time t' as a function of the spatial coordinate z' is then described by the differential equation:

$$\frac{\partial}{\partial z'} E_{2\omega}(z',t') = \frac{2i\omega}{n_{2\omega} c} d_{eff} E^2_\omega(t') e^{i\Delta kz'} \tag{1.33}$$

This equation can readily be integrated with the assumption that no SH field is incident on the sample ($E_{2\omega}(z'=0,t') = 0$):

$$E_{2\omega}(z',t') = \frac{2i\omega}{n_{2\omega} c} d_{eff} E^2_\omega(t') \frac{e^{i\Delta kz'} - 1}{i\Delta k} \tag{1.34}$$

Using the time averaged Poynting vector $I = \frac{1}{2}\epsilon_0 cn|E|^2$, the SH intensity can be calculated for a given penetration length l (Fig. 1.2) in the nonlinear medium:

$$I_{2\omega}(l) \propto |E_{2\omega}|^2 = \left(\frac{2\omega \cdot d_{eff}}{n_{2\omega} c}\right)^2 \cdot I^2_\omega \cdot l^2 \cdot \left(\frac{sin(\Delta kl/2)}{\Delta kl/2}\right)^2 \tag{1.35}$$

The term

Stellenbosch University http://scholar.sun.ac.za

$$\left(\frac{sin(\Delta kl/2)}{\Delta kl/2}\right)^2 \tag{1.36}$$

describes the phase mismatch between the fundamental and SH frequencies. For exact phase matching ($\Delta k = 0$) this term is identical to 1 and Eq. 1.35 predicts a purely quadratic relation between the intensity I_ω of the fundamental and the intensity $I_{2\omega}$ of the SH for small penetration lengths l (in agreement with UPA). In the here presented experiments employing SHG in reflection from crystalline surfaces, the penetration length l is in the order of a few micrometers and therefore the phase matching condition ($\Delta kl = 0$) is satisfied.

1.5.2 SHG in Reflection

In order to investigate crystalline semiconductor materials a reflection geometry was chosen for the SHG experiments performed in this study. Thus, the following section presents the here applicable description of SHG in reflection from a linear to nonlinear boundary as it was first derived by Bloembergen [31]. The geometry as displayed in Fig. 1.3 is considered. Medium 1 may either be air (as in the experiments presented here) or an arbitrary optically linear dielectric with dielectric constant ϵ_1, whereas medium 2 represents the optically nonlinear material with dielectric constant ϵ_2. The boundary plane is $z = 0$. All waves, represented by their wave vectors $\vec{k}_j$ and polarization states $\vec{p}_j$, $\vec{s}_j$ are propagating in the $x - z$ plane. The indices $j = i, r, t, s$ represent the i = incident, r = reflected, t = transmitted and s = (inhomogeneous) source waves [31], respectively.

Despite the fact that two refracted fundamental waves are expected for birefringent crystals, for simplicity only one refracted fundamental wave is assumed for this theoretical description. This is experimentally satisfied for cubic nonlinear media and uni-axial crystals, when the plane of incidence contains the optical axis and the incident light wave is, e.g., polarized within this plane.

First the linear optical properties of the boundary are taken into account. The fundamental wave $\vec{k}_i(\omega)$ incident on the interface with an angle θ_i is partially refracted into medium 2 as well as reflected back into medium 1. The respective angles θ_s and θ_r are determined by Snell's law and the electric field amplitudes corresponding to the transmitted and reflected wave vectors $\vec{k}_t(\omega)$ and $\vec{k}_r(\omega)$ can be calculated using the relevant linear Fresnel factors, which are obtained by solving Maxwell's

Stellenbosch University http://scholar.sun.ac.za

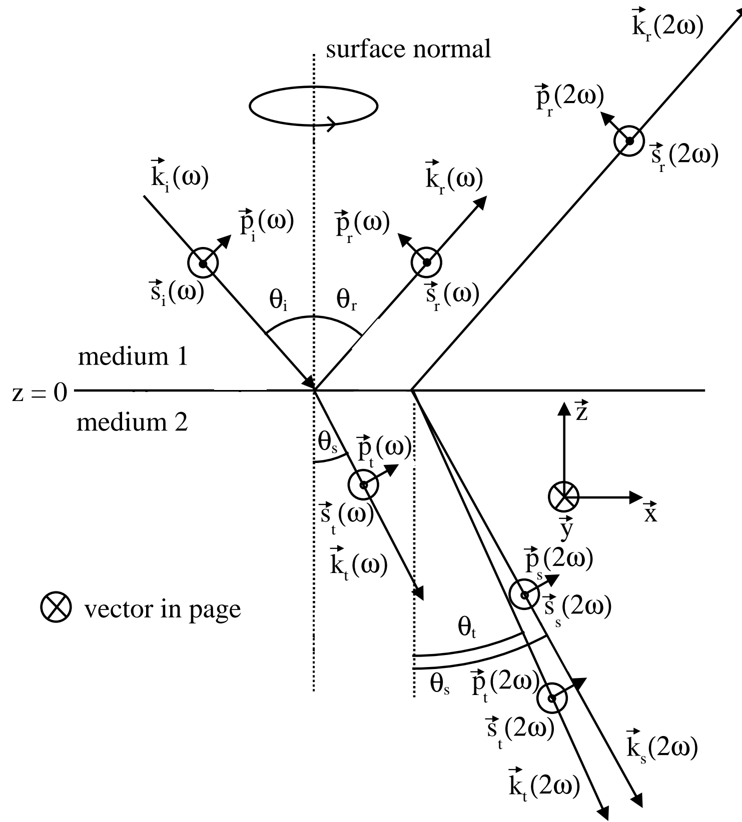

FIGURE 1.3: Geometry of SHG in reflection from a linear to nonlinear boundary [31]. Fundamental wave vectors $\vec{k}_j(\omega)$, polarization states $\vec{p}_j(\omega), \vec{s}_j(\omega)$, second harmonic wave vectors $\vec{k}_j(2\omega)$ ($j = i$ (incident), r (reflected), t (transmitted), s (inhomogeneous source)).

equations (Eqs. 1.1 - 1.4) with the following boundary conditions:

D_{normal}	continuous (no free charge)
$E_{tangential}$	continuous
$B = H$	continuous (non-magnetic media)

The results of these calculations involving the solution of the wave equation (Eq. 1.5) are tabulated in reference [21].

The electric fields of the transmitted and reflected second harmonic waves $\vec{k}_t(2\omega)$ and $\vec{k}_r(2\omega)$ generated at a boundary as shown in Fig. 1.3 are determined in a similar fashion as in the linear case described above. Again Maxwell's equations have to be solved for the SH field with the above boundary conditions after the inclusion of the

Stellenbosch University http://scholar.sun.ac.za

second order nonlinear source term (Eq. 1.18) resulting in the nonlinear wave equation (Eq. 1.11). The solution of this problem resembles the case of linear reflection and refraction. The main difference is, however, that the role of the incident fundamental wave is taken over by the "inhomogeneous source wave" [31] resulting from the nonlinear source term (Eq. 1.18) with an amplitude proportional to $P^{(2)}$. This source wave is denoted with the index s in Fig. 1.3 and points ($\vec{k}_s(2\omega)$) in the same direction as the transmitted fundamental wave ($\vec{k}_t(\omega)$). In general the transmitted homogeneous SH wave vector ($\vec{k}_t(2\omega)$) points in a somewhat different direction and only in the case of exact phase matching ($\Delta k = 0$ in Eq. 1.35) or normal incidence the two waves are parallel. The reflected SH wave ($\vec{k}_r(2\omega)$ in Fig. 1.3), which is detected in the experiments conducted here, originates from the radiation of the "inhomogeneous source wave" [31] caused by the nonlinear polarization (Eq. 1.18) back into medium 1. If medium 1 is air or assumed to be dispersionless the reflected fundamental ($\vec{k}_r(\omega)$) and SH ($\vec{k}_r(2\omega)$) waves point in the same direction. For further mathematical details it is referred to reference [31].

1.5.3 Second Harmonic Rotational Anisotropy

As mentioned above, the linear optical susceptibility $\chi^{(1)}$ is a scalar in cubic media. Therefore linear optical measurements are invariant with respect to different crystal faces or sample orientations. The second order optical susceptibility $\chi^{(2)}$ has higher tensorial rank ($n = 3$) and hence an anisotropic character, which contains structural information about the respective crystalline medium [32]. In general, the SH intensity recorded in the reflection geometry described above depends on the angle of rotation about the surface normal (Fig. 1.3). This azimuthal angular dependence is called rotational SH anisotropy and was first observed by Maker *et al.* [33].

In order to calculate analytic expressions for the reflected SH fields, the components of $\chi^{(2)}$, which are normally given in the crystal coordinate system (Fig. 1.3), must be transformed into the laboratory frame. The solution of this problem is explicitly derived in references [34–36] and [37]. The latter particularly emphasizes zinc-blende type crystals, which are the main subject of this work.
The relative orientations between the crystal and laboratory axes are related by multiple rotations. Hence the transformation of the second order susceptibilty $\chi^{(2)}$ can be described by three successive rotations (angles α, β and ψ) represented by three rotation matrices R^j ($j = 1, 2, 3$). The transformation rule for each rotation is given by:

Stellenbosch University http://scholar.sun.ac.za

$$\chi^{(2)}_{x'y'z'} = \sum_{xyz} R^{j}_{x'x} R^{j}_{y'y} R^{j}_{z'z} \chi^{(2)}_{xyz} \tag{1.37}$$

Here the primed coordinates denote the rotated coordinate system.

The explicit form of the rotation matrix, which represents the azimuthal rotation about the surface normal by the angle ψ is given by [35]:

$$R^{3}_{ij}(\psi) = \begin{pmatrix} cos\psi & -sin\psi & 0 \\ sin\psi & cos\psi & 0 \\ 0 & 0 & 1 \end{pmatrix} \tag{1.38}$$

If the transformation is carried out explicitly [34, 35, 37] with emphasis on the low index crystal orientations (100), (111) and (110) of cubic crystals, the following expressions are obtained for the reflected p- and s-polarized SH fields originating from the bulk nonlinear polarization (Eq. 1.18), which is here assumed to dominate over the surface SH contribution [35]:

$$E^{2\omega}_{g,p}(\psi) \propto \left[a_{g,p} + \sum_{n=0}^{4} b_{g,p} \cos(n\psi) \right] [E^{\omega}_{g}]^{2} \tag{1.39}$$

$$E^{2\omega}_{g,s}(\psi) \propto \left[\sum_{n=1}^{4} b_{g,s} \sin(n\psi) \right] [E^{\omega}_{g}]^{2} \tag{1.40}$$

Here, the Fourier coefficients $a_{g,p}$, $b_{g,p}$ and $b_{g,s}$ are introduced for simplicity. Apart from the independent $\chi^{(2)}$ tensor elements, they summarize the relevant Fresnel factors, which account for the fact that the fundamental field in the nonlinear source term (Eq. 1.18) is that inside the crystal (medium 2 in Fig. 1.3), whereas the SH field is detected outside the crystal (medium 1 in Fig. 1.3). Furthermore, it is mentioned that $b_{g,p} = b_{g,p}(\alpha, \beta)$ and $b_{g,s} = b_{g,s}(\alpha, \beta)$ include the angular functions in the angles α and β arising from the above reference frame transformation. The index $g = p, s$ denotes the p- or s- polarization states of the incident fundamental wave (Fig. 1.3).

Thus, assuming phase matched conditions ($\Delta k = 0$ in Eq. 1.35), the p- and s-polarized SH intensities generated in reflection from the low index faces of bulk cubic media can be expressed as:

$$I^{2\omega}_{g,p} \propto |a_{g,p} + \sum_{n=0}^{4} b_{g,p} \cos(n\psi)|^{2} \cdot (I^{\omega}_{g})^{2} \tag{1.41}$$

Stellenbosch University http://scholar.sun.ac.za

$$I_{g,s}^{2\omega} \propto |\sum_{n=1}^{4} b_{g,s} \sin(n\psi)|^2 \cdot (I_g^{\omega})^2 \tag{1.42}$$

The above relations (Eqs. 1.41 and 1.42) form the basis of the numerical reproduction of the rotational SH anisotropy measurements performed as part of this work.

1.6 Mathematical Framework of Modelocking

The intense ultrashort laser pulses employed in the SHG experiments presented here are generated with a modelocked titanium sapphire oscillator. The following section summarizes the standard mathematical framework describing the principle of modelocking [42].

The light wave oscillations inside the laser resonator take place at a number of frequencies, which are evenly separated as seen in the following relation:

$$\omega_{n+1} = \omega_n + \frac{\pi c}{l} \tag{1.43}$$

where l is the resonator length and c the speed of light. Eq. 1.43 is equivalent to the expression $\omega_n = \omega_0 + n\Delta\omega$ with $\Delta\omega = \pi c/l$ and n an integer. The total multimode oscillation of the field within the laser resonator can thus be expressed by the following superposition of N plane waves:

$$E(t) = \sum_{n=0}^{N-1} E_n e^{i[(\omega_0 + n\Delta\omega)t + \phi_n]} \tag{1.44}$$

It is noted that $E(t) = E(t+T)$ is periodic in $T = 2\pi/\omega = 2l/c$, representing the roundtrip time of the resonator. If the single modes satisfy a fixed phase condition $\phi_n = \phi_0 \ \forall \ n$ (modelocking), the sum in Eq. 1.44 can be evaluated, with the simplifying assumptions $E_n = 1$ and $\phi_0 = 0$, as well as the index transformation $n = 0...(N-1) \rightarrow n = -(N-1)/2...(N-1)/2$:

$$E(t) = \sum_{n=-(N-1)/2}^{(N-1)/2} e^{i(\omega_0 + n\Delta\omega)t} = e^{i\omega_0 t} \frac{\sin(N\Delta\omega t/2)}{\sin(\Delta\omega t/2)} \tag{1.45}$$

Hence, the power output $P(t)$ of a modelocked laser is then given by the expression:

Stellenbosch University http://scholar.sun.ac.za

$$P(t) \propto |E(t)|^2 = \frac{\sin^2(N\Delta\omega t/2)}{\sin^2(\Delta\omega t/2)} \tag{1.46}$$

Fig. 1.4 shows plots of $P(t)$ as a function of time for different total numbers N of laser modes superposed with fixed phase.

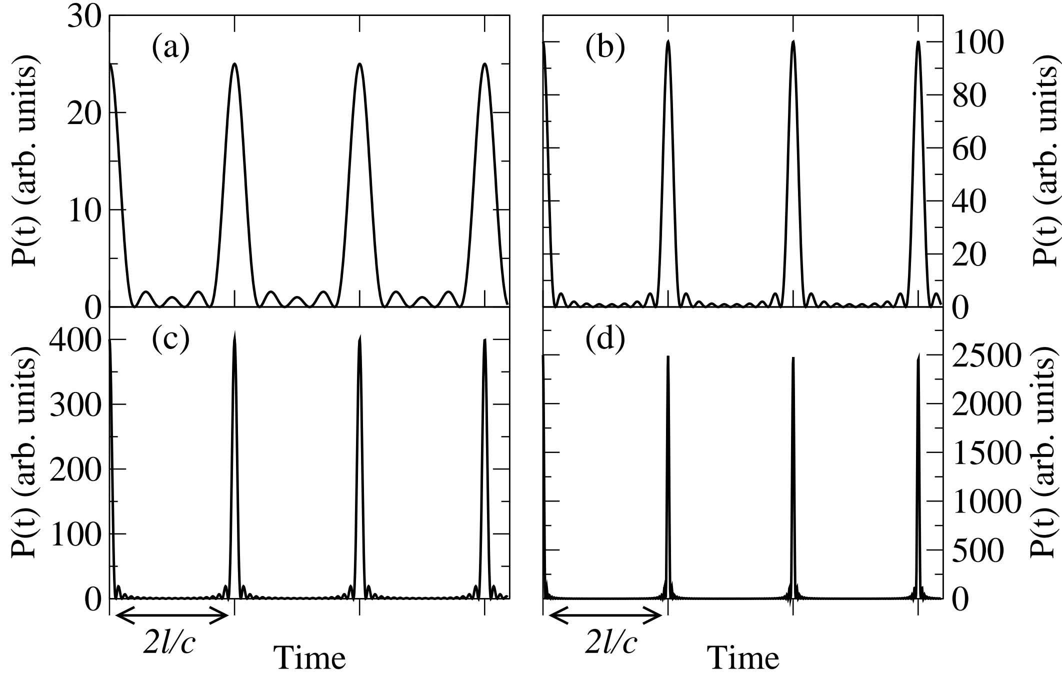

FIGURE 1.4: Modelocked laser output power $P(t)$ according to Eq. 1.46 for different total numbers N of modes superposed with fixed phase condition; (a): $N = 5$, (b): $N = 10$, (c): $N = 20$ and (d): $N = 50$.

The modelocked laser output according to Eq. 1.46 (Fig. 1.4) forms a train of pulses with repetition rate $f_{rep} = 1/T = c/2l$. The power amplitudes of the individual pulses increase drastically with the total number N of phaselocked modes, whereas the temporal pulse durations decrease with N. The number N of phaselocked modes is determined by the width of the gain line shape of the laser medium. The resultant temporal laser pulse duration τ_P is, hence, reciprocally related to the spectral pulse width $\Delta\nu$ by the Fourier theorem. Typical pulse peak intensities generated with modelocked lasers ly in the GW/cm^2 range at pulse durations in the femtosecond regime.

Stellenbosch University http://scholar.sun.ac.za

Chapter 2

Experimental Setup and Methods

In the following chapter the experimental setup is described, which was designed and built during the course of this work and used to perform all SHG experiments presented in this dissertation. In the first section the femtosecond laser system and its working principle is described, the second section deals with the characterization of the laser beam using the laser pulse diagnostics setup developped as part of this work, and the third section gives a detailed overview of the SHG experiment conducted to investigate crystalline semiconductor materials. Lastly, the sample preparation methods employed to produce the investigated materials are briefly outlined.

2.1 The Femtosecond Laser System

The commercial femtosecond laser system (Spectra Physics, USA, Tsunami) used in this work relies on a titanium doped sapphire crystal (Ti:sapphire, or Ti:Al_2O_3) as laser gain medium. As a consequence of strong phonon broadening the fluorescence band of this material covers the spectral range from 660 to 1180 nm with a peak at 795 nm [38]. Since the temporal duration τ_P of a laser pulse and its spectral width $\Delta\nu$ are reciprocally related by the Fourier theorem, the theoretical limit for light pulses generated by the use of Ti:sapphire is 4 fs. Titanium doped sapphire is the most widely used gain material in the field of ultrafast lasertechnology. 5.4 fs laser pulses have been demonstrated with Ti:sapphire based laser oscillators [39]. After external pulse compression temporal pulse durations close to the theoretical limit could be achieved [40].

In Ti:sapphire laser oscillators the constructive superposition of laser modes with

Stellenbosch University http://scholar.sun.ac.za

fixed phase condition (see section 1.6) is achieved by the 'Kerr-Lense-Modelocking' (KLM) [41]. The third order nonlinear optical susceptibility $\chi^{(3)}$ of the Ti:Al_2O_3-crystal yields a refractive index, which is dependent on the intensity I of the light wave propagating through the crystal: $n = n_0 + n_2 I$ (with $n_2 = 3.1 \times 10^{-16} \text{cm}^2/\text{W}$). As a consequence intense laser modes with a given lateral spatial intensity distribution experience a lateral refractive index profile inside the Ti:Al_2O_3-crystal, resulting in selffocussing. Therefore, laser modes randomly interfering constructively inside the resonator show stronger selffocussing compared to modes of lower intensity. This provides a preference criteria for constructively superposed laser modes, which are characterized by a fixed phase condition with respect to each other and result in intense light pulses (section 1.6). The laser oscillator is designed such that low intense modes experience higher losses than constructively superposed laser modes undergoing stronger selffocussing. Consequently, intense light pulses are amplified preferentially and, eventually, low intensity continuous wave modes not satisfying the constructive fixed phase condition die out (SAM: Self Amplitude Modulation). The total number N of constructively superposed laser modes is determined by the width of the laser gain lineshape making Ti:sapphire with its broad fluorescence band particularly suitable as laser active medium for the generation of ultrashort laser pulses.

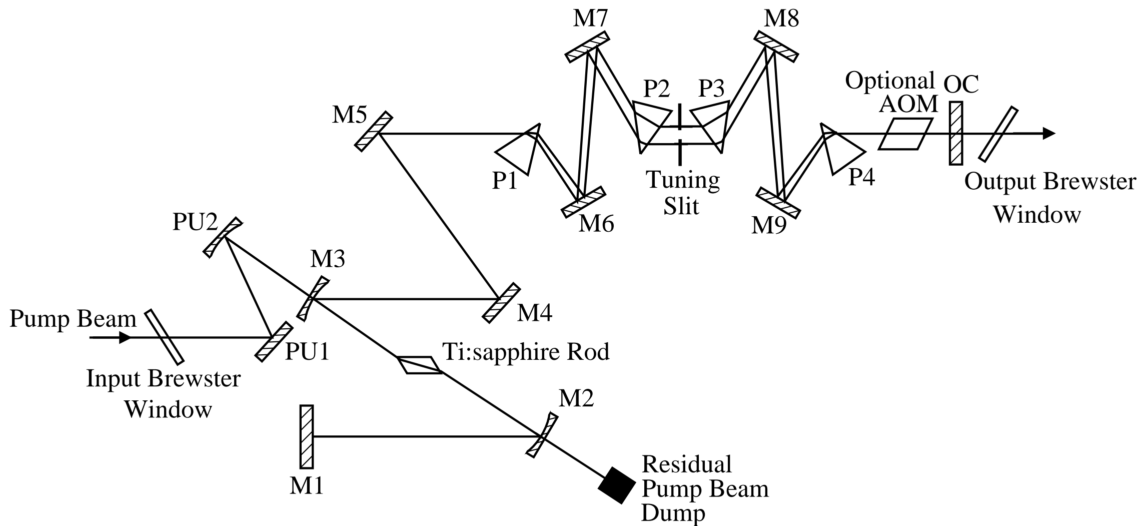

FIGURE 2.1: Configuration of the here-employed Ti:sapphire oscillator.

Due to their broad spectral composition (spectral width $\Delta\nu$) the ultrashort laser pulses experience normal (positive) group velocity dispersion (GVD) induced by the optical elements in the laser resonator. Furthermore, the nonlinear refractive index n_2 of Ti:sapphire leads to an intensity dependent phase shift (SPM: Self Phase

Stellenbosch University http://scholar.sun.ac.za

Modulation) also referred to as frequency chirp [22, 25, 42]. Both, GVD and SPM (for $n_2 > 0$) lead to positive temporal pulse spreading, since blue spectral components are retarded with respect to the red. In order to achieve stable modelocking and minimum pulse durations, positive pulse spreading has to be compensated by the introduction of controllable anomalous (negative) GVD. In the here-employed Ti:sapphire oscillator this is achieved by the implementation of an adjustable set of prism pairs. Fig. 2.1 schematically shows the oscillator configuration. The continuous pump beam of 5.5 W maximum power is delivered by a commercial intra-cavity frequency doubled Nd:YVO_4 laser (Spectra Physics, Millennia V) at a wavelength of 532 nm. The pump light enters through a Brewster window and is directed and focussed into the Ti:sapphire laser rod by the mirrors PU1 and PU2. M2 and M3 are curved dichroic mirrors, highly transmissive for the green pump light and highly reflective for the near infrared (NIR) laser light. M1 is the end mirror of the Ti:sapphire oscillator and P1 - P4 form the prism pairs introducing negative GVD and yielding stable modelocking. The tuning slit of constant width and adjustable position between P2 and P3 is used to select a frequency range and thus allows for frequency tuning of the laser output. After leaving the oscillator through the output coupler OC the laser beam is guided through an output Brewster window to minimize losses of the vertically polarized light. An acousto-optical modulator (AOM) can optionally be used to actively start and stabilize modelocking. The characteristic parameters of the laser output are determined experimentally as discussed in detail in the following section.

2.2 Characterization of the Laser Beam

For any quantitative spectroscopic experiment it is crucial to exactly determine the properties of the probing laser light incident on the sample. In the case of ultrashort laser pulses some of the most important defining parameters are the temporal pulse duration, the spectral composition, the spatial energy distribution as well as the laser pulse energy. These parameters were determined using a laser beam diagnostics setup developed as part of this work and are discussed separately in the following sections.

2.2.1 Temporal Pulse Duration

Electronic measuring techniques are incapable to resolve processes taking place on the femtosecond time scale, since typical time constants for electronic transitions in

Stellenbosch University http://scholar.sun.ac.za

solids (e.g. semiconductor detectors) lie in the picosecond regime. Therefore, optical techniques must be used to determine the temporal duration of femtosecond laser pulses. During the course of this work a so-called autocorrelator was built, which is based on a Michelson interferometer [43] and schematically displayed in Fig. 2.2.

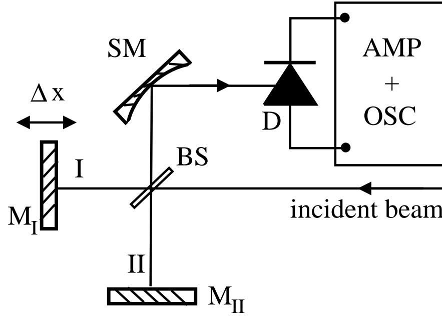

FIGURE 2.2: Schematic of the custom-built autocorrelator, M_I, M_{II}: mirrors, BS: beam splitter, SM: spherical mirror, D: AlGaAs detector diode, AMP: amplifier, OSC: oscilloscope, Δx: optical path length difference.

The incident laser beam falls on the 1:1 beam splitter BS and is divided into the two branches I and II. The back reflections from the mirrors M1 and M2, which are again superposed by the beam splitter are focussed into the AlGaAs light emitting diode (LED) by the spherical mirror SM. The LED is reversed biased and used as a detector [43]. Its band gap energy ($\sim$ 1.9 eV) is larger than the single photon energy of the laser pulses (1.59 eV). Therefore, the laser induced photo current generated in the LED results from two photon absorption (TPA), since single photon absorption is supressed [44].

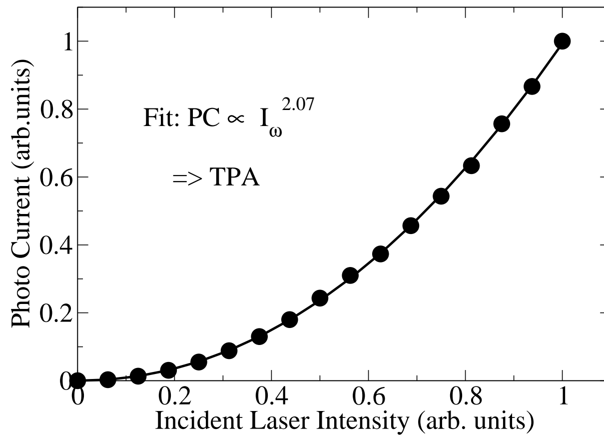

FIGURE 2.3: (Normalized) photo current (PC) of AlGaAs detector diode vs. (normalized) incident laser intensity (I_ω). Filled circles: data points; solid line: fit; approx. quadratic relation; two photon absorption (TPA).

As shown in Fig. 2.3 the measured photo current (filled circles in Fig. 2.3) generated in the AlGaAs diode by pulsed NIR femtosecond irradiation is, in good approximation, a quadratic function of the incident laser fundamental intensity (solid line in Fig. 2.3: fit function $PC \propto I_\omega^{2.07}$). According to Eq. 1.35 (with $\Delta k = 0$) this observation provides experimental evidence for TPA in the AlGaAs diode [44]. For the

Stellenbosch University http://scholar.sun.ac.za

measurement in Fig. 2.3 the photo current was amplified and recorded in a quasi-continuous measurement averaging over the 80 MHz laser pulse repetition rate (see section 2.2.4).

The variation of the optical path length difference Δx between the branches I and II (Fig. 2.2) yielding a time delay $\Delta t = \Delta x/c$ between the splitted pulses I and II leads to an interference pattern in the photo current conventionally referred to as autocorrelation function of the laser pulse. Fig. 2.4 (a) shows a typical autocorrelation measurement of the here-employed femtosecond laser pulses, whereas Fig. 2.4 (b) displays the corresponding numerical data fit.

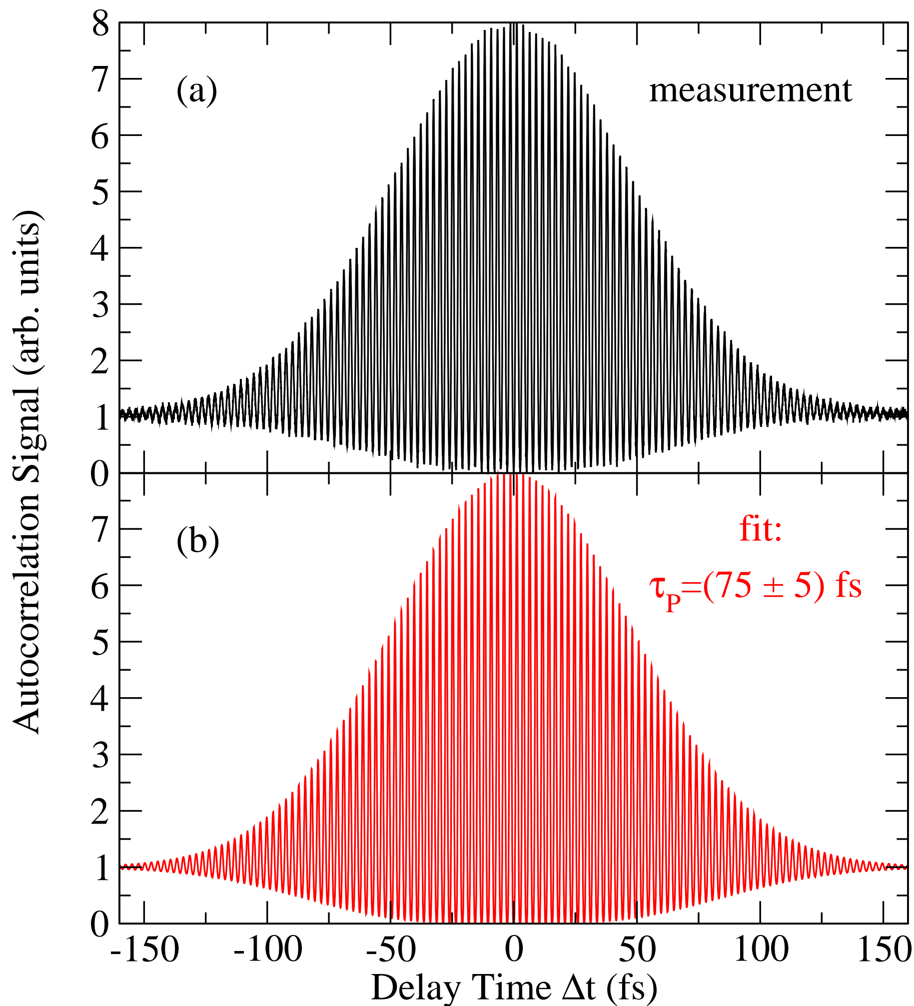

FIGURE 2.4: (a): Measured autocorrelation trace of the Ti:sapphire laser output. (b): Data fit: laser pulse duration (FWHM of intensity envelope): $\tau_P = (75 \pm 5)$ fs.

Fit and experiment are plotted separately for visibility and show very good agree-

Stellenbosch University http://scholar.sun.ac.za

ment. In the following discussion, the fit and its mathematical background are explained in detail yielding the extraction of the femtosecond pulse duration $\tau_P = (75 \pm 5)$ fs (FWHM of intensity envelope).

The numerical fit assumes a sinusoidal carrier wave and a Gaussian envelope function for the incident laser pulse. The electric field functions representing the splitted laser pulses propagating through the branches I and II (Fig. 2.2), which are superposed in the AlGaAs diode can thus be expressed as:

$$E_I(t) = E_I \cdot e^{-2t^2/\tau^2} \cdot \sin(\omega t) \tag{2.1a}$$

$$E_{II}(t - \Delta t) = E_{II} \cdot e^{-2(t-\Delta t)^2/\tau^2} \cdot \sin(\omega(t - \Delta t) + \phi) \tag{2.1b}$$

Here ω is the frequency of the carrier wave. The $1/e$-width of the Gaussian electric field envelope function amounts to $\sqrt{2} \cdot \tau$. The phase shift between the two carrier waves introduced by the dielectric beam splitter is denoted by ϕ and Δt is the time delay between the splitted pulses I and II.
Since two photon absorption takes place in the diode (Fig. 2.3), the measured photo current $PC(\Delta t)$ as a function of the delay time Δt is proportional to the square of the total intenstity $I(\Delta t)$ (Eq. 1.35 with $\Delta k = 0$) incident on the detector integrated over time t, which is written as:

$$PC(\Delta t) \propto I^2(\Delta t) = \int (|E_I(t) + E_{II}(t - \Delta t)|^2)^2 dt \tag{2.2}$$

The right hand side of Eq. 2.2 represents a convolution integral, which can be evaluated after the insertion of Eqs. 2.1a and 2.1b. The result is represented by the curve in Fig. 2.4 (b), which is least square fitted to the experimental data in Fig. 2.4 (a) using an appropriate software package [45]. The carrier wave frequency ω is measured directly (see section 2.2.2). $E_I = E_{II}$, ϕ and τ are fit parameters, which, once extracted, unambiguously determine the electric field function of the laser pulses in Eqs. 2.1a and 2.1b. Conventionally, the temporal pulse duration τ_P is given by the full width at half maximum (FWHM) of the intensity envelope function of the laser pulse. The latter is related to the electric field envelope by $I(t) \propto |E(t)|^2$. For the Gaussian electric field envelope functions as defined in Eqs. 2.1a and 2.1b τ represents the $1/e$-width of the intensity envelope and $\tau_P = \sqrt{\ln 2} \cdot \tau$ (FWHM).

Finally, τ_P is extracted from the fit and amounts to $\tau_P = (75 \pm 5)$ fs for the here employed Ti:sapphire laser source. It should be noted that for vanishing delay time $\Delta t = 0$, destructive interference is observed (Fig. 2.4). This is expected, since the

Stellenbosch University http://scholar.sun.ac.za

employed dielectric beam splitter introduces a phase shift of $\phi = \pi/2$ between the splitted pulses I and II.

The 8/1 ratio between the maximum and offset signals in Figs. 2.4 (a) and (b) can be rationalized by the following relation 2.3, which again accounts for the TPA process in the AlGaAs diode:

$$\frac{PC(\mathrm{max})}{PC(\mathrm{offset})} \propto \frac{I(\mathrm{max})^2}{I(\mathrm{offset})^2} \propto \frac{(|E_I + E_{II}|^2)^2}{(|E_I|^2)^2 + (|E_{II}|^2)^2} = \frac{(2 \cdot E_I)^4}{2 \cdot (E_I)^4} = \frac{16 \cdot (E_I)^4}{2(E_I)^4} = \frac{8}{1} \quad (2.3)$$

$PC(\mathrm{offset})$ denotes the photo current resulting from uncorrelated pulses I and II reaching the detector diode, whereas $PC(\mathrm{max})$ stands for the case of full temporal overlap of the pulses I and II, leading to the fully constructive superposition $E_I + E_{II}$ of the respective electric field amplitudes.

2.2.2 Spectral Composition

Another crucial parameter of the employed laser pulses is the spectral composition. A spectrometer based on a charge coupled device (CCD) array (Ocean Optics HR4000) was used to record and monitor the spectral composition of the Ti:sapphire laser output throughout the entire duration of all experiments performed here. Fig. 2.5 shows a typical laser pulse spectrum corresponding to the autocorrelation trace shown in Fig. 2.4.

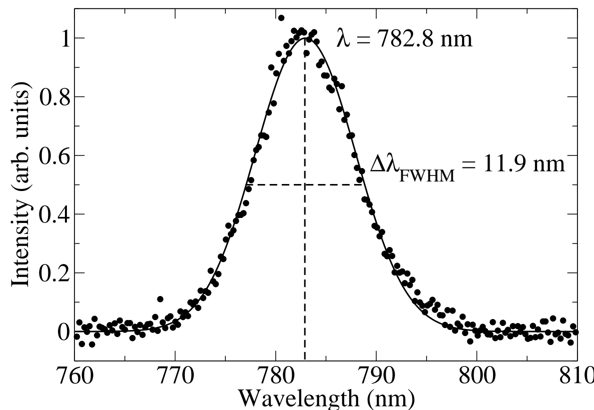

FIGURE 2.5: Recorded spectrum of the Ti:sapphire laser output corresponding to the autocorrelation trace in Fig. 2.4, solid line: Gaussian fit, center wavelength: $\lambda = 782.8$ nm, wavelength band width $\Delta\lambda_{\mathrm{FWHM}} = (11.9 \pm 0.5)$ nm.

The spectrum is well reproduced by a Gaussian fit yielding a center wavelength of $\lambda = 782.8$ nm, which was selected for all experiments presented here, and a wavelength band width of $\Delta\lambda = (11.9 \pm 0.5)$ nm (FWHM). These wavelength values can be transformed into frequencies using the relation $\nu = c/\lambda, \omega = 2\pi\nu$. The center

Stellenbosch University http://scholar.sun.ac.za

frequency, hence, amounts to $\nu = 3.83 \cdot 10^{14}$ Hz ($\omega = 2\pi f = 2.41 \cdot 10^{15}$ s^{-1}) and the time band width product $\tau_P \cdot \Delta\nu$ can be computed yielding the value 0.44 ± 0.04, which is within the experimental error margin equivalent to the theoretical value of 0.44 for band width limited Gaussian pulse shapes.

2.2.3 Spatial Fluence Distribution

The lateral shape of the laser beam profile was measured with a commercial beam profiler (Spiricon SP980M), which relies on a silicon CCD camera. Fig. 2.6 shows a typical result in arbitrary colour coded units recorded of the attenuated laser beam, indicating a close to Gaussian TEM_{00} mode.

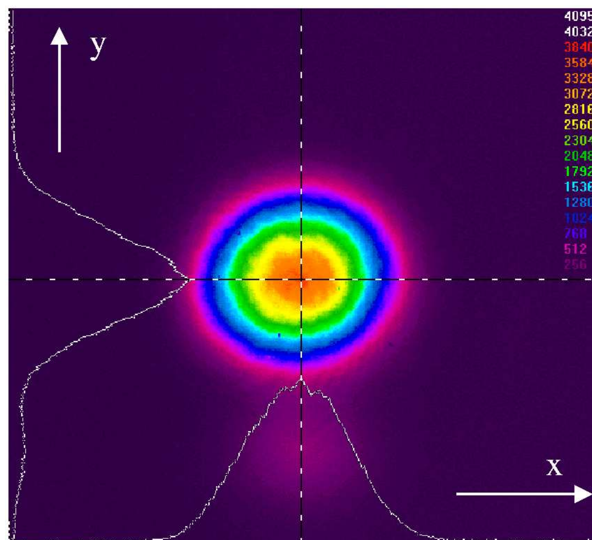

FIGURE 2.6: Lateral fluence distribution of the Ti:sapphire laser output, recorded with a CCD array beam profiler: approximately Gaussian TEM_{00} mode.

The $1/e^2$ beam diameters (intensity envelope) in the x- and y-directions as emitted by the Ti:sapphire oscillator amount to 2.52 and 2.45 mm, respectively, yielding a practically round Gaussian transverse fluence distribution.

2.2.4 Pulse Energy

Since typical repetition rates of modelocked Ti:sapphire oscillators lie in the $10^7 - 10^9$ Hz range, it is impractical to measure the single pulse energy E_P with an energy meter in single pulse mode. The preferred strategy is to record the average power P_{ave} in a quasi-continuous measurement as well as precisely measure the repetition rate f_{rep} of the pulse sequence emitted by the laser source. The single pulse energy can then be determined by the relation $E_P = P_{ave}/f_{rep}$. In order to measure f_{rep} a

Stellenbosch University http://scholar.sun.ac.za

pulse train detector was designed as part of this work using a silicon based photodiode (Infineon BPX 65) with fast response time in the electrical configuration shown in Fig. 2.7.

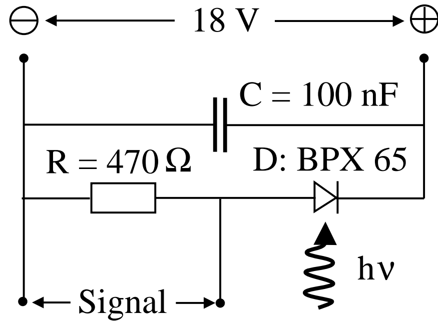

FIGURE 2.7: Electrical configuration of pulse train detector employing fast silicon detector diode BPX 65.

The electrical current signal induced by the laser pulse incident on the reverse-biased photodiode (D) is transformed into a voltage signal using the resistance R. Fig. 2.8 shows a typical pulse sequence measured with the detector shown in Fig. 2.7 and visualized with a standard oscilloscope (Tektronix TDS3022, 300 MHz band width).

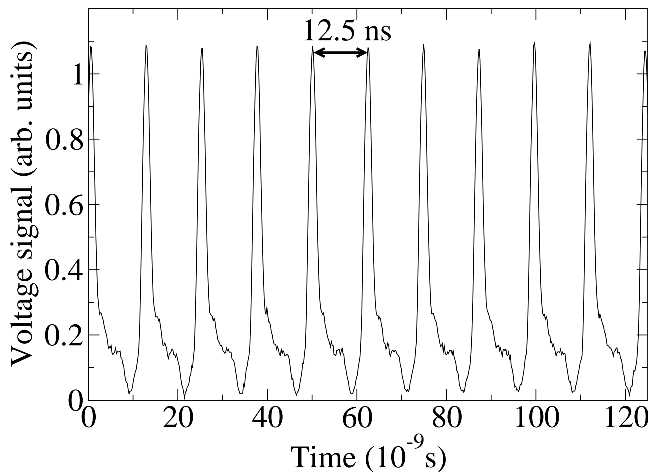

FIGURE 2.8: Pulse sequence of Ti:sapphire laser source measured with pulse train detector shown in Fig. 2.7: pulse-to-pulse time 12.5 ns, $f_{rep} = 80$ MHz.

The pulse-to-pulse time amounts to 12.5 ns yielding a repetition rate of $f_{rep} =$ 80 MHz.

The average power was measured with a standard commercial power meter (Coherent, USA, Field Master with LM-3 power head) yielding a maximum average power of 840 mW as incident on the sample. Hence, the maximum single pulse energy is determined to be 10.5 nJ.

Stellenbosch University http://scholar.sun.ac.za

2.2.5 Summary: Characteristic Laser Beam Parameters

The following table 2.1 summarizes the characteristic parameters of the Ti:sapphire laser source as determined by the experimental techniques described in the previous sections. The listed values are applicable for the laser pulses as incident on the sample.

TABLE 2.1: Characteristic parameters of the employed Ti:sapphire laser source.

Max Average Power	P_{ave}	840 mW
Repetition Rate	f_{rep}	80 MHz
Max Pulse Energy	E_P	10.5 nJ
Minimum Pulse Duration	τ_P	(75 ± 5) fs (FWHM of Intensity Envelope)
Max Pulse Power	P_{max}	130 kW
Center Wavelength	λ	782.8 nm
Spectral Width	$\Delta\lambda$	(11.9 ± 0.5) nm (FWHM at $\lambda = 782.8$ nm)
Time Band Width Product	$\tau_P \cdot \Delta\nu$	0.44 ± 0.04 ($\approx$ theoretical limit)
Max Pump Power	P_{Pump}	5.5 W
Pump Wavelength	λ_{Pump}	532 nm
Radial Mode		$\approx$ TEM_{00}
Polarization		vertical

2.3 Experimental Setup for SHG

During the course of this work the experimental setup to conduct second harmonic generation experiments with semiconductor samples was designed and realized. The diagram in Fig. 2.9 schematically shows the configuration of the experiment. The vertically polarized Ti:sapphire laser output is guided through the $\lambda/2$ retarder plate (B. Halle Nachfolge., Germany,) and the polarizer P1 (Halbo Optics, UK) by the gold mirrors M1 (Edmund Industrial Optics, USA, protective coating, 1/4-wave surface accuracy at 632.8nm). By rotating the $\lambda/2$ plate the laser light intensity incident on the sample can be varied continuously and the polarizer P1 defines the excitation polarization. A red cut-off filter suppresses any second harmonic light possibly generated in the optical elements, avoiding it to reach the sample. The laser

Stellenbosch University http://scholar.sun.ac.za

fundamental is focused onto the sample surface by the achromat lense L1 (Edmund Industrial Optics, USA, NIR anti reflection coated, focal length f = 35 mm)

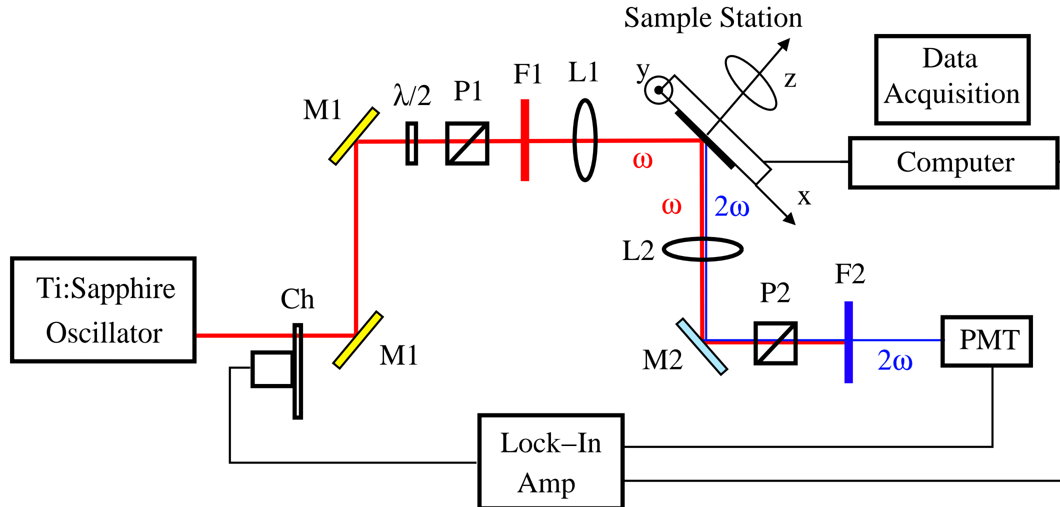

FIGURE 2.9: Schematic diagram of the SHG experiment; CH: light chopper, M1: gold mirrors, $\lambda/2$: retarder plate, P1,P2: polarizers, F1: red cut-off filter, L1,L2: lenses, M2: UV-aluminium mirror, F2: filter combination, PMT: photomultiplier tube, Lock-in technique for noise reduction, computer automated data acquisition.

For all experiments an incident angle of 45° with respect to the surface normal was chosen, as well as a fundamental wavelength of 782.8 nm. The light reflected by the sample is collected by a double convex lense L2 (Edmund Industrial Optics, USA, VIS-NIR anti reflection coated) and guided through the analyzer P2 (Halbo Optics, UK) by the aluminium mirror M2 (Edmund Industrial Optics, UV enhanced aluminium coating, 1/4-wave surface accuracy at 632.8 nm). The filter combination F2 separates the reflected fundamental from the generated SH wave. It comprises of a blue cut-off filter and a bandpass interference filter of 10 nm band width centered at the SH wavelength of 391.4 nm. The SH signal is detected by a photomultiplier tube (PMT) (Hamamatsu R760) in a quasi-continuous measurement integrating over the pulse sequence of 80 MHz repetition rate. A high voltage of 1200 V was applied to the PMT in all experiments. In order to enhance the signal to noise ratio a lock-in amplifier (Ithaco, Dynatrac Model 393) is employed and gated by a 500 Hz light choppper (Ch). The semiconductor sample is mounted on a computer controlled 3D stage (Newport, USA) allowing for sample translation in the x- and y-directions, as well as azimuthal rotation around the z-axis, as indicated in Fig. 2.9. The maximum step resolutions for translations and rotations are 5 μm and 1.8°, respectively. The

Stellenbosch University http://scholar.sun.ac.za

data acquisition is fully computer automated including the control of the sample stage, signal A/D-conversion at a sampling rate of 700 Hz as well as data point averaging and statistical error recording. Suitable laboratory software (National Instruments, USA, Labview) and drivers are employed. The SH signal is either recorded as a function of the x- and y-positions (SH imaging) or of the azimuthal angle (rotational SH anisotropy). The measurements can be performed polarization resolved involving all four polarization combinations between the incident fundamental and recorded SH waves, denoted by p-p, p-s, s-p, and s-s (p = parallel, s = perpendicular with respect to plane of incidence, Fig. 1.3).

2.4 Transverse Beam Radius at Sample: z-Scan

The peak power (P_{max} = 130 kW) of the employed femtosecond laser pulses is determined by the techniques described in section 2.2. The decisive quantity for optical nonlinear processes such as SHG is, however, the peak intensity (Eq. 1.35) of the light pulses incident on the sample. To relate power and intensity, it is, therefore, necessary to precisely measure the beam waist w_0 ($1/e^2$ radius of the transverse intensity envelope) of the laser beam at the sample position, where the laser beam is focused (Fig. 2.9). This is typically achieved by a so-called z-scan measurement, which is described in detail in the following.

In good agreement with the measurement in Fig. 2.6 showing the laser output as emitted by the Ti:sapphire oscillator, the transverse spatial intensity profile can be described by a Gaussian envelope function. Furthermore, considering the geometry illustrated in Fig. 2.10 the fundamental laser intensity incident on the sample can be expressed by the following Gaussian form:

$$I_\omega(x,y) = I_{\omega 0} \cdot \exp(-2x^2/w^2) \cdot \exp(-2\cos^2\theta \ \cdot y^2/w^2) \tag{2.4}$$

Here $\theta = 45°$ is the angle between the incident wave and the sample surface, $I_{\omega 0}$ the intensity at the position $(x = 0, y = 0)$ and $w = w(z)$ the radius of the incident beam at the position z, here defined along the propagation direction of the incident wave (Fig. 2.10).

Conforming with the definition in Eq. 2.4, $w(z)$ is related to the Rayleigh length by [46]:

$$w = w(z) = w_0 \cdot \left(1 + z^2/z_R^2\right)^{1/2} \tag{2.5}$$

Stellenbosch University http://scholar.sun.ac.za

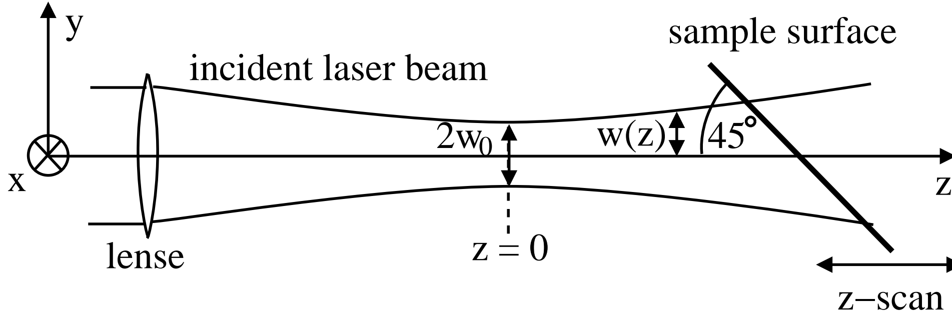

FIGURE 2.10: Geometry and coordinate system appicable for the z-scan measurement, w_0: beam radius at waist position $z = 0$.

where

$$z_R = \pi w_0^2 / \lambda \tag{2.6}$$

holds for the Rayleigh length z_R with $\lambda = 2\pi c/\omega$. The waist radius $w_0 = w(z = 0)$ is the minimum beam radius at the waist position $z = 0$.

The total fundamental power P_ω incident on the sample is computed by evaluating the integral $P_\omega = \iint I_\omega(x, y)dxdy$ yielding:

$$P_\omega = I_{\omega 0} \cdot \frac{\pi w^2}{2\cos\theta} \tag{2.7}$$

According to Eq. 1.35 ($\Delta k = 0$) the generated SH intensity is a quadratic function of the incident fundamental intensity yielding the following expression for the transverse spatial shape of the SH intensity $I_{2\omega}(x, y)$, assuming the form in Eq. 2.4 for the fundamental wave:

$$I_{2\omega}(x, y) = \eta \cdot I_\omega^2(x, y) = \eta \cdot I_{\omega 0}^2 \cdot \exp(-4x^2/w^2) \cdot \exp(-4\cos^2\theta \ \cdot y^2/w^2) \tag{2.8}$$

with η representing the SH conversion efficiency. Integrating $\iint I_{2\omega}(x, y)dxdy$ the total generated SH power is obtained:

$$P_{2\omega} = \eta \cdot I_{\omega 0}^2 \cdot \frac{\pi w^2}{4\cos\theta} \tag{2.9}$$

The comparison of Eqs. 2.7 and 2.9 yields:

$$P_{2\omega} = \eta \cdot P_\omega^2 \cdot \frac{\cos\theta}{\pi w^2} \propto \frac{1}{w^2} \tag{2.10}$$

Stellenbosch University http://scholar.sun.ac.za

Inserting Eq. 2.5 into Eq. 2.10, the SH power $P_{2\omega} = P_{2\omega}(z)$ as a function of the position z is eventually expressed in terms of the Rayleigh length z_R:

$$P_{2\omega} = P_{2\omega}(z) = \eta \cdot P_\omega^2 \cdot \frac{\cos\theta}{\pi w_0^2(1+z^2/z_R^2)} = \frac{K}{1+z^2/z_R^2} \tag{2.11}$$

with $K = (\eta P_\omega^2 \cos\theta)/(\pi w_0^2)$.

Fig. 2.11 shows a typical measurement of the total SH power $P_\omega(z)$, here generated in CdTe, as a function of the sample position z along the propagation direction of the incident fundamental wave. The solid curve is a fit according to Eq. 2.11 with K and z_R as fit parameters. The Rayleigh length is extracted from the fit and amounts to $z_R = 0.17$ mm yielding a beam waist of $w_0 = 6.5$ μm at the focal position $z = 0$ according Eq. 2.6. Thus, the spot diameter amounts to 13 μm with an estimated error bar of ± 2 μm. In all SHG experiments presented here the respective semiconductor sample is positioned at $z = 0$ with the help of a z-scan measurement.

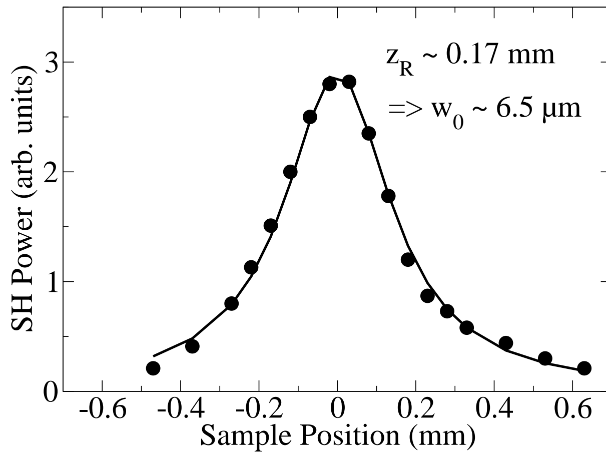

FIGURE 2.11: SH power generated in CdTe as a function of the sample position z along propagation direction of the incident laser beam; solid line: Fit according to Eq. 2.11: Rayleigh length $z_R = 0.17$ mm, beam waist (radius) $w_0 = 6.5$ μm.

Employing Eq. 2.7 the laser peak intensities incident on the sample can finally be related to the pulse peak power applied in the relevant SHG experiment. If the value for the maximum pulse power $P_{max} = 130$ kW (listed in Table 2.1) and the beam radius $w_0 = 6.5$ μm are inserted in Eq. 2.7, the maximum peak intensity value yields $I_{\omega 0} \sim 140$ GW/cm^2. The actual peak intensity values chosen here for the respective SHG experiments usually range between 1 and 20 GW/cm^2 to avoid SH signal saturation or sample damage.

Stellenbosch University http://scholar.sun.ac.za

2.5 Sample Material

In the following section a brief overview is given of the properties of the three semiconductor compounds, silicon carbide, zinc oxide and lead cadmium telluride, investigated in this work. The technological relevance of each material system is put into perspective, and the growth techniques employed to prepare the materials are briefly described.

2.5.1 Material Properties and Technological Relevance

Silicon carbide (SiC) is a wide band gap semiconductor material and, hence, technologically interesting for high power and high temperature applications. Its high radiation damage threshold makes it an attractive candidate for the production of robust electronic devices used under extreme conditions (e.g. in space). Large electro-optical coefficients are expected in SiC, which therefore shows a potential for opto-electronic applications in the visible to ultraviolet spectral region [23]. SiC is chemically inert and thermally as well as mechanically robust. It occurs in over 200 different polytypes, the most important species being 3C-, 2,4,6H- and 15R-SiC. They are characterized by different stacking orders yielding different underlying crystal symmetries (cubic, hexagonal and rhombohedric, respectively). The two most extreme polytypes are 3C with pure cubic stacking of the Si-C bilayers in the (111) direction and 2H showing pure hexagonal stacking in the (0001) direction. 3C- and 2H-SiC have zinc-blende and wurtzite type crystal structures, respectively. The (indirect) energy band gaps of SiC vary between 2.3 eV (3C) and 3.4 eV (2H) [47]. Polytype detection within SiC wafers has been subject to recent research [23] and remains a relevant issue for the fabrication of SiC based electronic devices.

Zinc oxide (ZnO) is a II-VI wide band gap semiconductor. It has a direct band gap of 3.37 eV [50] at room temperature, shows a high chemical stability, and has a high melting point of $\sim$ 2300 K. Apart from its potential for high power electronics, particularly its high exciton binding energy (59-60 meV) [51] and small Bohr radius (18 Å) make it an ideal candidate for opto-electronic applications. Lasing in ZnO thin films at room temperature has been reported [52–56] and it is an important contender in the field of blue-to-UV light emitters [57]. Furthermore, ZnO is suitable for use as a transparent conducting electrode in solar-cell and display applications [58–62] as well as in organic light emitting devices [63, 64]. Despite the use of a variety of growth methods such as pulsed laser deposition (PLD) [65–68], molecular beam epitaxy (MBE) [69, 70] or metal organic chemical vapour deposition

Stellenbosch University http://scholar.sun.ac.za

(MOCVD) [71, 72], the deposition of thin ZnO films of homogeneous quality is still a main issue [73].

In contrast to SiC and ZnO, the third material system under investigation, lead cadmium telluride ($Pb_xCd_{1-x}Te$), is a ternary semiconductor compound. Due to the different band gap energies of the underlying binary compounds CdTe and PbTe of 1.49 eV (direct) and 0.3 eV (indirect), respectively, this material is suitable for band gap engineering by varying the Pb_x and Cd_{1-x} contents. For x=0.79 an ideal band gap for the use in thermophotovoltaic applications can be expected [74]. Furthermore, considering the different refractive indices of the binary compounds (2.8 and 5.5 for CdTe and PbTe, respectively) as well as different second-order optical coefficients, $Pb_xCd_{1-x}Te$ layer structures may be of great interest for a variety of photonic applications, such as gratings, waveguides or dispersive layer systems. Despite the similar lattice parameters (6.481 Å for CdTe and 6.459 Å for PbTe), the synthesis of homogeneous bulk $Pb_xCd_{1-x}Te$ is problematic and subject to current research [75, 76].

2.5.2 Sample Preparation

All sample materials investigated in this study are manufactured in collaborating research laboratories. Chemical vapour deposition (CVD) is employed to produce thin semiconductor films and the vertical Bridgman method (VBM) is used to grow bulk semiconductor crystals of various compositions.

2.5.2.1 Chemical Vapour Deposition (CVD)

The widely used technique chemical vapour deposition [77, 78] generates thin films of material on a substrate by the use of chemical reactions. Reactive gases called precursors, which are often diluted in an inert carrier gas, are fed into a vacuum chamber. They react on the surface of a heated substrate forming a thin film of solid material. The adsorption and decomposition of the precursor molecules at the substrate surface as well as the formation of chemical bonds strongly depend on the growth parameters, such as the ratio of the precursor gases, the gas flow rates, the temperature, or the geometry of the growth reactor. The properties of the substrate, such as structure, surface orientation or roughness also have an important influence on the layer formation. It is, therefore, desirable to relate the film quality to the decisive parameters controlling the production process. With the help of powerful diagnostical methods, such as SHG, the material growth processes can be optimized.

Stellenbosch University http://scholar.sun.ac.za

The silicon carbide (SiC) thin film samples, studied here mainly for calibration purposes and reproducability tests, were supplied by a collaborating research group[1]. They were grown by CVD on silicon of (100) surface orientation at 1600°C and showed an average thickness of $\sim$ 4.9 μm.

The zinc oxide (ZnO) thin films investigated in this study were also supplied by collaborating researchers[2]. They were grown by metal organic chemical vapour depostion using diethyl zinc (DEZ) and *tert*-butanol (TBOH) as precursor gases [73]. The substrate temperature was kept at 450°C and a growth rate of $\sim$ 2 μm/hr was chosen. ZnO layers were deposited on crystalline silicon cut in the (100) surface direction, amorphous glass as well as crystalline GaAs of (100) surface orientation.

2.5.2.2 Vertical Bridgman Crystal Growth

In contrast to the thin film chemical vapour deposition described above, the vertical Bridgman method (VBM) [79, 80] is used to grow bulk semiconductor rods of large size ($\geq$ several cm), which are subsequently cut into wafers and polished. The source materials are melted, homogenized, usually in an oscillating furnace, and solidified in a process tube applying a well defined and controlled temperature gradient.

The lead cadmium telluride ($Pb_xCd_{1-x}Te$) ternary alloys investigated in this work were grown by collaborating researchers[3] using VBM. They were prepared from premixed and melted Cd (6N+), Te (6N+) and Pb (6N). Crystal growth was performed at a solidification speed of 1 mm/h, with a maximum temperature of 1120°C and a vertical temperature gradient of 5°C/cm [75]. For the wafers studied here nominal lead concentrations of x = 0.20 were chosen. Crystal wafers were cut perpendicular to the growth direction and mechanically polished. A Br_2-ethylene glycol solution (2%) was used for further chemical polishing to optical quality. The basic binary compounds CdTe and PbTe investigated here were grown by the same collaborating group[3], also employing the vertical Bridgman method under comparable growth conditions as $Pb_xCd_{1-x}Te$.

[1] H. Stafast *et al.*, Institut für Physikalische Hochtechnologie, P.O. Box 100239, D-07702 Jena, Germany

[2] A. W. R. Leitch, O. Pagni, Nelson Mandela Metropolitan University, Department of Physics, P.O. Box 77000, Port Elizabeth 6031, South Africa

[3] E. Saucedo *et al.*, Departamento de Físika de Materiales, Universidad Autónoma de Madrid, Madrid 28049, Spain

Stellenbosch University http://scholar.sun.ac.za

Chapter 3

Experimental Results

The experimental results are presented in three sections, each dealing with the SHG experiments performed with a specific material system. The first section focuses on the SHG experiments performed with SiC thin films deposited on silicon. The second section deals with the SHG analysis of ZnO layers of various thicknesses grown on different substrates, and the third section presents comparative SHG and SEM (scanning electron microscopy) results obtained with $Pb_xCd_{1-x}Te$ ternary alloys as well as the underlying binary compounds CdTe and PbTe.

3.1 Silicon Carbide (SiC)

The SiC thin films investigated in this study are grown by CVD on a silicon substrate of (100) surface orientation at a growth temperature of 1600°C by a collaborating research group[1]. The average thickness of the SiC films is approximately 5 μm.

Fig. 3.1 displays the SH intensity generated in a SiC thin film recorded in the (p-p) polarization combination between excitation and detection as a function of the incident fundamental intensity, the latter being determined as described above (sections 2.2 and 2.4). The solid line in Fig. 3.1 represents a numerical fit using the function $I^{2\omega} = (I^{\omega})^{1.9}$. In the regime below ~ 4 GW/cm^2 the SH intensity appears to be an approximately quadratic function of the incident fundamental laser peak intensity, which is experimental evidence for pure SHG (Eq. 1.35). For incident intensities above 4 GW/cm^2 the SH signal deviates from the quadratic relation indicating that the SH conversion process begins to saturate. For the incident intensity value of

[1] H. Stafast *et al.*, Institut für Physikalische Hochtechnologie, P.O. Box 100239, D-07702 Jena, Germany

Stellenbosch University http://scholar.sun.ac.za

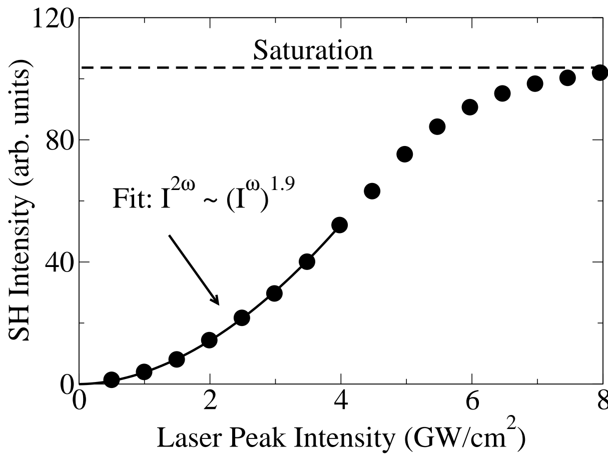

FIGURE 3.1: SH intensity generated in a SiC film (4.9 μm thickness, on Si(100) substrate) as a function of the incident laser peak intensity; solid line: numerical fit: approx. quadratic relation (Eq. 1.35) below $\sim$ 4 GW/cm^2, full saturation above $\sim$ 8 GW/cm^2.

$\sim$ 8 GW/cm^2 full saturation occurs. To ensure well defined unsaturated SH conversion, the following SHG experiments in SiC are conducted at incident intensities well below 4 GW/cm^2.

Fig. 3.2 displays a 2D SH image of a 3 mm $\times$ 3 mm area of a 4.9 μm thickness SiC film grown on Si(100), which is obtained by recording the SH intensity as a function of the (x,y)-sample position (see Fig. 2.9).

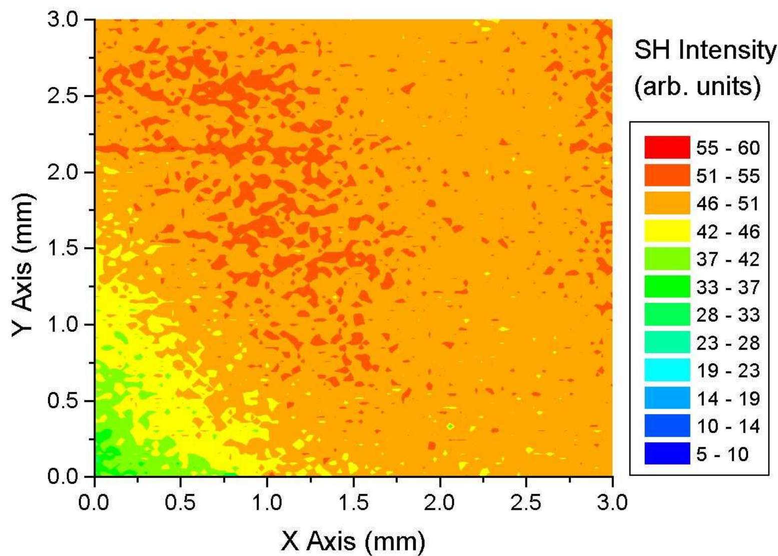

FIGURE 3.2: 2D SH image of SiC thin film (4.9 μm): 3 GW/cm^2 incident laser peak intensity, 30 μm step resolution, (p-p) polarization combination: uniform SH response of single crystalline SiC (3-C polytype).

The translational step size was chosen to be 30 μm in the x- and y-directions and

Stellenbosch University http://scholar.sun.ac.za

the incident laser peak intensity was 3 GW/cm^2. Again the (p-p) polarization combination was selected between excitation and detection. A relatively uniform SH response throughout the entire area is observed. The variations of the SH signal height remain within 10% throughout most parts of the thin SiC film.

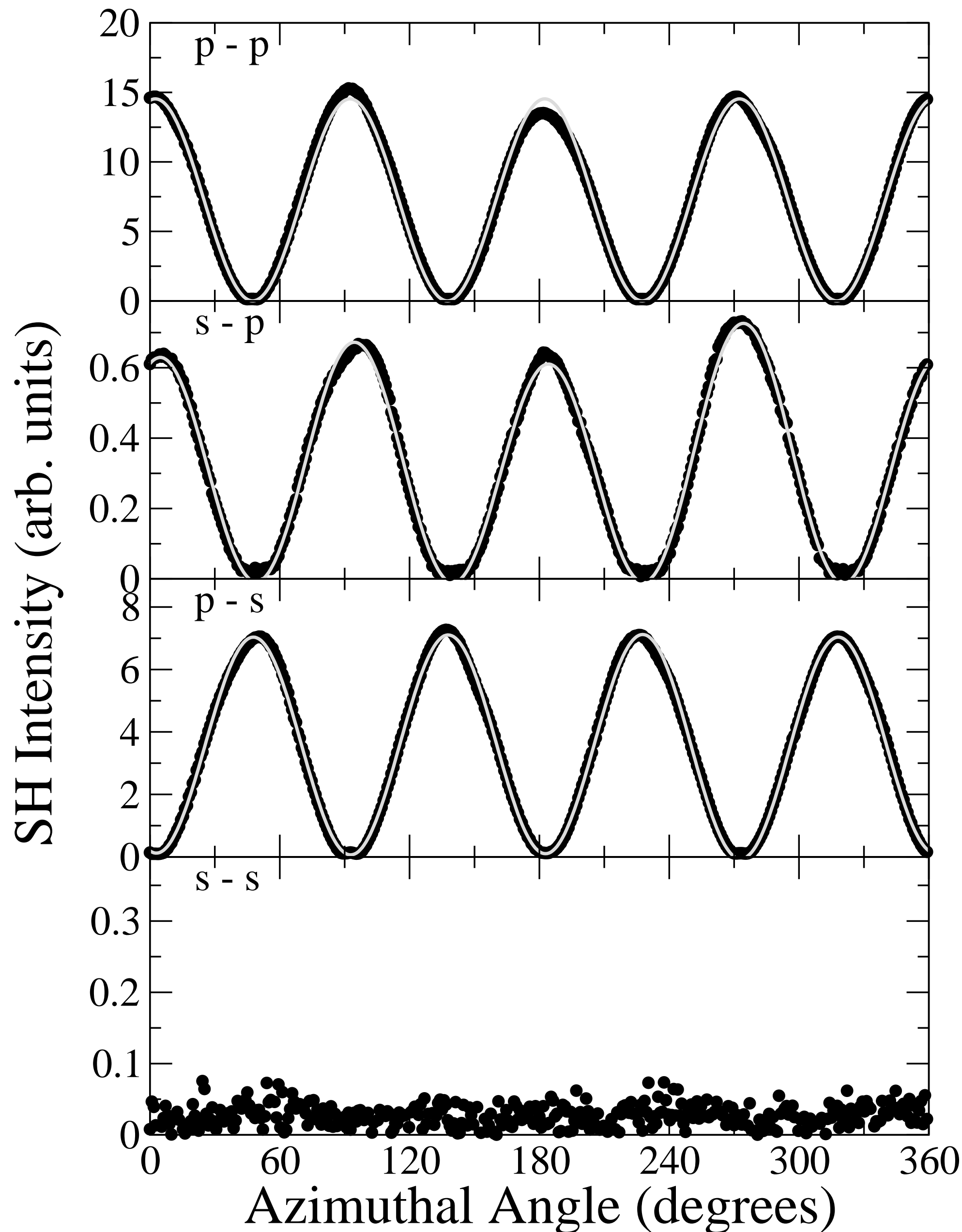

FIGURE 3.3: Rotational SH anisotropy pattern of 4.9 μm thick SiC grown on Si(100) recorded in the four polarization combinations (p-p), (s-p), (p-s) and (s-s) at ~ 0.6 GW/cm^2; solid line: fit according to Eq. 4.1, 3-C polytype.

Stellenbosch University http://scholar.sun.ac.za

To obtain information about the symmetry properties of the SiC polytype under investigation, rotational SH anisotropy measurements are performed as displayed in Fig. 3.3. Here the SH intensity is recorded as a function of the azimuthal sample angle (see Fig. 2.9), and the incident laser peak intensity is chosen to be 0.6 GW/cm^2. A clear 4-fold symmetry is observed in the (p-p), (s-p) and (p-s) polarization combinations. The intensity maxima are separated by exactly 90° and occur at identical azimuthal angles for the p-output polarizations (p-p) and (s-p). An azimuthal phase shift in the rotational SH anisotropy of 45° is observed in the (p-s) polarization relative to the (s-p) polarizaion combination. The SH signal vanishes in the case of perpendicularly polarized excitation as well as detection (s-s). The grey solid lines in Fig. 3.3 are fitting curves according to Eq. 4.1 (section 4.1).

As discussed in section 4.1, the here investigated SiC thin film is identified to be a 3-C polytype of high single crystalline quality throughout the sample area. The measurements presented above confirm and fully agree with results reported earlier in the literature [23, 48].

3.2 Zinc Oxide (ZnO)

The ZnO samples investigated in this study are supplied by a collaborating research group[2]. The films of various thicknesses were grown by MOCVD on three different substrate materials. In the following, the SHG results obtained from ZnO layers deposited on crystalline silicon (centrosymmetric diamond-like structure), amorphous glass and as well GaAs (non-centrosymmetric zinc-blende structure) are presented in separate sections.

3.2.1 ZnO on Si(100)

In a first step the SHG process in ZnO layers is investigated as a function of the incident laser peak intensity for films of different thicknesses grown on silicon of (100) surface orientation. Since the diamond-like crystalline structure of silicon is centrosymmetric, dipole SH contributions originating from the bulk substrate are parity forbidden [36]. The SH signal heights expected from higher order bulk and surface SH contributions for silicon are well known [21, 81, 82] and at least two orders of magnitude weaker than the SH signal generated in the non-centrosymmetric ZnO

[2] A. W. R. Leitch, O. Pagni, Nelson Mandela Metropolitan University, Department of Physics, P.O. Box 77000, Port Elizabeth 6031, South Africa

Stellenbosch University http://scholar.sun.ac.za

layers (wurtzite crystal structure). Interferences between substrate- and ZnO-SH contributions are, therefore, not expected and background corrections accounting for the SH signal originating from the substrate material are unnecessary.

Fig. 3.4 displays the intensity dependence of the SH signal on the incident laser peak intensity for the ZnO films grown on Si(100) within 30 min, 150 min and 300 min, yielding average thicknesses of 1, 5 and 10 μm, respectively.

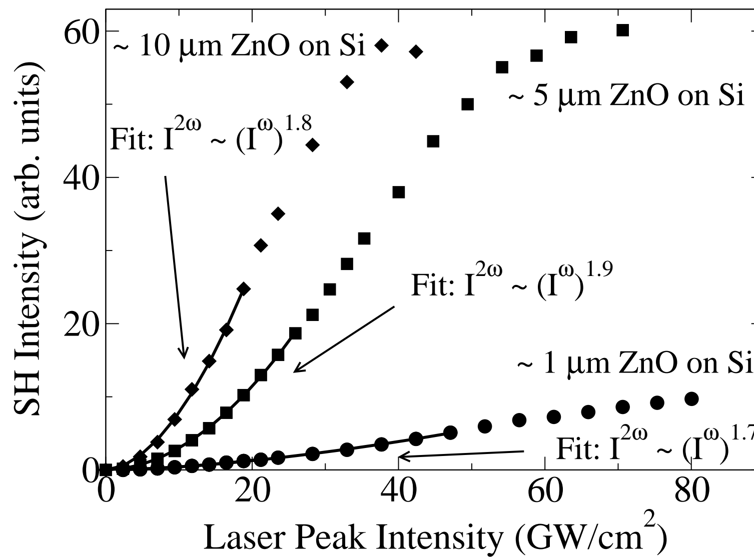

FIGURE 3.4: SH intensity as a function of the incident laser peak intensity for ZnO films of 1, 5 and 10 μm average thickness grown on Si(100); solid lines: fitting curves: approx. quadratic relations below ~45, ~30, ~20 GW/cm^2, saturation intensities ~90, ~65, ~35 GW/cm^2, respectively.

As indicated by the fit functions (solid lines in Fig. 3.4), for relatively low incident intensities an approximately quadratic relation is observed for all three different film thicknesses, confirming pure SHG (Eq. 1.35). The measured SH intensities begin to deviate from this quadratic relation for incident intensities above $\sim$ 45, $\sim$ 30 and $\sim$ 20 GW/cm^2 and full saturation is observed for intensities $>$ 90, 65 and 35 GW/cm^2, respectively. In the SHG experiments presented in the following incident intensities of 12.5 GW/cm^2 are chosen ensuring pure SH conversion in all films.

The following three figures (Figs. 3.5, 3.6 and 3.7) present SH images of ZnO films grown by MOCVD within 30 min, 150 min and 300 min (average thicknesses of 1, 5 and 10 μm), respectively. All SH images show sample areas of 3 mm by 3 mm and are recorded with a step resolution of 30 μm.

Stellenbosch University http://scholar.sun.ac.za

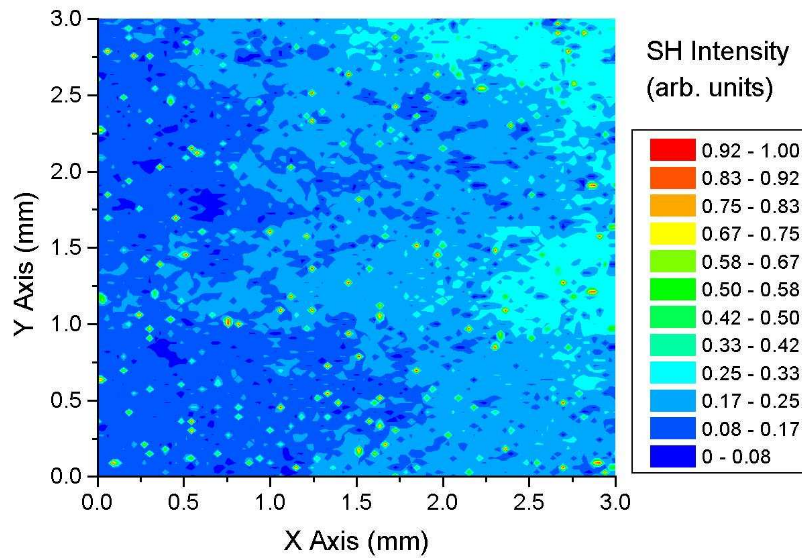

FIGURE 3.5: SH image of a ZnO film grown on Si(100) within 30 min (average thickness $\sim 1\ \mu$m), 12.5 GW/cm^2 laser peak intensity, 30 μm step resolution.

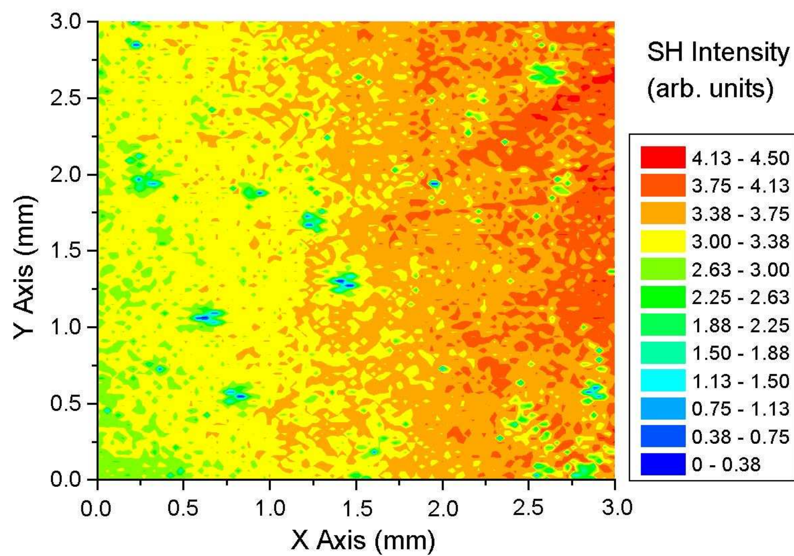

FIGURE 3.6: SH image of a ZnO film grown on Si(100) within 150 min (average thickness $\sim 5\ \mu$m), 12.5 GW/cm^2 laser peak intensity, 30 μm step resolution.

Stellenbosch University http://scholar.sun.ac.za

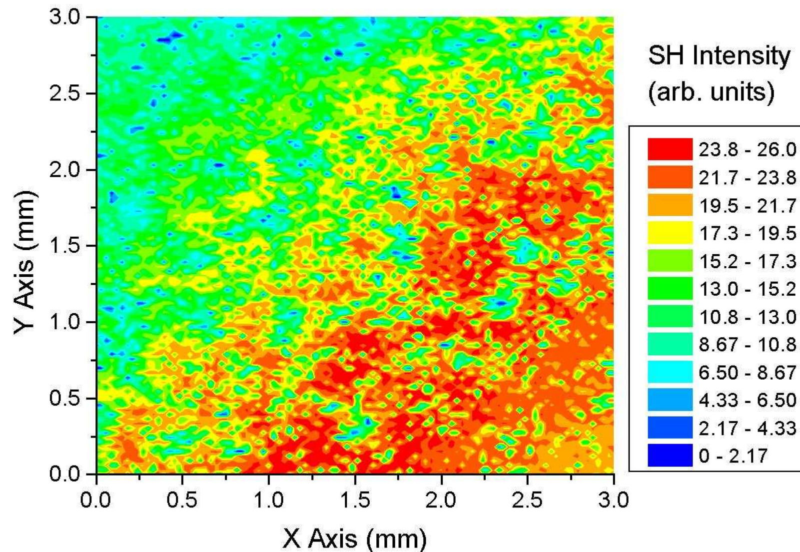

FIGURE 3.7: SH image of a ZnO film grown on Si(100) within 300 min (average thickness $\sim$ 10 μm), 12.5 GW/cm^2 laser peak intensity, 30 μm step resolution.

Comparing the above three SH images it is found that, irrespective of the growth times and average film thicknesses, all ZnO layers show a strongly position dependent, non-uniform SH response. The SH image in Fig. 3.5 (30 min growth time) resolves single crystallites or grains, $\sim$ 30-50 μm in size, randomly distributed throughout the substrate surface, showing a strong SH response. In Fig. 3.6 (150 min growth time) a more extensive ZnO surface coverage is found characterized by SH signal heights approximately 5 times higher than in Fig. 3.6. Isolated microcrystals are hardly visible. In the SH image of the thickest ZnO film (300 min growth time) in Fig. 3.7 the SH signal amplitudes are again about 5 times higher compared to Fig. 3.6 and the structural homogeneity appears to be very similar as in the case of the 5 μm thin film. Furthermore, it is observed that in all cases (Figs. 3.5, 3.6 and 3.7) the SH signal amplitudes are enhanced on the right hand side of the sample giving rise to certain assumptions about the geometry of the growth reactor (section 4.2.1).

Fig. 3.8 shows the SH anisotropy of the ZnO film grown on Si(100) within 150 min (5 μm average thickness). In contrast to the clear 4-fold symmetry found in 3C-SiC (Fig. 3.3), an irregular random SH signal is observed for the ZnO thin layer. The SH signal amplitudes in Fig. 3.8 are consistent with those of the area scan in Fig. 3.6.

Stellenbosch University http://scholar.sun.ac.za

The films of 1 and 10 μm average thickness show similar SH anisotropy results.

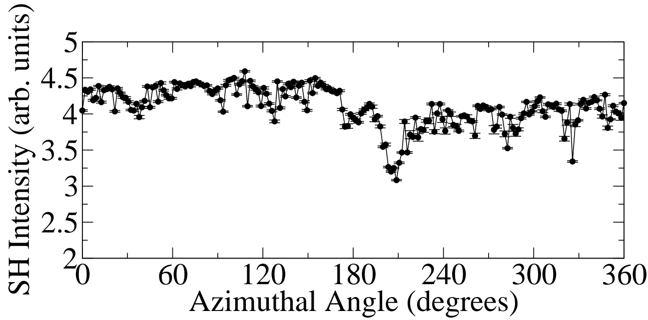

FIGURE 3.8: Rotational SH anisotropy of a ZnO film grown on Si(100) within 150 min (average thickness $\sim$ 5 μm). 12.5 GW/cm^2 laser peak intensity

3.2.2 ZnO on Glass

This section deals with the SHG experiments performed with ZnO films grown on amorphous glass (fused silica). In order to experimentally verify that the SH contribution of the glass substrate is neglegible similarly as in the above case of silicon substrates, a SH image was recorded of a clean substrate as shown in Fig. 3.9. The incident laser peak intensity was chosen to be 25 GW/cm^2 at a step resolution of 5 μm.

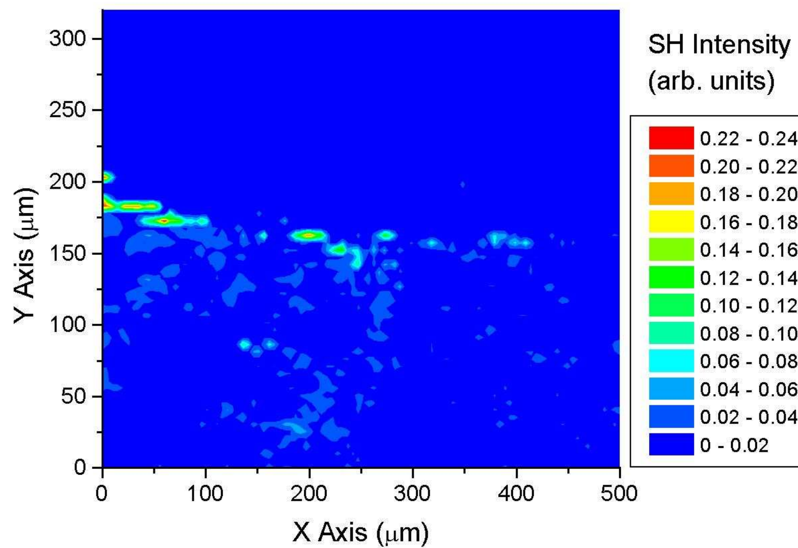

FIGURE 3.9: SH image of a clean amorphous glass substrate, 25 GW/cm^2 laser peak intensity, 5 μmu step resolution.

Stellenbosch University http://scholar.sun.ac.za

Except for small irregularities the SH response is below the here applicable experimental detection limit, which again makes background corrections due to SH signal arising from the glass substrate unnecessary.

Fig. 3.10 shows the measured SH intensity as a function of the incident laser peak intensity for two different ZnO films grown on amorphous glass. The growth times of the layers were 30 min and 150 min yielding average thicknesses of 1 and 5 μm.

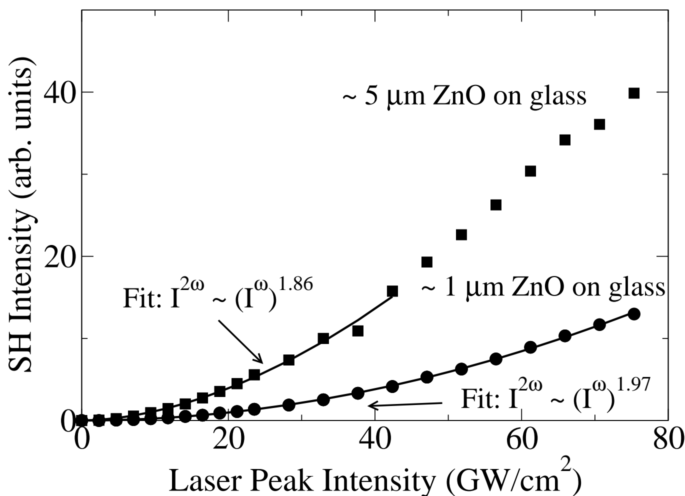

FIGURE 3.10: SH intensity as a function of the incident laser peak intensity for ZnO films of 1 and 5 μm average thickness grown on glass; solid lines: fitting curves: approx. quadratic relations below ~80 and ~50 GW/cm^2.

A clearly quadratic relation between the SH signal and the incident intensity holds up to at least 80 GW/cm^2 incident intensity in the case of the 1 μm film, whereas the SH conversion process begins to saturate at $\sim$ 50 GW/cm^2 in the 5 μm film.

The SH images of the two ZnO layers (1 and 5 μm) on glass shown in Figs. 3.11 (a) and 3.11 (b) were, hence, recorded at incident laser peak intensities of 25 and 12.5 GW/cm^2, respectively, at a step resolution of 30 μm. To ensure direct comparability between the two SH images, the arbitrary SH intensity units in Fig. 3.11 (a) were scaled by the factor 1/4 accounting for the fact the latter SH image was recorded at twice the incident laser peak intensity as compared to the area scan in Fig. 3.11 (b). Here the quadratic relation $I^{2\omega} \propto (I^{\omega})^2$ was assumed in agreement with Fig. 3.10.

Similar to the findings in ZnO on silicon substrates, the SH response of the ZnO layers deposited on glass is non-uniform and strongly position dependent. The thicker layer grown with 150 min (Fig. 3.11 (b)) in average shows an approximately 5 times larger SH signal compared to the 1 μm-layer grown within 30 min (Fig. 3.11 (a)). Overall, the morphology and homogeneity of the ZnO layers grown on glass appear to be very similar to the layers deposited on silicon. Also the fact that the SH response is enhanced on the right hand side of the samples is confirmed with glass substrates.

Stellenbosch University http://scholar.sun.ac.za

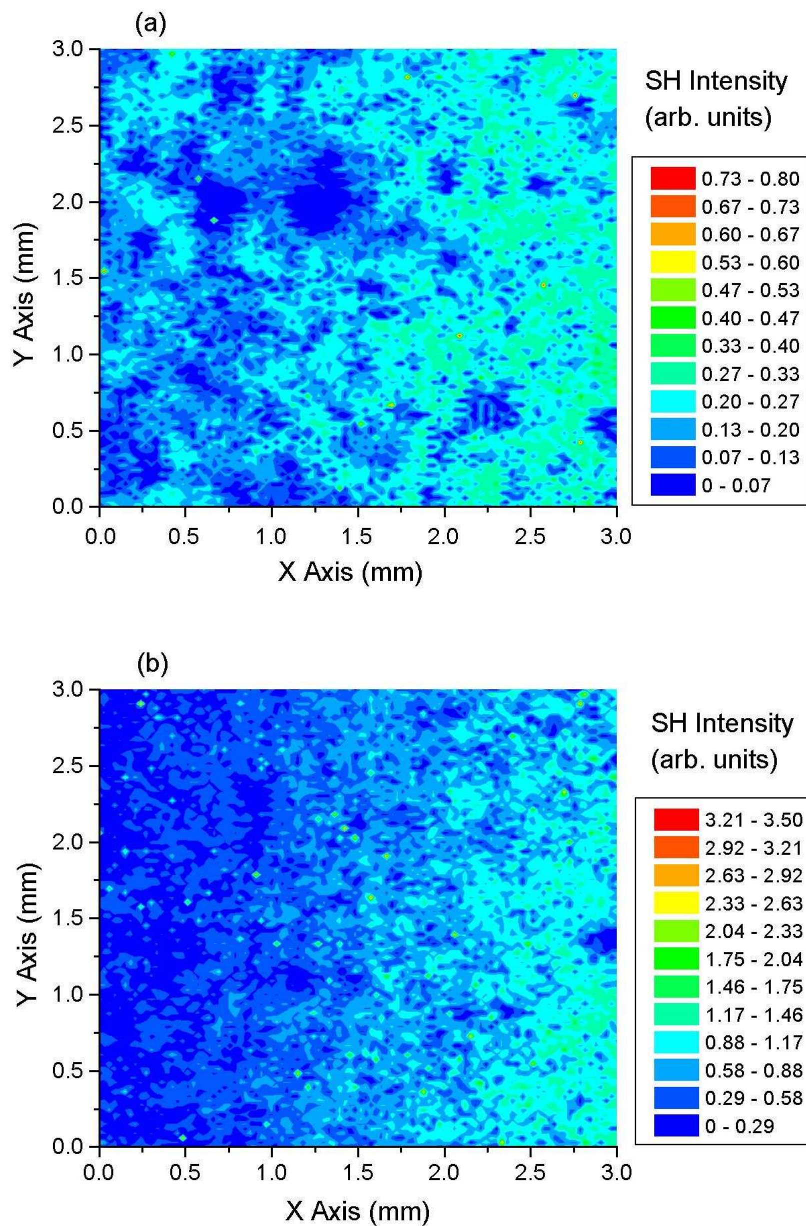

FIGURE 3.11: SH image of a ZnO films grown on amorphous glass; (a): growth time 30 min (average thickness $\sim 1\ \mu$m), 25 GW/cm^2 laser peak intensity, 30 μm step resolution, (b): growth time 150 min (average thickness $\sim 5\ \mu$m), 12.5 GW/cm^2 laser peak intensity, 30 μm step resolution.

Stellenbosch University http://scholar.sun.ac.za

3.2.3 ZnO on GaAs

In both the above cases using silicon and amorphous glass substrates the SH response arising from the substrate material could be neglected. GaAs representing the third substrate material employed here for the ZnO growth, is a non-centrosymmetric crystalline material of zinc-blende type crystal structure with non-vanishing $\chi^{(2)}$ elements (Eq. 1.28). Hence, superposing SH contributions of the same order of magnitude originating from the ZnO films as well as the underlying GaAs substrates are expected. In order to obtain information about the properties of the ZnO film, it is, therefore, necessary to isolate the film and substrate SH contributions by comparing SH images recorded before and after the deposition of ZnO on GaAs.

Fig. 3.12 shows the SH intensity generated in pure GaAs at the azimuthal maximum of the rotational SH anisotropy as a function of the incident laser peak intensity.

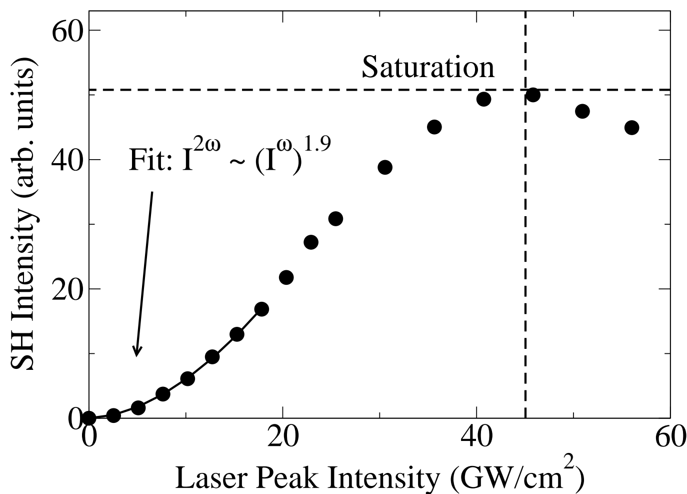

FIGURE 3.12: SH intensity generated in GaAs at azimuthal maximum as a function of the incident laser peak intensity; solid line: numerical fit: approximately quadratic relation below $\sim$ 20 GW/cm^2, SH signal saturation at $\sim$ 45 GW/cm^2.

Below $\sim$ 20 GW/cm^2 incident laser peak intensity a quadratic relation is observed indicating pure SHG (Eq.1.35), full saturation of SHG and, eventually, sample damage occur above $\sim$ 45 GW/cm^2.

Fig. 3.13 displays the rotational SH anisotropy pattern recorded of a GaAs wafer typically used here as substrate for the ZnO growth at an incident laser peak intensity of 12.5 GW/cm^2 and (p-p) polarization combination between excitation and detection. The solid line is a numerical fit according to Eq. 1.41. A clear 4-fold symmetry is observed. The differences in the SH signal amplitudes at the azimuthal maxima are characteristic for a surface off-cut angle of approximately 2° with respect to the (100) crystal orientation (see section 4.2.3).

Stellenbosch University http://scholar.sun.ac.za

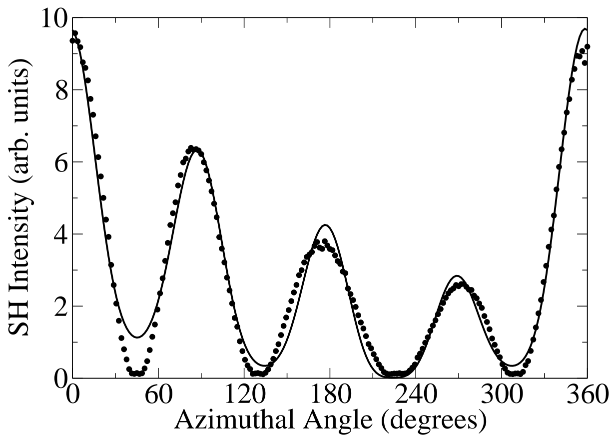

FIGURE 3.13: Rotational SH anisotropy pattern of GaAs substrate: (100) surface orientation, 2°-off-cut angle, 12.5 GW/cm^2 laser peak intensity, (p-p) polarization; solid line: fit according to Eq. 1.41.

Fig. 3.14 shows the corresponding SH image of a clean GaAs substrate recorded at the azimuthal maximum. Here the sample area is 0.5 mm by 0.5 mm, the spatial step resolution 5 μm, and the incident laser peak intensity 12.5 GW/cm^2.

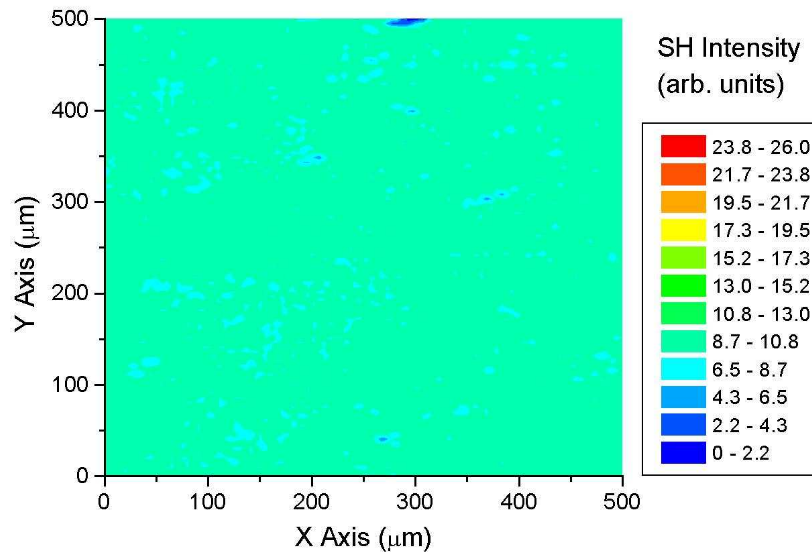

FIGURE 3.14: SH image of typical GaAs substrate wafer, 12.5 GW/cm^2 laser peak intensity, 5 μm step resolution.

Despite minor surface irregularities the SH response of the GaAs wafer in Fig. 3.14 is very uniform and homogeneous throughout the entire sample area.

In direct comparison to the clean GaAs substrate shown in Fig. 3.14, Fig. 3.15 displays an SH image of a comparable sample area (0.5 mm by 0.5 mm) after the deposition of the ZnO film (150 min, 5 μm average thickness). The SH image

Stellenbosch University http://scholar.sun.ac.za

was recorded with identical SHG parameters (12.5 GW/cm^2 peak intensity, (p-p) polarization, 5 μm step resolution, same azimuthal angle). Equal colour scales were chosen for both SH images.

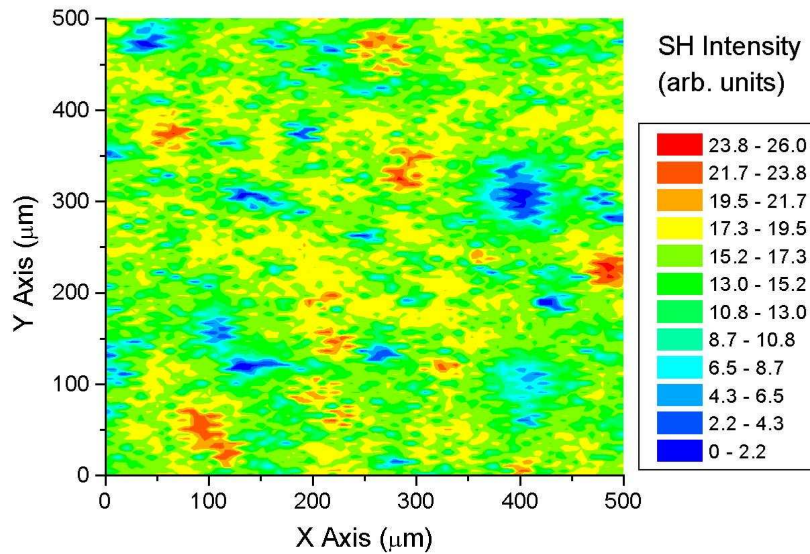

FIGURE 3.15: SH image of a ZnO film grown within 150 min in GaAs(100) (average thickness $\sim$ 5 μm), 12.5 GW/cm^2 laser peak intensity, 5 μm step resolution.

Clearly an irregular, position dependent SH response is observed after the ZnO deposition similarly as in the cases of silicon and glass substrates. In some sample areas, where ZnO was deposited, the observed SH signal amplitudes are larger (yellow and red spots) compared to those of the clean substrate, in some areas approximately equal (green and light green areas), and as clearly resolved in Fig. 3.15, a significant amount of areas (blue and dark blue regions, SH intensity < 6.5 arb. units) occurs, where even the SH signal originating from the underlying GaAs substrate is obviously suppressed. The typical size of these areas is 20-50 μm.

Stellenbosch University http://scholar.sun.ac.za

3.3 Lead Cadmium Telluride ($Pb_xCd_{1-x}Te$)

The $Pb_xCd_{1-x}Te$ wafers ($x = 0.20$) as prepared by collaborating researchers[3] are investigated in a comparatative study using the methods scanning electron microscopy (SEM) as well as SHG.

3.3.1 SEM in $Pb_xCd_{1-x}Te$

The morphology of typical $Pb_{0.20}Cd_{0.80}Te$ wafers cut perpendicular to the growth direction is first investigated using a standard scanning electron microscope (Philips XL30). The SEM image displayed in Fig. 3.16 clearly shows the separation of two phases, which was observed earlier in these wafers by our collaborators [75]. The lighter area on the left-hand side represents a phase of Pb-rich composition, whereas the darker right-hand side shows the Cd-rich phase. These two phases are found to segregate during the growth process of $Pb_xCd_{1-x}Te$ [75].

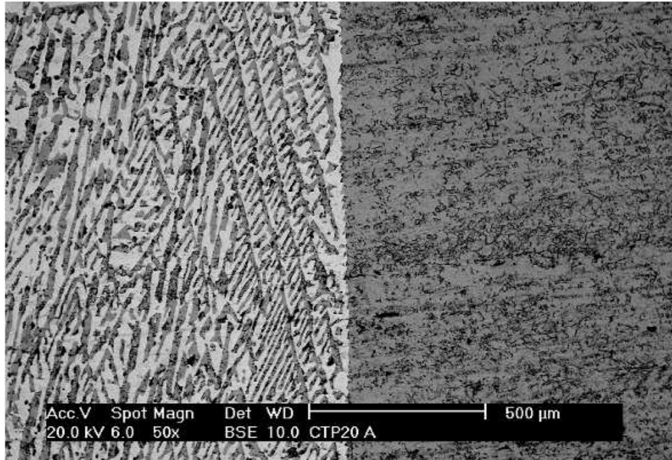

FIGURE 3.16: SEM image of a typical $Pb_{0.20}Cd_{0.80}Te$ wafer with clearly distinguishable Pb-rich (left) and Cd-rich phases (right).

If, particularly, the Pb-rich phase (left-hand side in Fig. 3.16) is investigated in further detail by high resolution SEM imaging as displayed in Fig. 3.17, clearly the presence of triangular enclosures is revealed, which are embedded in the Pb-rich phase. These enclosures represent crystalline micrograins of Cd-rich material which are strongly aligned in the (111) direction (Fig. 3.17) [83]. The formation of this type of microcrystals is related to the supercooling in the PbTe phase during the solidification process and is discussed in further detail in section 4.3.1.

[3] E. Saucedo *et al.*, Departamento de Física de Materiales, Universidad Autónoma de Madrid, Madrid 28049, Spain

Stellenbosch University http://scholar.sun.ac.za

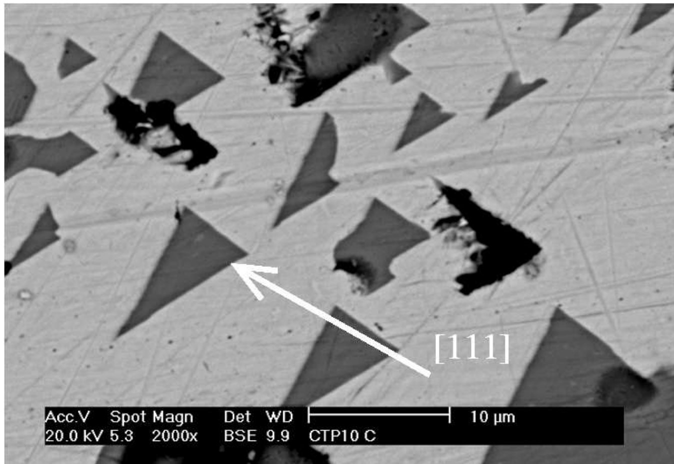

FIGURE 3.17: High resolution SEM image of Pb-rich phase in a typical $Pb_{0.20}Cd_{0.80}Te$ wafer: Cd-rich microcrystals enclosed into the Pb-rich phase.

In the case of slow cooling rates (2° C/h) the coalescence of the Cd-rich microcrystals leads to a formation of a superlatice structure characterized by an alternating layer-by-layer accommodation of the Pb-rich and Cd-rich phases. Fig. 3.18 shows this phenomenon in a SEM image.

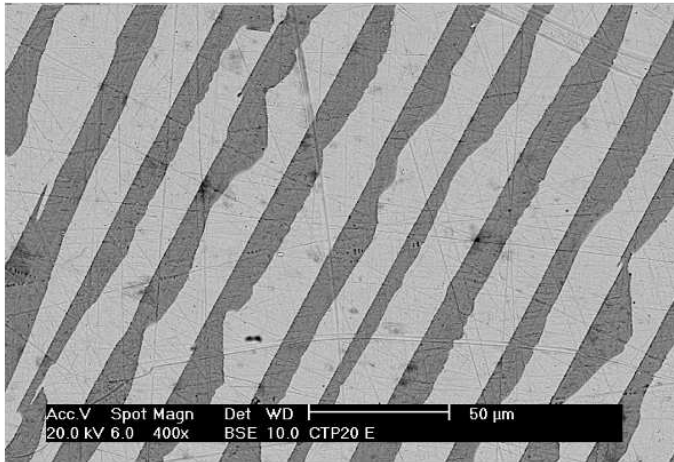

FIGURE 3.18: High resolution SEM image: Periodic layer-by-layer accommodation of Pb-rich and Cd-rich phases on a 10 μm length scale.

The periodicity of the superlatice of Pb-rich and Cd-rich material at the employed cooling rate (2° C/h) occurs on a 10 μm length scale.

The following sections deal with the SHG experiments performed with $Pb_xCd_{1-x}Te$ wafers yielding detailed results complementing the SEM analysis.

Stellenbosch University http://scholar.sun.ac.za

3.3.2 SHG in CdTe and PbTe

In order to quantitatively evaluate the SH response of the ternary alloy $Pb_{0.20}Cd_{0.80}Te$, compare the SH signal amplitudes to a reference, and eventually distinguish between SH contributions originating from the Pb-rich and Cd-rich phases, respectively, at first, SHG experiments are performed with the pure underlying binary compounds CdTe and PbTe.

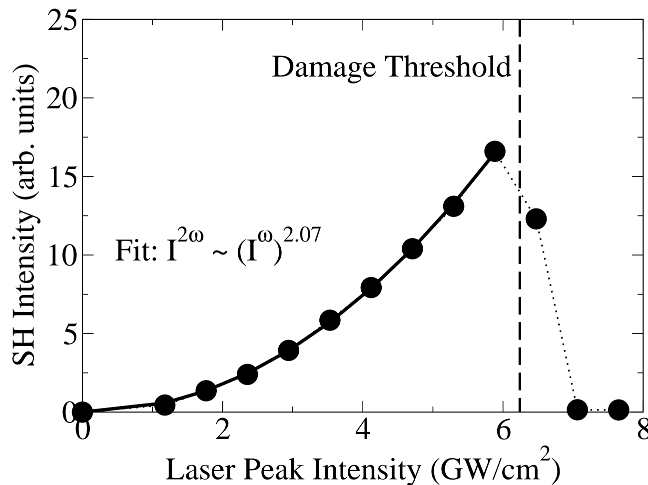

FIGURE 3.19: Quadratic dependence of the SH intensity $I^{(2\omega)}$ generated in CdTe on the incident fundamental laser intensity $I^{(\omega)}$ up to the approximate sample damage threshold of ~ 6 GW/cm^2.

Fig. 3.19 shows the SH intensity generated in CdTe as a function of the incident fundamental laser intensity. The approximately quadratic fit (solid line in Fig. 3.19) is evidence of pure SHG (Eq. 1.35). At an incident laser peak intensity of approximately 6 GW/cm^2 the sample damage threshold is reached and the SHG signal drops abruptly to zero due to an obvious destruction of the crystalline structure of the CdTe compound.

Fig. 3.20 displays a SH image of a 0.5 mm by 0.5 mm sample area of a typical CdTe wafer. The image was recorded at 3.5 GW/cm^2 incident laser peak intensity, 5 μm translational step resolution in the x- and y-directions, as well as (p-p) polarization combination. Apart from minor surface irregularities the SH response is very uniform throughout the entire sample area, characteristic for high quality single crystalline material (similar as in the cases of SiC and GaAs). The position dependent variations of the SH signal amplitude are in the order of 10%.

Stellenbosch University http://scholar.sun.ac.za

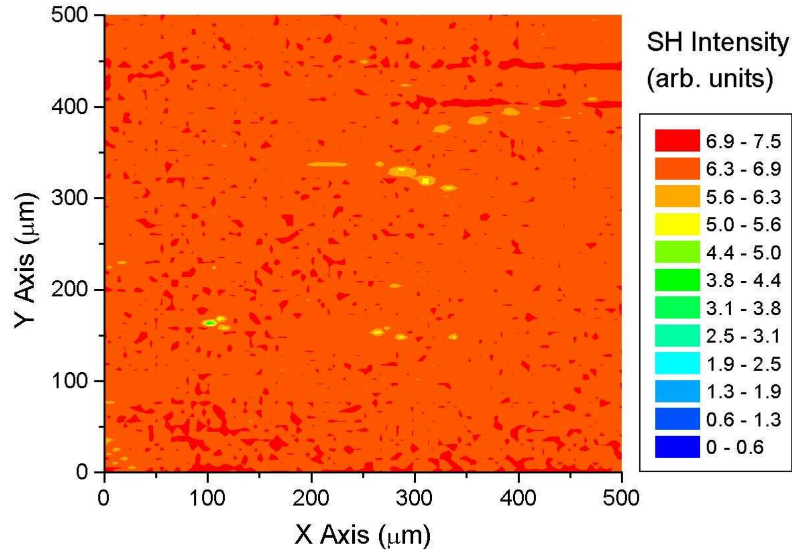

FIGURE 3.20: SH image of pure CdTe: 3.5 GW/cm^2 incident laser peak intensity, 5 μm step resolution, p-p polarization combination; uniform SH response of single crystalline material CdTe (111).

The rotational SH anisotropy of the same CdTe wafer is displayed in Fig. 3.21 for all polarization combinations yielding SH signal amplitudes consistent with the area scan in Fig. 3.20.

A clear and regular three-fold symmetry is observed for the (p-p) and (s-p) polarization combinations, and a full six-fold symmetry for (p-s) and (s-s). The solid lines are fitting curves according to Eq. 4.2 (section 4.3.2). As discussed in detail in section 4.3.2 the symmetry properties observed in Fig. 3.21 identify the CdTe wafer to be of very regular zinc-blende type structure of (111) surface orientation.

In contrast to the SHG results obtained for CdTe, the SH response of pure PbTe is found to be below the here applicable experimental detection limit. This implies that the SH signal amplitudes generated in PbTe are at least two orders of magnitude smaller than in the case of CdTe. As discussed in section 4.3.2, this is rationalized by the centrosymmetric crystalline structure of PbTe (rock salt, section 1.4.3).

Stellenbosch University http://scholar.sun.ac.za

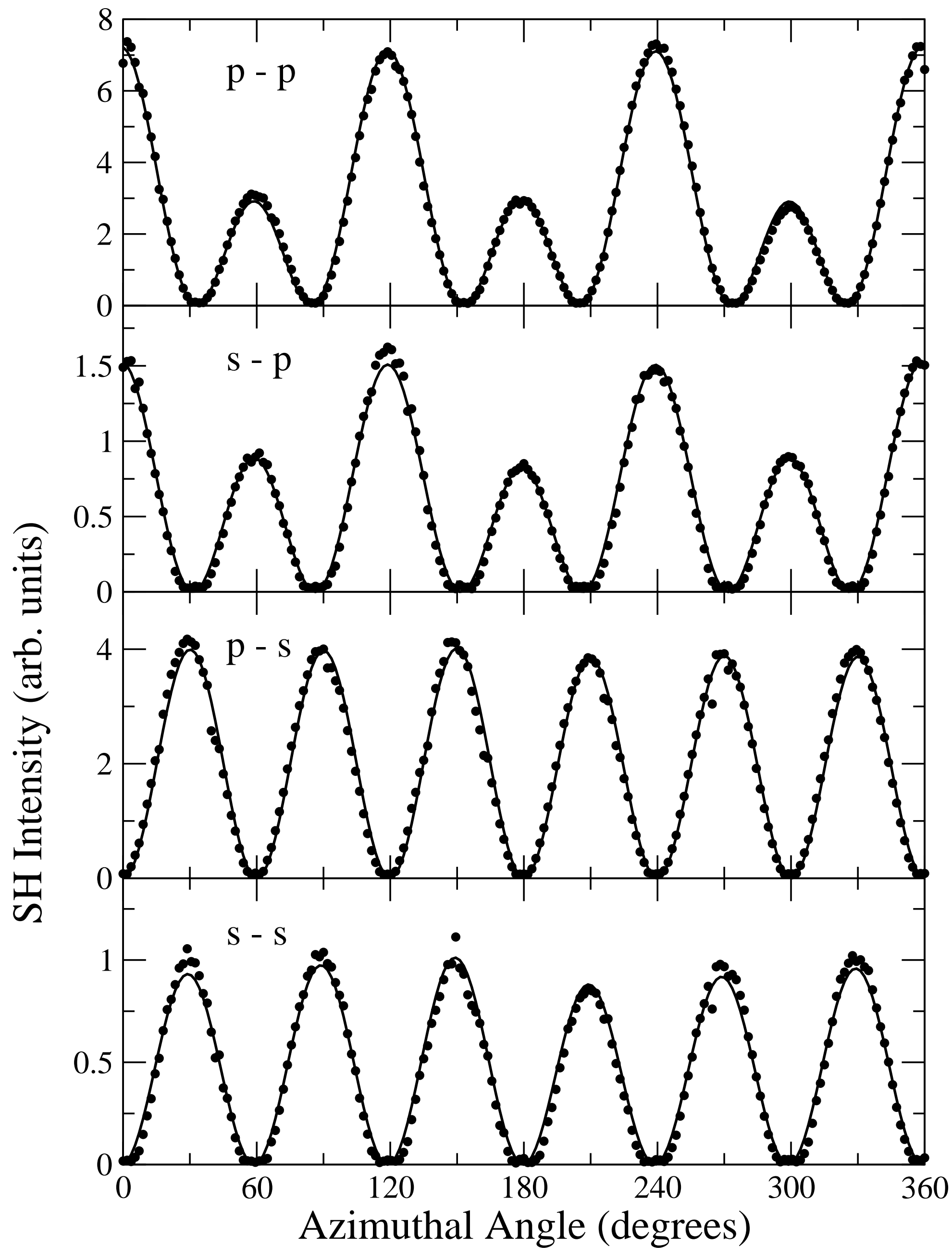

FIGURE 3.21: Rotational SH anisotropy of single crystalline CdTe (111): threefold symmetry for the p-p and s-p polarization combinations, sixfold symmetry for p-s and s-s; solid lines: fitting curves according to Eq. 4.2 (section 4.3.2, Refs. [21, 37]).

Stellenbosch University http://scholar.sun.ac.za

3.3.3 SHG in $Pb_xCd_{1-x}Te$

In this section the SH response of $Pb_{0.20}Cd_{0.80}Te$ ternary alloys is investigated.

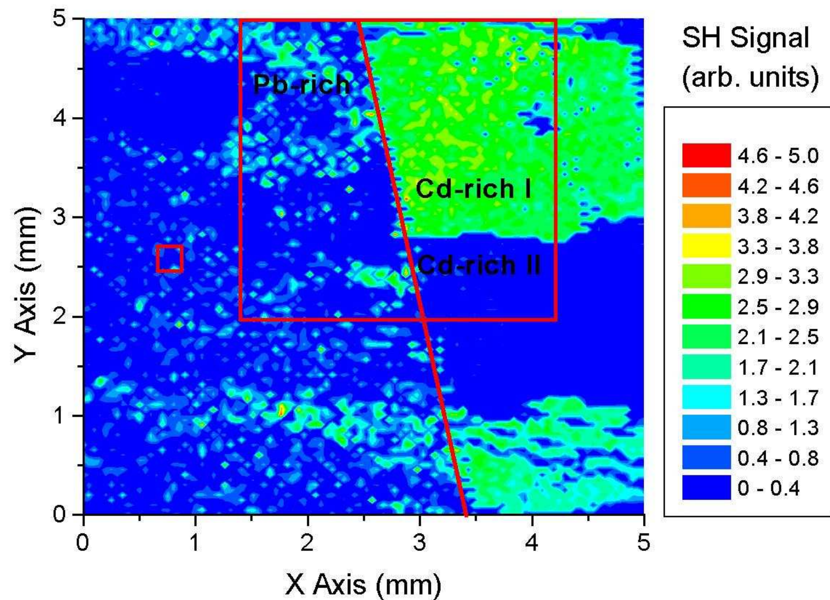

FIGURE 3.22: SH image of a typical $Pb_xCd_{1-x}Te$ wafer recorded at 3.5 GW/cm^2 incident laser peak intensity, (p-p) polarization combination, 50 μm step resolution; additional images of the areas highlighted by the small and large squares are shown in Figs. 3.23 and 3.24, respectively.

Fig. 3.22 shows a SH image of a 5 mm by 5 mm sample area of a typical $Pb_{0.20}Cd_{0.80}Te$ wafer recorded in the (p-p) polarization combination. The incident laser peak intensity was 3.5 GW/cm^2, and the spatial step resolution 50 μm. In Fig. 3.22 the boundary between the Pb-rich and Cd-rich phase (left- and right-hand side, respectively) is clearly identified in agreement with the SEM image in Fig. 3.16 and highlighted by the red line. In the following, the SH response of the the two different phases is investigated separately.

3.3.3.1 SHG in the Pb-rich Phase of $Pb_xCd_{1-x}Te$

The area on the left hand side of the red boundary line in Fig. 3.22 represents the Pb-rich phase and shows a rather position dependent SH response. A weak to vanishing background SH signal (blue) is superposed by a random distribution

Stellenbosch University http://scholar.sun.ac.za

of highly responsive grains (yellow, green). These are attributed to the Cd-rich microcrystallites embedded in the Pb-rich phase, consistently visualized by SEM (Fig. 3.17). The grain size of these microcrystallites is found to be in the order of the spatial step resolution of 50 μm.

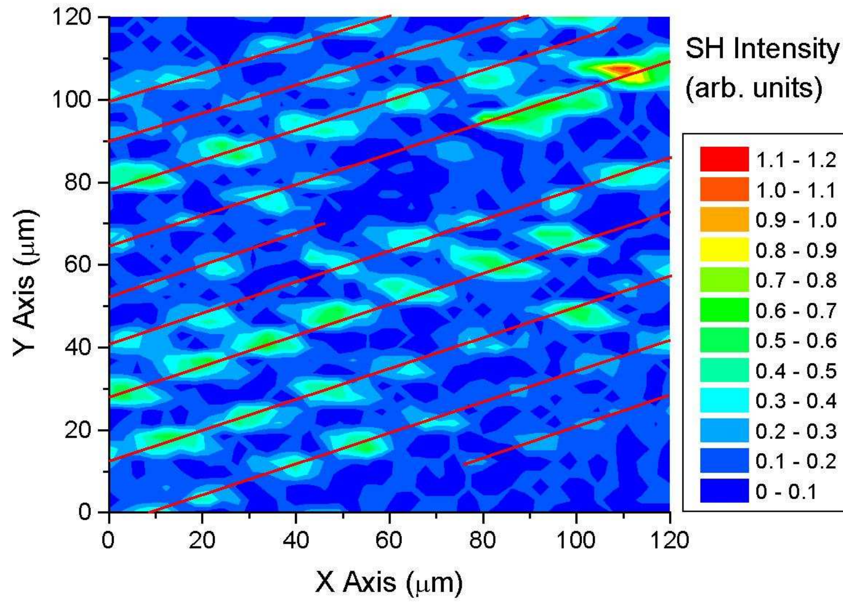

FIGURE 3.23: High resolution SH image of the area within the small red square in Fig. 3.22, 3.5 GW/cm^2, (p-p) polarization combination, 3 μm step resolution; periodically alternating SH response (highlighted by red lines) due to layer-by-layer accommodation of Cd-rich (high SH response) and Pb-rich (low to vanishing SH response) phases on a length scale of $\sim$ 10 μm.

Fig. 3.23 shows a high-resolution SH image of the area highlighted by the small red square in Fig. 3.22. The sample area of 120 μm by 120 μm was scanned at a translational step resolution of 3 μm, and 3.5 GW/cm^2 incident laser peak intensity, in the (p-p) polarization combination. On a length scale of approximately 10 μm a periodically alternating SH response is observed as highlighted by the red lines in Fig. 3.23. Clearly the alternating SH response reflects the superlattice structure induced by the layer-by-layer accommodation of Pb-rich and Cd-rich phases in the ternary alloy wafers, as it is consistently observed by SEM (Fig. 3.18). Hence the Pb-rich phase of the $Pb_xCd_{1-x}Te$ material investigated here is found to show a periodically alternating SH response on a 10 micrometer length scale.

Stellenbosch University http://scholar.sun.ac.za

3.3.3.2 SHG in the Cd-rich Phase of $Pb_xCd_{1-x}Te$

The area on the right hand side of the red boundary line in Fig. 3.22 represents the Cd-rich phase of the ternary alloy wafer. Here, large coherent areas of relatively uniform SH response occur. The maximum SH signal heights are found to be reduced by approximately 30% as compared to the SH signal amplitudes generated in pure CdTe using equal incident laser intensities (Fig. 3.20). It is immediately apparent from Fig. 3.22 that, within the Cd-rich phase, regions of high SH response (Cd-rich I) occur as well as regions of low to vanishing SH response (Cd-rich II). The SEM image in Fig. 3.16, however shows a uniform morphology of the Cd-rich phase, ruling out the presence of coherent Pb-rich areas of relevant size within the Cd-rich phase. Hence, it is found that the SH response is distinctly different in various regions of the Cd-rich phase. In the following, SH imaging at different azimuthal angles as well as polarization resolved SH imaging is employed to investigate this observation in further detail.

Fig. 3.24 (a) presents an enlarged SH image of the sample area highlighted by the large red square in Fig. 3.22 (3 mm by 3 mm, 30 μm step resolution, 3.5 GW/cm^2, (p-p) polarization). Fig. 3.24 (b) shows the identical sample area recorded under equal experimental conditions (both (p-p) polarization combination), but at an azimuthal angle rotated by 30.6° with respect to the area scan in Fig. 3.24 (a).

Comparing Figs. 3.24 (a) and 3.24 (b) it is found that after the sample rotation by $\sim 30°$ regions of previously strong SH reponse (Cd-rich I in Fig. 3.24 (a)) show a weak to vanishing SH response in Fig. 3.24 (b) and vice versa (Cd-rich II). The maximum SH signal heights reached in region Cd-rich I in Fig. 3.24 (a) are approximately equal to those obtained in region Cd-rich II in Fig. 3.24 (b). Hence, an azimuthal phase shift is observed between the Cd-rich regions I and II.

Stellenbosch University http://scholar.sun.ac.za

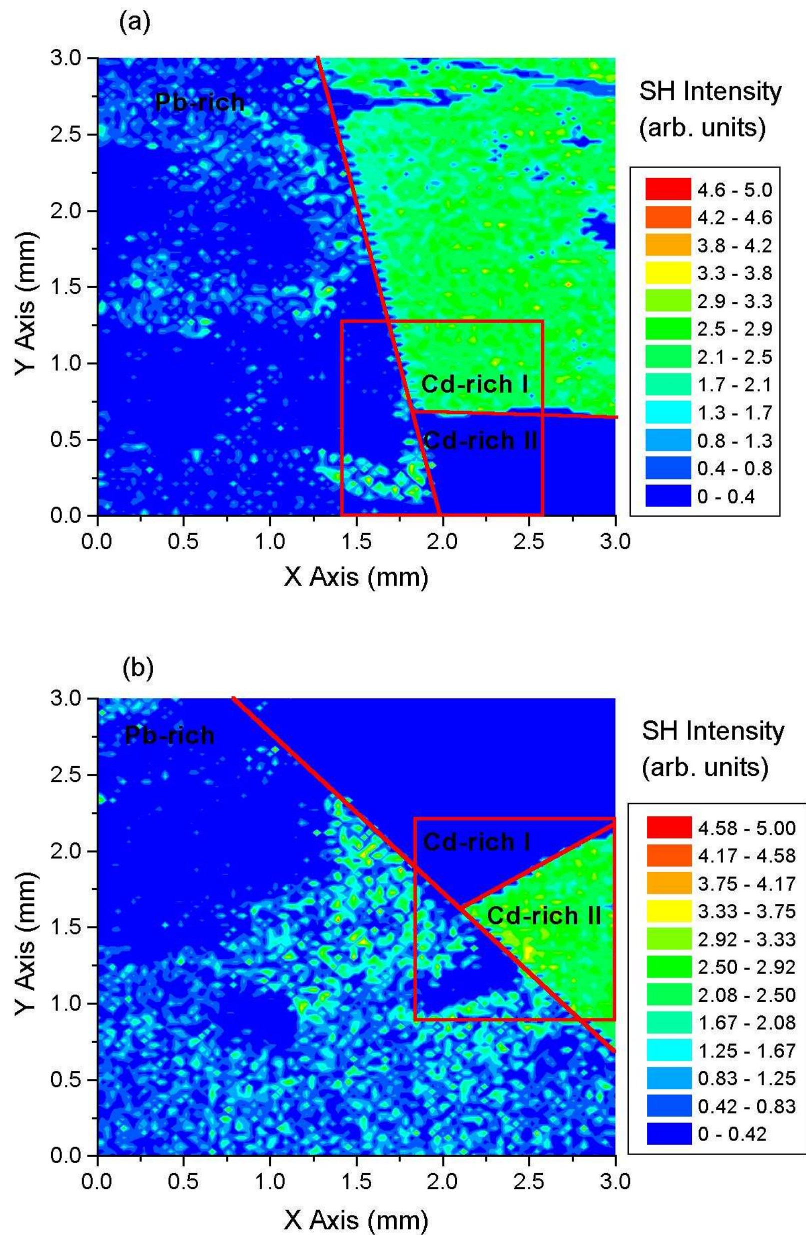

FIGURE 3.24: SH images of identical sample area (large red square in Fig. 3.22) recorded in (p-p) polarization combination but with rotation of the azimuthal angle by $\sim 30°$ in (b) with respect to (a). Cd-rich areas of strong SH response (Cd-rich I) in (a) show a weak to vanishing SH response after azimuthal rotation by $\sim 30°$ (b), and vice versa (Cd-rich II).

Stellenbosch University http://scholar.sun.ac.za

In a further experiment SH images were recorded of the sample area highlighted by the red square in Fig. 3.24 (b). Fig. 3.25 (a) shows an enlargement of this area (1.2 mm by 1.2 mm, 30 μm step resolution, 3.5 GW/cm^2) recorded in the (p-p) polarization combination. Fig. 3.25 (b) presents a SH image of the identical sample area recorded at the equal azimuthal angle, but in the (p-s) polarization combination. Again, Cd-rich areas of weak to vanishing SH response in Fig. 3.25 (a) (Cd-rich I) show a strong SH response in Fig. 3.25 (b), and vice versa (Cd-rich II). Considering the rotational SH anisotropy measurements in Fig. 3.21, and especially the curves recorded in the (p-p) and (p-s) polarization combinations, the switch in the observed SH intensity amplitudes in Figs. 3.25 (a) and 3.25 (b) under different detection polarizations is another strong indication for the phase shift between the Cd-rich regions I and II. As seen in Fig. 3.25 (b) the SH signal does not vanish completely in the Cd-rich region II indicating that the angle of the observed phase shift deviates slightly from the 30° value.

Thus, both SH imaging at different azimuthal angles as well as polarization resolved SH imaging consistently visualize two different Cd-rich large coherent regions (several mm^2) in $Pb_{0.20}Cd_{0.80}Te$ wafers enclosing an azimuthal SH phase shift close to 30°.

Stellenbosch University http://scholar.sun.ac.za

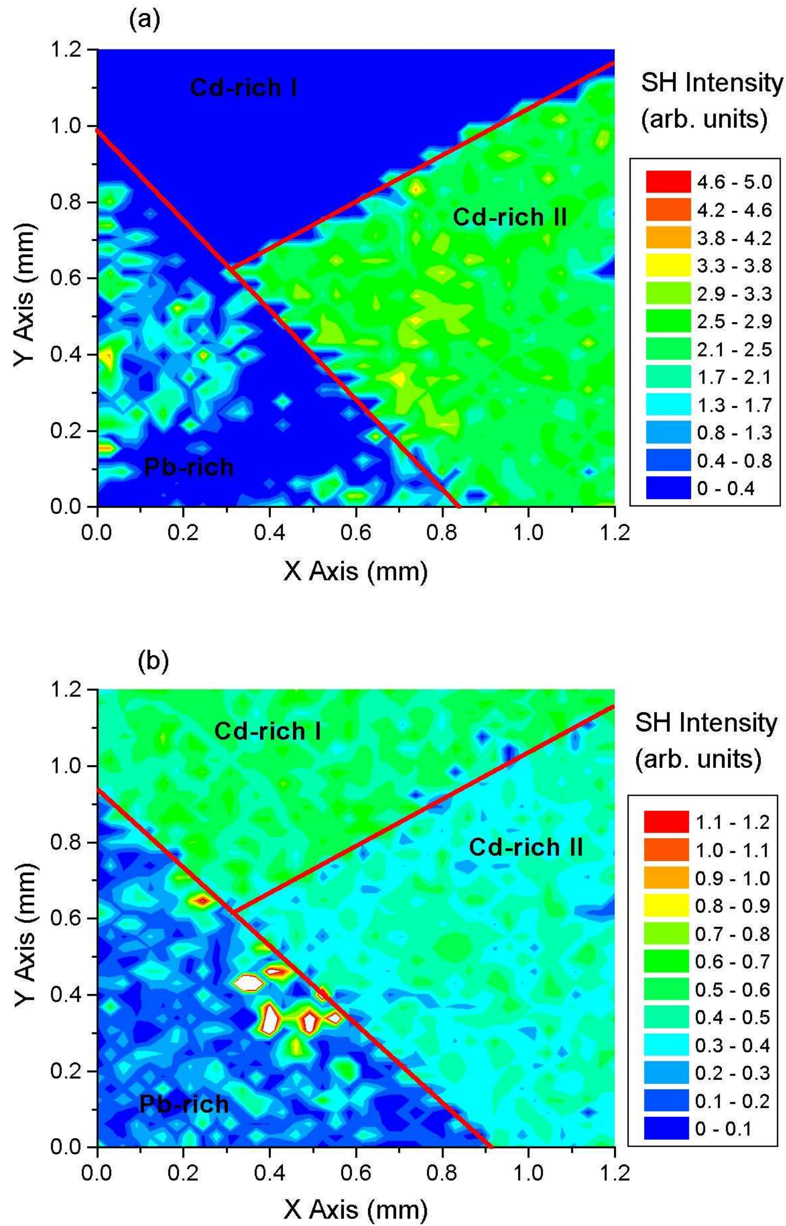

FIGURE 3.25: SH images recorded of identical sample area (red square in Fig. 3.24 (b)) at identical azimuthal angles, but with different polarization combinations, (a): (p-p), (b): (p-s). Sample areas of weak to vanishing SH response (Cd-rich I) in (a) show a strong SH response in (b), and vice versa (Cd-rich II).

Stellenbosch University http://scholar.sun.ac.za

Chapter 4

Discussion

In the following chapter the experimental findings are discussed and interpreted. Each of the three material systems (SiC, ZnO and $Pb_xCd_{1-x}Te$) is considered in a separate section. Detailed information is derived concerning crucial material properties, such as the structural quality, the crystal orientation, the homogeneity or the optical damage threshold for near infrared femtosecond irradition. Particularly in the case of ZnO, SHG also reveals valuable information about some aspects of the MOCVD sample growth processes.

4.1 Interpretation of the SiC-Results

The SHG experiments with SiC thin films (~ 5 μm, grown on Si(100)) presented in this work were mainly conducted for calibration purposes and reproduceability tests to ensure the full functionality of the experimental setup. The measurements performed here consistently reproduce results previously reported in the literature [23, 47, 48].

The dependence of the SH signal on the incident fundamental laser peak intensity shown in Fig. 3.1, on the one hand, indicates a well defined SH conversion process for intensities ≤ 4 GW/cm^2. This is confirmed by the numerical fit (solid line in Fig. 3.1). On the other hand, the SHG saturation intensity (NIR fs-pulses, 80 MHz) is determined to be ~ 8 GW/cm^2 for the ~ 5 μm thin SiC film grown on silicon.

The SH image displayed in Fig. 3.2 shows a very uniform SH response throughout the entire sample area. This is characteristic for homogeneous film deposition. Fig. 3.2 clearly indicates high quality, single-crystalline film growth throughout the sample area. In the left bottom corner of the SH image the SH signal appears to be

Stellenbosch University http://scholar.sun.ac.za

decreased by approximately 20 % compared to the other parts of the sample. Since the bulk SH contributions dominate the SH response of SiC (sections 1.4.3, 1.5.3), this observation is seen as an indication that in the left bottom corner the thickness of the SiC film is reduced compared to the rest of the sample. Hence, SH imaging proves to be suitable to monitor the CVD process with respect to the uniformity of the film thickness.

Fig. 3.3 shows the rotational anisotropy pattern of the SiC film recorded in all four polarization combinations (p-p), (s-p), (p-s) and (s-s) between excitation and detection. In the case of zinc-blende type crystal structures, where the form of the d_{il}-tensor as given in Eq. 1.28 is applicable, the expressions for the azimuthal angular dependences of the p- and s-polarized SH intensities given in Eqs. 1.41 and 1.42 reduce to the following angular functions for the (100) crystal orientation [23, 37, 48]:

$$\begin{array}{cccc} (p-p) & (s-p) & (p-s) & (s-s) \\ I^{2\omega} \propto |\cos(2\psi+\phi)|^2 & I^{2\omega} \propto |\cos(2\psi+\phi)|^2 & I^{2\omega} \propto |\sin(2\psi+\phi)|^2 & 0 \end{array} \tag{4.1}$$

Here ϕ is an arbitrary phase representing the azimuthal angle at the start of the SH anisotropy measurement. In the (s-s) polarization combination the SH signal is expected to vanish in the dipole approximation. The grey solid lines in Fig. 3.3 are fitting curves according to Eq. 4.1 for the respective polarization combinations. They show very good agreement with the measurements, reflecting the four-fold symmetry as well as the azimuthal phase shift of 90° between the p- and s-polarized SH anisotropy patterns. Furthermore, the (s-s) polarized recording, indeed, shows a vanishing SH signal.

The SH anisotropy measurements in Fig. 3.3 and their excellent reproduction by the fits according to Eq. 4.1 unambiguously identify the here investigated SiC thin film to be the 3C-polytype (cubic stacking order), grown in the (100) crystal direction.

Thus, using SHG, important information about the quality of thin SiC films deposited by CVD on silicon is obtained. The investigated material is identified to be single-crystalline 3C-SiC of homogeneous structural film quality throughout the entire sample area. The results presented here [84] are consistent with results reported in the recent relevant literature [23, 48, 49] and summarized in Table 4.1.

Hence, it is evidently verified that the experimental setup developed as part of this work is fully operational, satifactorily calibrated and suitable to obtain reproducable results, which are comparable to those published in the recent literature [23, 47–49].

Stellenbosch University http://scholar.sun.ac.za

TABLE 4.1: Summary: SHG analysis of SiC thin film ($\sim 5\ \mu$m) deposited on Si(100) by CVD.

SiC	
well-defined SHG	≤ 4 GW/cm^2
full SHG saturation	~ 8 GW/cm^2
structure	• zinc-blende
	• homogeneous single crystalline layer
	• (100) surface orientation
	• 3C-SiC polytype (cubic stacking)

The following sections deal with the interpretation of the SHG experiments performed with ZnO thin films as well as bulk $Pb_xCd_{1-x}Te$ wafers representing the main subjects of this dissertation with novel character.

4.2 Interpretation of the ZnO-Results

ZnO has non-centrosymmetric wurtzite crystal structure and is known to show a large SH response in the form of bulk material as well as thin films [85–87]. SHG experiments were performed here to characterize ZnO thin films grown by MOCVD on the three different substrate materials, silicon of (100) surface orientation, amorphous glass, as well as gallium arsenide of (100) surface orientation. They are discussed and interpreted separately in the following sections.

4.2.1 ZnO on Si(100)

In silicon the dipole allowed SH contribution vanishes due to the centrosymmetric diamond-like crystal structure [36]. SH signals generated in silicon arise from surface as well as bulk electric quadrupole and magnetic dipole terms [35, 36]. The resulting SH signal amplitudes are well known [21, 81, 82] and at least two orders of magnitude smaller than the SH signal amplitudes generated in ZnO, which, due to its non-centrosymmetric crystalline structure, show a second order optical susceptibility up to at least $\chi^{(2)} = 10$ pm/V [85]. Therefore, the SH signal arising from the substrate material is neglegable being by far dominated by the ZnO contribution. Interferences between substrate and film SH contributions are, hence, not expected and background corrections are unnecessary.

Stellenbosch University http://scholar.sun.ac.za

Fig. 3.4 shows the dependence of the SH intensity on the incident fundamental laser peak intensity for three different ZnO films of 1, 5 and 10 μm average thickness deposited within growth times of 30, 150 and 300 min on Si(100). The broken inversion symmetry of the wurtzite crystal structure of ZnO (section 1.4.3) implies that SHG arising from the bulk material is dominant over pure surface contributions. This is clearly reflected and confirmed by the observation in Fig. 3.4 that the SH intensity increases with the film thickness for a given incident laser peak intensity. Furthermore, it is found that the incident intensity, at which SH saturation occurs decreases with increasing film thickness. Full SH saturation is observed for incident laser peak intensities above ~ 90, ~ 65 and ~ 35 GW/cm^2 for 1, 5 and 10 μm thin films, respectively. The SH signal height reached under saturation is approximately equal for the 5, and 10 μm thin films and amounts ~ 60 arb. units. Fig. 3.4, hence, suits to identify the intensity regimes, where well defined unsaturated SH conversion takes place in the different ZnO films. Below ~ 45, ~ 30 and ~ 20 GW/cm^2 pure SHG is expected as confirmed by the approximately quadratic fits (solid lines in Fig. 3.4), respectively.

Comparing the SH images of the ZnO films grown within 30, 150 and 300 min in Figs. 3.5, 3.6 and 3.7 it is found that irrespective of the growth time, and hence the film thickness, all samples show SH responses, which strongly depend on the sample position. This leads to the conclusion that all films are deposited in a polycrystalline structure. The grain size of the microcrystals forming the ZnO film is found to be of the same order of magnitude as the spatial step resolution of the SH images and amounts to 20-50 μm.
The rotational SH anisotropy of the ZnO film in Fig. 3.8 lacks a clear symmetry (in contrast to the single crystalline SiC film discussed in section 4.1). Clearly, a random dependence of the (p-p) polarized SH intensity on the azimuthal angle is observed. This finding strongly supports the assumption of a polycrystalline film structure containing randomly orientated microcrystals.
Furthermore, consistent with Fig. 3.4, the SH images (Figs. 3.5, 3.6 and 3.7) show average SH signals, which increase with the film thickness, confirming that SHG is dominated by the bulk SH contributions arising from the film material.

The SH image in Fig. 3.5 displaying an area scan of the ZnO film deposited within 30 min represents the early stages of the MOCVD growth process. It is noted that highly responsive ZnO micrograins appear to be randomly deposited across the entire substrate area. It can be assumed that these crystalline micrograins act as seeds for the further film growth process. In the SH image recorded of a ZnO film deposited within a five times larger growth time of 150 min (Fig. 3.6) isolated microcrystals

Stellenbosch University http://scholar.sun.ac.za

are hardly visible and the entire substrate area is covered with a polycrystalline film structure. This trend is continued in the SH image of the thickest film deposited within 300 min (Fig. 3.7). Again the film structure is spread throughout the entire substrate and the structural quality and morphological homogeneity appear to be very similar as in the film in Fig. 3.7.

Another common feature in Figs. 3.5, 3.6 and 3.7 is the finding that the SH signal amplitudes appear to be enhanced on the right hand side of the sample area. This is seen as an unambiguous indication that the MOCVD growth process, as employed here, is more efficient on the right hand side of the substrate surface. This can be related to the geometry of the growth reactor tube, taking into account the direction of the precursor-gas flow as well as the substrate position. SH imaging, hence, shows the potential to provide guiding criteria for the optimization of the geometrical configuration of the growth reactor yielding maximally uniform film deposition.

Striving towards the goal of ideal single crystalline film growth, MOCVD of ZnO thin films was tested with other substrate materials as discussed in the following sections.

4.2.2 ZnO on Glass

Due to their amorphous structure the SH response of the glass substrates employed here is expected to be considerably lower than that of the deposited polycrystalline ZnO film. This is experimentally verified by the SH image presented in Fig. 3.9. Within the experimental resolution the glass substrate shows a vanishing SH signal. The few isolated spots of non-vanishing SH response are attributed to surface impurities. Interferences between SH signals originating from glass substrate and ZnO film are neglegable and background correction is unnecessary.

Fig. 3.10 shows the dependences of the SH signal on the incident fundamental laser peak intensity for two ZnO films grown within 30 and 150 min. Indicated by the approximately quadratic fits, well defined SHG occurs in the 1 μm film within the entire here investigated intensity regime up to 80 GW/cm^2, and up to $\sim$ 50 GW/cm^2 in the 5 μm thin film. Again, the thicker film shows the stronger SH response at a given incident laser intensity, confirming the dominance of the bulk SH contribution arising from the ZnO film.

Qualitatively the SH images in Figs. 3.11 (a) and (b) recorded of the 1 μm and 5 μm thin ZnO films are very similar to the SH images of ZnO films on silicon substrates.

Stellenbosch University http://scholar.sun.ac.za

Again, the strongly position dependent SH response points to a polycrystalline film structure. The grain size is again in the order of 20-50 μm and the average SH response is approximately 5 times higher in the thicker film confirming the finding in Fig. 3.10. Also the higher efficiency of the growth process on the right hand side of the sample, which is related to the configuration of the growth reactor tube, is consistently reflected in Figs. 3.11 (a) and (b).

It is noted that the SH signal amplitudes observed in the ZnO films grown on glass are considerably smaller than those detected in ZnO films of comparable thickness deposited on silicon. This is particularly obvious, when comparing the SH images in Fig. 3.6 and Fig. 3.11 (b), which are recorded at equal incident laser peak intensity, yielding 4-5 times lower average SH signal amplitudes in the case of the glass substrate. This is consistent with Figs. 3.4 and 3.10, when looking at the SH signal dependences on the indident laser intensity for the films of 5 μm thickness grown on silicon and glass, respectively. The main reason for this finding is seen in the fact that glass has a considerably lower refractive index as compared to silicon at both, the fundamental (n_{glass}(782.8nm) $\sim$ 1.5, n_{Si}(782.8nm) = 3.7) as well as the SH frequencies (n_{glass}(391.4nm) $\sim$ 1.6, n_{Si}(391.4nm) = 6.7)[89–91]. Therefore, the reflectance at the film/substrate boundary is significantly higher for silicon yielding the larger SH signal measured in reflection from the ZnO films grown on silicon as compared to those deposited on glass substrates, even though the films show comparable thicknesses. This effect of stronger ZnO SH response for silicon compared to glass substrates is not as prominent in the case of the $\sim$ 1 μm films deposited within 30 min growth time, where the average SH signals differ only slightly for glass and silicon substrates. This is not surprising, since here no complete substrate coverage by a coherent ZnO films is achieved. The randomly distributed ZnO grains consistently show a stronger SH response in the case of silicon substrates (Figs. 3.5 and 3.11 (a)).

Overall the structure and homogeneity of the ZnO layers deposited on amorphous glass are comparable to the layers grown on silicon. Neither significant improvements nor aggravations with respect it the film quality are observed.

4.2.3 ZnO on GaAs

The zinc-blende type crystalline structure of GaAs is non-centrosymmetric. In contrast to the substrate materials silicon and glass discussed above, the SH response of GaAs is expected to be of the same order of magnitude as that of the deposited ZnO films [37, 92–94]. In order to isolate the SH contributions arising from the ZnO

Stellenbosch University http://scholar.sun.ac.za

film and the GaAs substrate, the latter is first investigated in pure form before the film deposition process is performed.

Fig. 3.12 displaying the dependence of the SH signal generated in pure GaAs as a function of the incident laser peak intensity indicates well defined SHG below $\sim$ 20 GW/cm^2 (solid line: approx. quadratic fit) and full SH saturation above $\sim$ 45 GW/cm^2. Laser induced irreversible damage of the GaAs substrate is found to occur for incident laser intensities above $\sim$ 60 GW/cm^2 (NIR fs-pulses, 80 MHz).

The SH image of a typical clean GaAs substrate in Fig. 3.14 shows a very uniform and homogeneous SH response. This is viewed as an indication for high quality single crystalline material. The rotational SH anisotropy pattern recorded of the GaAs substrate in the (p-p) polarization combination (Fig. 3.13) shows a clear four-fold symmetry, being clear evidence for the (100) surface orientation. The differences in the SH signal heights at the azimuthal maxima are explained by the 2° surface off-cut angle with respect to the (100) crystal direction. The solid line in Fig. 3.13 represents a fit according to Eq. 1.41 applicable for zinc-blende type crystal strcutures of (100) surface orientation [21, 37]. The fit shows good agreement with the experiment and confirms the interpretations of uniform single crystalline material of (100) surface orientation and 2° off-cut angle.

Fig. 3.15 presents a SH image of a ZnO film grown within 150 min (5 μm average thickness) on the above discussed GaAs substrate material. Again, very similar to the results seen with silicon and glass substrates, the ZnO film structure appears to be polycrystalline with typical grain sizes of 20-50 μm. The SH image (Fig. 3.15) representing the superposition of substrate- and ZnO-SH contributions allows further conclusions concerning the structure of the deposited film.
Clearly, in Fig. 3.15 randomly distributed areas and grains are identified characterized by SH signals, which either exceed, match or fall below the SH signal arising from the underlying GaAs substrate. This behaviour is, on the one hand, related to the polycrystalline nature of the ZnO film consisting of randomly orientated microcrystals. On the other hand, however, in the regions, where the SH signal arising from the substrate is suppressed (dark blue, SH intensity < 6.5 arb. units), it seems likely that the ZnO material is deposited in a presumably amorphous phase, which did not undergo a complete gas phase reaction of the film precursors during the MOCVD growth process. These areas are not only characterized by a vanishing SH response, they obviously absorb either significant amounts of the incident fundamental laser intensity or of the SH signal generated in the underlying GaAs substrate, leading to the suppression of the SH signal. It is mentioned that the possibility of partially amorphous deposition also on silicon and glass can not be excluded.

Stellenbosch University http://scholar.sun.ac.za

Thus, the SHG analysis of ZnO thin films deposited on GaAs substrates reveals that the parameters of the MOCVD growth process (such as the substrate temperature, the gas flow rates or the ratio of the precursor gases) need further optimization in order to achieve more satisfying results concerning the gas and surface reactions taking place during CVD, and eventually the structural film quality.

Table 4.2 summarizes the information obtained by SHG about ZnO thin films of various thicknesses grown on different substrates.

TABLE 4.2: Summary: SHG analysis of ZnO thin films of various thicknesses (growth times) deposited on Si(100), amorphous glass and GaAs(100) ($2°$ offcut angle) by MOCVD.

ZnO on Si(100)	~ 1 μm (30 min)	~ 5 μm (150 min)	~ 10 μm (300 min)
well-defined SHG	≤ 45 GW/cm^2	≤ 30 GW/cm^2	≤ 20 GW/cm^2
full SHG saturation	> 90 GW/cm^2	> 65 GW/cm^2	> 35 GW/cm^2
structure	polycrystalline	polycrystalline	polycrystalline
grain size	20-50 μm	20-50 μm	20-50 μm
ZnO on glass	~ 1 μm (30 min)	~ 5 μm (150 min)	-
well-defined SHG	≤ 80 GW/cm^2	≤ 50 GW/cm^2	-
full SHG saturation	> 90 GW/cm^2	> 80 GW/cm^2	-
structure	polycrystalline	polycrystalline	-
grain size	20-50 μm	20-50 μm	-
ZnO on GaAs(100)	-	~ 5 μm (150 min)	-
well-defined SHG	-	≤ 15 GW/cm^2	-
full SHG saturation	-	> 35 GW/cm^2	-
structure	-	polycrystalline, part. amorphous	-
grain size	-	20-50 μm	-

Overall, using SHG as a powerful optical probe, it is found that all here-investigated ZnO films deposited under identical growth conditions show very similar polycrystalline structures (20-50 μm grain size) irrespective of the employed substrate material (Si, glass, GaAs) [84, 88].

Stellenbosch University http://scholar.sun.ac.za

4.3 Interpretation of the $Pb_xCd_{1-x}Te$-Results

In the following sections the SHG results obtained with $Pb_xCd_{1-x}Te$ ternary alloys are discussed in comparison to the respective SEM analysis. Detailed information is deduced regarding the structural and morphological properties of this novel material system.

4.3.1 SEM in $Pb_xCd_{1-x}Te$

The SEM image in Fig. 3.16 clearly resolves two segregated phases within the $Pb_{0.20}Cd_{0.80}Te$ wafer, which have been previously observed and documented by our collaborators, who supplied the sample material [75]. This segregation into Pb-rich and Cd-rich phases (left and right hand side in Fig. 3.16, respectively) takes place during the solidification process of the melt, and is mainly due to the different crystalline structures of the binary compounds CdTe and PbTe (zinc blende and rock salt, respectively). Despite a very low lattice mismatch (lattice constants 6.481 Å and 6.459 Å for CdTe and PbTe, respectively) the formation of at least two phases is foreseen, when Cd atoms (hexahedral coordination) are substituted by Pb atoms (tetrahedral coordination). This leads to an instability in the (111)A plane and the PbTe segregation into precipitates [75].
This instability is also confirmed by the formation of Cd-rich triangular microcrystallites, which appear to be embedded in the PbTe precipitates and are aligned in the (111) direction as shown in Fig. 3.17 [75, 95]. Saucedo *et al.* identify radial supercooling effects as determining segregation problems. PbTe acts as solvent for CdTe yielding the crystallization of the observed faceted CdTe-rich microcrystals. At slow cooling rates (2 °C/h) and nominal Pb concentrations of $x = 0.20$ a coalescence of the CdTe-rich microcrystals is found leading to a regular layer-by-layer arrangement of alternating Pb-rich and Cd-rich phases as shown in Fig. 3.18. These layers, forming a superlattice structure, are aligned along the most stable CdTe plane (111) and show Pb-contents of 96-97 % and 1-4 %, respectively. The thicknesses of these layers are equivalent to the bases of the triangular Cd-rich microcrystals ($\sim 10\ \mu$m) seen in Fig. 3.17 [75].

4.3.2 SHG in CdTe and PbTe

The SHG analysis of the pure binary compounds CdTe and PbTe is performed to establish a reference and be able to comparatively evaluate the results obtained with

Stellenbosch University http://scholar.sun.ac.za

the $Pb_xCd_{1-x}Te$ ternary alloy.

CdTe has a non-centrosymmetric zinc blende type crystal structure showing a significant SH conversion efficiency [96, 97]. CdTe was recently used as nonlinear medium to generate autocorrelation traces of sub-picosecond laser pulses in the far infrared spectral range [98]. The dependence of the SH signal generated in CdTe on the incident laser peak intensity shown in Fig. 3.19 indicates well-defined SH conversion (approx. quadratic fit) up to the observed damage threshold of ~ 6 GW/cm^2. For even higher incident laser intensities the CdTe sample is irreversibly damaged by the near infrared femtosecond pulse train (80 MHz repetition rate) and the SH response drops to zero.

The regular and uniform SH response displayed in the SH image in Fig. 3.20 points to homogeneous single crystalline material. The minor irregularities are attributed to the surface roughness of the wafer resulting from the mechanical polishing procedure.

The rotational SH anisotropy of the CdTe sample wafer is shown in Fig. 3.21 for all four polarization combinations. The angular dependences of the p- and s-polarized SH intensities as given in Eqs. 1.41 and 1.42 reduce for zinc blende type crystals and (111) surface orientations to the following angular functions [37]:

$$
\begin{array}{cc}
(p-p) & (s-p) \\
I^{2\omega} \propto |a_1 + a_2 \cos(3\psi + \phi)|^2 & I^{2\omega} \propto |a_1 + a_2 \cos(3\psi + \phi)|^2 \\
(p-s) & (s-s) \\
I^{2\omega} \propto |a_1 + a_2 \sin(3\psi + \phi)|^2 & I^{2\omega} \propto |a_1 + a_2 \sin(3\psi + \phi)|^2
\end{array}
\qquad (4.2)
$$

The solid lines in Fig. 3.21 represent numerical data fits according to Eq. 4.2 with a_1 and a_2 as fit parameters, and ϕ the arbitrary phase at the start of the rotational SH anisotropy measurement. Excellent agreement between theory and experiment is found. Thus, the here-investigated CdTe wafers are identified to be of high single crystalline quality and (111) surface orientation. Consistent results on CdTe were reported by Berlouis *et al.* [99].

PbTe has a rock salt type crystalline structure, which is centrosymmetric. The dipole SH contribution is, therefore, parity forbidden [35]. Indeed the SH signal is found to be below the here-applicable experimental detection limit. This discrepancy in the SH response of the pure binary compounds CdTe and PbTe is regarded as a strong indication that the SH response of the $Pb_xCd_{1-x}Te$ ternary alloy is dominated by the Cd-rich phases.

Stellenbosch University http://scholar.sun.ac.za

Table 4.3 summarizes relevant properties of the pure binary compounds CdTe and PbTe.

TABLE 4.3: Summary: SHG analysis of CdTe and PbTe binary compounds grown be the vertical Bridgman method.

CdTe	
well-defined SHG	$\leq$ 6 GW/cm^2
sample damage	$\sim$ 6 GW/cm^2
structure	• zinc-blende • homogeneous single crystal • (111) surface orientation
PbTe	
SH response	< exp. detection limit
structure	• rock salt (centrosymmetric)

4.3.3 SHG in $Pb_{0.20}Cd_{0.80}Te$

Due to their different SH response, the SH image displayed in Fig. 3.22 clearly resolves the two different phases of the $Pb_xCd_{1-x}Te$ ternary alloy wafer in agreement with the SEM image in Fig. 3.16. The boundary between the Pb-rich and Cd-rich phases is marked by the red line in Fig. 3.22. They are discussed separately in the following.

4.3.3.1 SHG in the Pb-rich phase of $Pb_{0.20}Cd_{0.80}Te$

The SHG analysis of the Pb-rich phase of $Pb_{0.20}Cd_{0.80}Te$ confirms the morphological findings obtained by SEM. The weak to vanishing background SH signal found in most areas is related to the Pb-rich crystalline structure, which is expected to be similar to that of pure PbTe (rock salt) showing no dipole allowed SH response (section 4.3.2). The superposed random distribution of highly responsive grains is due to the Cd-rich microcrystallites embedded in the Pb-rich phase. The crystalline structure of these Cd-rich grains is similar to that of pure CdTe (zinc blende) showing a strong SH response (section 4.3.2). The grain size of the Cd-rich microcrystals is in the order of 10-50 μm.
The periodically alternating SH response observed in the high resolution SH image

Stellenbosch University http://scholar.sun.ac.za

in Fig. 3.23 (enlargement of the small red square in Fig.3.22) clearly reflects the superlattice structure formed by the layer-by-layer arrangement of the two phases. The periodicity occurs on a $\sim 10\ \mu$m length scale, making this material system an interesting candidate for a variety of technological applications in the field of nonlinear optics.

4.3.3.2 SHG in the Cd-rich phase of $Pb_{0.20}Cd_{0.80}Te$

The SH response of the Cd-rich phase seen on the right hand side in Fig. 3.22 shows a surprising feature. In contrast to the uniform morphology found by SEM (Fig. 3.16), large coherent areas within the Cd-rich phase are observed with both, weak to vanishing as well as strong SH response. Differences in the composition of these different areas as well as the presence of large Pb-rich regions in the Cd-rich phase can be excluded looking at the SEM image in Fig. 3.16. Hence it can be assumed that the composition (Pb content) is approximately uniform throughout the Cd-rich regions. The phenomenon of two apparently distinct Cd-rich areas is explained by the following interpretation of the SH images recorded at different azimuthal angles and polarization combinations.

Fig. 3.24 (a) is an enlargement of the area marked by the large red square in Fig. 3.22. The identical area is recorded in the SH image in Fig. 3.24 (b) at an azimuthal angle rotated by 30.6° with respect to (a). Regions characterized by a strong SH response before the rotation (Cd-rich I) show a weak to vanishing SH response after the rotation, and vice versa (Cd-rich II). The respective maximum signal heights are approximately equal. Hence, it is stated that two large coherent Cd-rich areas occur, which enclose an azimuthal SH phase shift of approximately 30°. This leads to the interpretation that two large crystalline grains (several mm^2) are present, which are characterized by equal Cd-rich compositions, but different crystalline orientations.

This interpretation is further supported by the results obtained by SH imaging using different polarization combinations. Fig. 3.25 (a) shows an enlargement of the area marked by the red square in Fig. 3.24 (a), which is recorded with (p-p) polarization. The SH image in Fig. 3.24 (b) shows the identical sample area recorded in the (p-s) polarization combination. Again, areas with weak to vanishing SH response in (a) show a strong SH response in (b), indicating the SH phase shift. As seen in the SH anisotropy curves of CdTe (Fig. 3.21) an azimuthal phase shift of exactly 30° would imply an exact transition from an azimuthal maximum to a minimum under change from (p-p) to (p-s) polarization. Hence, the fact the SH signal does not vanish completely in the (p-s) polarization combination in Fig. 3.24 is a sign that

Stellenbosch University http://scholar.sun.ac.za

the phase shift deviates slightly, but lies close to the value of 30°. Laue diagrams of $Pb_{0.20}Cd_{0.80}Te$ wafers recorded by x-ray diffraction revealed two dominant crystal orientations in the Cd-rich phase [75], namely (111) and (411). These two crystal faces enclose an angle of approximately 34°. Therefore, the two coherent regions enclosing the ~ 30 ° azimuthal SH phase shift are identified as large area grains of the (111) and (411) growth orientations. Due to the observed abundance, it is assumed that the region Cd-rich I represents the (111) orientation, whereas Cd-rich II shows a (411) oriented grain.

In addition to this, it is observed that the maximum SH signal heights in the Cd-rich phase are reduced by ~ 30 % compared to pure CdTe (Fig. 3.20) yielding the conclusion that the incorporation of Pb atoms (1-4 % within the Cd-rich phase) leads to a decrease of the SH conversion efficiency by ~ 30 %.

Table 4.4 summarizes the results and interpretations of the SHG analysis of $Pb_{0.20}Cd_{0.80}Te$.

TABLE 4.4: Summary: SHG analysis of $Pb_{0.20}Cd_{0.80}Te$ wafers grown be the vertical Bridgman method segregating into Pb-rich and Cd-rich phases.

Pb-rich phase	
composition	$Pb_{0.96-0.97}Cd_{0.03-0.04}Te$
SH response	weak to vanishing
structure	• rock salt • embedded Cd-rich microcrystals (10-50 μm) • superlattice structure on ~ 10 μm scale (for low cooling rates): → layer-by-layer accomodation of Pb-rich and Cd-rich phases → periodically alternating SH response
Cd-rich phase	
composition	$Pb_{0.01-0.04}Cd_{0.96-0.99}Te$
SH response	~ 30 % weaker than in pure CdTe
structure	• zinc blende • large coherent areas enclosing $\sim 30°$ azimuthal SH phase shift → macroscopic grains (several mm^2) of: (111) growth direction (411) growth direction

Stellenbosch University http://scholar.sun.ac.za

Summary and Conclusions

In this dissertation optical second harmonic generation (SHG) is employed to probe the structural and morphological properties of the three technologically relevant compound semiconductor sample materials SiC, ZnO and $Pb_xCd_{1-x}Te$. The experimental setup for the SHG experiments was developed during the course of this work. It employes a commercial Ti:Sapphire laser oscillator emitting femtosecond laser pulses, the characteristic parameters of which (782.8 nm, (75 ± 5) fs, 10 nJ, 80 MHz, TEM_{00}) are measured using a beam diagnostics setup including a custom-built autocorrelator. The setup involves fully computer automated data acquisition as well as lock-in-amplification to achieve an optimum signal-to-noise ratio. The second harmonic (SH) intensity generated in a reflection geometry by the interaction of the respective sample material with the intense femtosecond laser pulses is measured as a function of the azimuthal sample orientation (rotational SH anisotropy) as well as the translational sample position (SH imaging).

The SHG analysis of SiC thin films grown by chemical vapour deposition on silicon proves suitable for polytype recognition. Polarization resolved rotational SH anisotropy measurements unambiguously identify the SiC films to be the 3C-SiC polytype with zinc blende type crystal structure (cubic stacking order) and (100) surface orientation. SH imaging shows the homogeneous single-crystalline quality of the investigated SiC layers. The results are consistent with the recent literature and are viewed as a successful confirmation of the full functionality of the SHG setup developed and realized as part of this work.

As a second material system, ZnO thin films grown by metal organic chemical vapour deposition on three different substrate materials (silicon, glass, gallium arsenide) are studied by SH imaging, representing a novel approach in this context. It is found that all ZnO thin films grown under equal growth condition show very similar polycrystalline structures irrespective of the employed substrate material. The typical grain size of the deposited ZnO crystallites amounts to 20-50 μm. Furthermore, all films show an increasing SH signal amplitude with increasing average film thickness

Stellenbosch University http://scholar.sun.ac.za

(1, 5 and10 μm) confirming that SHG is a volume effect in ZnO.
The SHG analysis of ZnO films deposited within varying growth times (30, 150 and 300 min) on crystalline silicon of (100) surface orientation yielding different average thicknesses (1, 5 and 10 μm) indicate that, in the early stages of the growth process, isolated microcrystals are randomly deposited on the substrate surface. These are assumed to act as seeds for the further deposition process resulting in a complete substrate coverage. The structural film quality and homogeneity change very little for different thicknesses and remain polycrystalline. The efficiency of the MOCVD growth process is found to be higher on the right hand side of the substrate, which is related to the geometry of the employed growth reactor tube.
The ZnO films grown on amorphous glass substrates appear to have a similar polycrystalline structure and equivalent grain sizes as the ZnO layers deposited on silicon. No major differences in the progression of the deposition process are observed.
Despite obvious differences in lattice mismatch as well as crystal structure the ZnO films deposited on gallium arsenide of (100) surface orientation again show a polycrystalline structure comparable to that observed with silicon as well as glass substrates. However, the comparison of SH images recorded before and after the ZnO layer growth yields the observation that in certain sample areas the SH signal arising from the gallium arsenide substrate is suppressed due to the deposited ZnO film. It is suggested that, here, the gas phase reaction during the MOCVD process is not satisfactorily completed and amorphous particles are deposited, which have light absorbing properties affecting the SHG process.

The third material system for the first time investigated here by SHG is the ternary alloy $Pb_xCd_{1-x}Te$, which is grown as bulk material by the vertical Bridgman method, cut perpendicularly into wafers and polished. SH imaging resolves the segregation of the alloy into two different crystalline phases consistent with results obtained by scanning electron microscopy (SEM). From SHG measurements performed with the underlying binary compounds CdTe and PbTe it is concluded that the Cd-rich phase dominates the SH response of the $Pb_{0.20}Cd_{0.80}Te$ ternary alloy. It is found that a net incorporation of 1-4% Pb atoms into the CdTe lattice yielding the Cd-rich phase ($Pb_{0.01-0.04}Cd_{0.96-0.99}Te$) results in a reduction of the SH conversion efficiency by $\sim$ 30% compared to pure CdTe. The SH response of the Pb-rich phase is at least two orders of magintude weaker, which is rationalized by the centrosymmetric crystalline structure of PbTe.
Within the Pb-rich phase of the ternary alloy embedded microcrystals (10-50 μm) of Cd-rich composition are visualized by SH imaging consistent with SEM. The formation of these microcrystals is related to the supercooling in the PbTe phase

Stellenbosch University http://scholar.sun.ac.za

during the cooling down process with PbTe acting as solvent for CdTe yielding the crystallization of facetted Cd-rich microcrystals. In the case of slow cooling rates (2°C/h) in some areas of the Pb-rich phase a periodically alternating SH response is observed. This phenomenon occurs on a $\sim 10\ \mu$m length scale and is attributed to a regular layer-by-layer accommodation of the Pb-rich and Cd-rich phases caused by the coalescence of the Cd-rich microcrystals embedded in the Pb-rich phase. This feature makes $Pb_xCd_{1-x}Te$ an interesting material system for technological applications in the field of nonlinear optics.
SH imaging at different azimuthal angles as well as different polarization combinations resolves macroscopic coherent regions (several mm^2) within the Cd-rich phase of the ternary alloy, which show equal composition but enclose an azimuthal SH phase shift of approximately 30°. These regions are attributed to Cd-rich large area grains of (111) and (411) growth orientations. SHG, hence, proves suitable to obtain spatially resolved mappings of the wafer surface, which are not only sensitive to the sample composition, but also to the crystalline orientation.

Overall, this dissertation demonstrates optical second harmonic generation as a non-destructive, powerful and versatile tool to investigate semiconductor thin films as well as semiconductor wafers. Detailed, spatially resolved information is obtained about the growth process and the structural, morphological as well as nonlinear optical properties of the compound semiconductor materials SiC, ZnO and $Pb_xCd_{1-x}Te$ [84, 88, 100, 101], all of which are of great technological relevance in fields such as high power electronics, light emitting devices, or photovoltaics.

Stellenbosch University http://scholar.sun.ac.za

Outlook

The results and interpretations presented in this work stimulate a number of interesting new questions and ideas with the potential for further experimental investigations. These, on the one hand, concern the specific material systems and growth processes investigated here and, on the other hand, open up wide fields of applications for SHG not only in the sector of semiconductor research, but also in fields such as chemistry or life science.

With SHG employed as a diagnostical tool to probe the structural quality of thin films, the optimization of the MOCVD growth of ZnO layers is an interesting challenge. The large number of growth parameters, such as substrate material and temperature, different precursor gases and flow rates, or the VI:II ratio open up a wide spectrum of investigations striving towards the goal of single-crystalline deposition of epitaxial ZnO layers of various thicknesses and well defined growth orientations. Furthermore, SHG has *in situ* capability and is, therefore, suitable to provide online feedback during the growth process. On the basis of the results obtained here, the direct implementation and combination of SHG techniques with the MOCVD film growth process is suggested for further studies as a powerful approach to achieve ideal film quality. In addition, comparative SHG studies of ZnO layers produced by other techniques, such as pulsed laser deposition (PLD), which is available at the Laser Research Institute Stellenbosch, are proposed and promise further valuable information for the development of optimum quality ZnO thin films.

The ability of SHG to non-destructively generate spatially resolved mappings of thin film samples as well as wafer surfaces, which not only visualize the composition, but also the growth direction of the material, opens up a variety of applications in the fields of semiconductor growth, technology and quality control. The method is not restricted to the example of $\mathrm{Pb_xCd_{1-x}Te}$ ternary alloys studied here, but shows the potential to become an important diagnostical tool in the development of a variety of novel material systems, including organic media, for opto-electronic applications.

Apart from crystalline films and solids, gas-solid and liquid-solid boundaries are

Stellenbosch University http://scholar.sun.ac.za

also accessible by SHG. Interesting challenges are the detailed investigation of surface chemical reactions or the study of biological samples, such as cell membranes. Time resolved methods allow to probe microscopic processes on the ultrashort time scale, and the combination of nonlinear femtosecond laser spectroscopy and confocal microscopy, both available at the Laser Research Institute Stellenbosch, open up enormous research opportunities. SHG is, thus, a powerful diagnostical tool stimulating novel approaches in a variety of cross-disciplinary research endeavors positioned between materials science, physics, chemistry and life science.

Stellenbosch University http://scholar.sun.ac.za

Bibliography

[1] J. Bardeen, Phys. Rev. **71**, 717, 1947

[2] W. H. Brattain, W. Shockley, Phys. Rev. **72**, 345, 1947

[3] W. H. Brattain, Phys. Rev. **72**, 345, 1947

[4] J. Bardeen, W. H. Brattain, Phys. Rev. **74**, 230, 1948

[5] W. H. Brattain, J. Bardeen, Phys. Rev. **74**, 231, 1948

[6] M. Göppert-Mayer, Ann. Phys. (Leipzig) **9**, 273, 1931

[7] P. A. Franken, A. E. Hill, C. V. Peters, G. Weinrich, Phys. Rev. Lett. **7**, 118, 1961

[8] L. J. Simpson, T. E. Futak, J. Electroanal. Chem. **500**, 163, 2001

[9] C. Schwab, G. Meister, J. Woll, A. Gerlach, A. Goldmann, Surf. Sci. **457**, 273, 2000

[10] C. Schwab, G. Meister, A. Goldmann, E. Bertel, Surf. Sci. **469**, 93, 2000

[11] V. I. Gavrilenko, F. Rebentrost, Surf. Sci. **331-333**, 1355, 1995

[12] T. Kimura, C. Yamada, J. Cryst. Growth **150**, 92, 1995

[13] C. Yamada, T. Kimura, Phys. Rev. Lett. **70**, 2344, 1993

[14] M. Watai, H. Hirayama, Phys. Rev. B **72**, 085435, 2005

[15] T. G. Pedersen, K. Pedersen, T. B. Kristensen, Phys. Rev. B **61**, 10255, 2000

[16] K. Pedersen, T. B. Kristensen, T. G. Pedersen, P. Morgen, Z. Li, S. V. Hoffmann, Surf. Sci. **482-485**, 735, 2001

Stellenbosch University http://scholar.sun.ac.za

[17] T. Brunhes, P. Boucaud, S. Sauvage, A. Lemaître, J.-M. Gérard, V. Thierry-Mieg, F. Glotin, R. Prazeres, J.-M. Ortega, Physica E **7**, 155, 2000

[18] C. T. Williams, D. A. Beattie, Surf. Sci. **500**, 545, 2002

[19] O. A. Aktsipetrov, A. A. Fedyanin, E. D. Mishina, A. N. Rubtsov, C. W. van Hasselt, M. A. C. Devillers, T. Rasing, Surf. Sci. **352-354**, 1033, 1996

[20] J. G. Mihaychuk, N. Shamir, H. M. van Driel, Phys. Rev. B **59**, 2164, 1999

[21] G. Lüpke, Surf. Sci. Rep. **35**, 75, 1999

[22] Y. R. Shen *The Principles of Nonlinear Optics*, Wiley, New York, 1984

[23] C. Jordan, H. Schillinger, L. Dressler, S. Karmann, W. Richter, K. Goetz, G. Marowsky, R. Sauerbrey, Appl. Phys. A **65**, 251, 1997

[24] J. D. Jackson, *Classical Electrodynamics*, 3rd edition, Wiley, New York, 1999

[25] R. W. Boyd, *Nonlinear Optics*, Academic Press London, 1992

[26] P. F. Brevet, *Surface Second Harmonic Generation*, Presses Polytechniques et Universitaires Romandes, Lausanne, 1997.

[27] C. Rauscher, *Transiente Infrarot-Spektroskopie an wasserstoffverbrückten Flüssigkeiten mit Sub-Pikosekunden Zeitauflösung*, Dissertation, Technische Universität München 1997

[28] J. E. Midwinter, J. Warner, Brit. J. Appl. Phys. **16**, 1135, 1965

[29] M. J. Buerger, *Elementary Crystallography*, Wiley, New York, 1963

[30] N. Butcher, *Nonlinear Optical Phenomena*, Ohio State University, 1965

[31] M. Bloembergen, P. S. Pershan, Phys. Rev. **128**, 606, 1962

[32] B. Koopmans, F. van der Woude, G. A. Sawatzky, Phys. Rev. B **46**, 12780, 1992

[33] P. D. Maker, R. W. Terhune, M. Nisenoff, C. M. Savage, Phys. Rev. Lett, **8**, 21, 1962

Stellenbosch University http://scholar.sun.ac.za

[34] D. J. Bottomley, G. Lüpke, J. G. Mihaychuk, H. M. van Driel, J. Appl. Phys. **74**, 6072, 1993

[35] G. Lüpke, D. J. Bottomley, H. M. van Driel, J. Opt. Soc. Am. B, **11**, 33, 1994

[36] J. E. Sipe, D. J. Moss, H. M. van Driel, Phys. Rev. B **35**, 1129, 1987

[37] C. Yamada, T. Kimura, Phys. Rev. B **49**, 14372, 1994

[38] P. F. Moulton, J. Opt. Soc. Am. B **3**, 125, 1986

[39] U. Morgner, F. X. Kärtner, S. H. Cho, H. A. Haus, J. G. Fujimoto, E. P. Ippen, V. Scheuer, G. Angelow, T. Tschudi, Opt. Lett **24**, 411, 1999

[40] M. Nisoli, S. De Silvestri, O. Svelto, R. Szipöcs, K. Ferencz, Ch. Spielmann, S. Sartania, F. Krausz, Opt. Lett. **22**, 522, 1997

[41] T. Brabec, Ch. Spielmann, P. F. Curley, F. Krausz, Opt Lett. **17**, 1292, 1992

[42] A. Yariv, *Quantum Electronic*, Wiley, New York, 1989

[43] A. Brodschelm, *Amplituden- und phasenaufgelöste Femtosekundenspektroskopie im mittleren Infrarot: Hochfeldtransport in Galliumarsenid und Silizium*, Doktorarbeit, Technische Universität München, Germany, 2003

[44] T. Feurer, A. Glass, R. Sauerbrey, Appl. Phys. B **56**, 295, 1997

[45] A. Thaller, A. Brodschelm, M. Lettenberger,*Fitclient, Fithelper*, Private Communications, 2001

[46] P. W. Milonni, J. H. Eberly, *Lasers*, Wiley & sons, New York, 1988

[47] S. Niedermeyer, H. Schillinger, R. Sauerbrey, B. Adolph, F. Bechstedt, Appl. Phys. Lett. **75**, 618, 1999

[48] F. Kühnlenz, *Untersuchungen von SiC-Oberflächen und -Schichten mittels nichtlinear-optischer Frequenzverdopplung*, Diplomarbeit, Friedrich-Schiller-Universität Jena, Germany, 1999

[49] C. Meyer, G. Lüpke, E. Stein von Kamienski, A. Gölz, H. Kurz, Appl. Phys. Lett. **69**, 2243, 1996

Stellenbosch University http://scholar.sun.ac.za

[50] J. Q. Hu, X. L. Ma, Z. Y. Xie, N. B. Wong, C. S. Lee, S. T. Lee, Chem. Phys. Lett. **344**, 97, 2001

[51] C. Kirchner, Th. Gruber, F. Reuß, K. Thonke, A. Waag, Ch. Gießen, M. Heuken, J. Cryst. Growth **248**, 20, 2003

[52] D. M. Bagnall, Y. F. Chen, Z. Zhu, T. Yao, S. Koyama, M. Y. Shen, T. Goto, Appl. Phys. Lett. **70**, 2230, 1997

[53] Z. K. Tang, G. K. L. Wong, P. Yu, M. Kawasaki, A. Ohtomo, H. Koinuma, Y. Segawa, Appl. Phys. Lett. **72**, 3270, 1998

[54] A. Mitra, R. K. Thareja, Appl. Phys. Lett. **89**, 2025, 2001

[55] D. M. Bagnall, Y. F. Chen, M. Y. Shen, Z. Zhu, T. Goto, T. Yao, J. Cryst. Growth **184/185**, 605, 1998

[56] A. Mitra, R. K. Thareja, V. Ganesan, A. Gupta, P. K. Sahoo, V. N. Kulkarni, Appl. Surf. Sci. **174**, 232, 2001

[57] Y. Yamamoto, G.-H. Lee, K. Matsuda, T. Shimizu, M. Kourogi, M. Ohtsu, Opt. Review **7**, 486, 2000

[58] D. Xu, Z. Deng, Y. Xu, J. Xiao, C. Liang, Z. Pei, C. Sun, Physics Letters A **346**, 148, 2005

[59] H. Gomez, A. Maldonado, M. de la L. Olvera, D. R. Acosta, Solar Energy Materials & Solar Cells **87**, 107, 2005

[60] T. Ootsuka, Z. Liu, M. Osamura, Y. Fukuzawa, R. Kuroda, Y. Suzuki, N. Otogawa, T. Mise, S. Wang, Y. Hoshimo *et al.*, This Solid Films **476**, 30, 2005

[61] K. Keis, L. Vayssieres, S.-E. Lindquist, A. Hagfeldt, NanoStructured Materials **12**, 487, 1999

[62] K. Keis, E. Magnusson, H. Lindström, S.-E. Lindquist, A. Hagfeldt, Solar Energy Materials & Solar Cells **73**, 51, 2002

[63] H. Iechi, M. Sakai, K. Nakamura, M. Iizuka, M. Nakamura, K. Kudo, Synthetic Metals **154**, 149, 2005

[64] H. Kim, J. S. Horwitz, W. H. Kim, A. J. Mäkinen, Z. H. Kafafi, D. B. Chrisey, Thin Solid Films **420-421**, 539, 2002

Stellenbosch University http://scholar.sun.ac.za

[65] H. Agura, A. Suzuki, T. Matsushita, T. Aoki, M. Okuda, Thin Solid Films **445**, 263, 2003

[66] S. S. Kim, B.-T. Lee, Thin Solid Films **446**, 307, 2004

[67] Y. Nakata, T. Okada, M. Maeda, Appl. Surf. Sci. **197-198**, 368, 2002

[68] V. Craciun, J. Elders, J. G. E. Gardeniers, J. Geretovsky, I. W. Boyd, Thin Solid Films **259**, 1, 1995

[69] K. Ramamoorthy, C. Sanjeeviraja, M. Jayachandran, K. Sankaranarayanan, P. Misra, L. M. Kukreja, Mat. Chem. Phys. **84**, 14, 2004

[70] I. Ohkubo, A. Ohtomo, T. Ohnishi, Y. Mastumoto, H. Koinuma, M. Kawasaki, Surf. Sci. **443**, L1043, 1999

[71] Z. Fu, B. Lin, J. Zu, Thin Solid Films **402**, 302, 2002

[72] H. Yuan, Y. Zhang, J. Cryst. Growth **263**, 119, 2004

[73] O. Pagni, A. W. R. Leitch, phys. stat. sol. (a), **201**, 2213, 2004

[74] N. G. Dhere, AIP Conf. Proc. **401**, 423, 1997

[75] E. Saucedo, L. Fornaro, V. Corrigedor, E. Diéguez, Eur. Phys. J. Appl. Phys. **27**, 427, 2004

[76] E. Saucedo, V. Corregidor, L. Fornaro, N. V. Sochinskii, J. Silveira, E. Diéguez, Eur. Phys. J. Appl. Phys. **27**, 207, 2004

[77] T. O. Sedgwick, H. Lydtin (Editors), *Proceedings of the 7th international conference on Chemical Vapour deposition*, Electrochemical Society, Princeton, New Jersey, 1979

[78] D. Bäuerle, *Laser Processing and Chemistry* 2nd edition, Springer, Berlin, 1996

[79] P. Rudolph, A. Engel, I. Schentke, A. Grochocki, J. Cryst. Growth **147**, 297, 1995

[80] P. Rudolph, Prog. Cryst. Growth Charact. Mater. **29**, 275, 1994

[81] H. W. K. Tom, T. F. Heinz, Y. R. Shen, Phys. Rev. Lett. **51**, 1983, 1983

Stellenbosch University http://scholar.sun.ac.za

[82] T. Scheidt, E. G. Rohwer, H. M. von Bergmann, H. Stafast, Phys. Rev. B **69**, 165314, 2004

[83] Z. H. Dughaish, Physica B **322**, 205, 2002

[84] T. Scheidt, E. G. Rohwer, H. M. von Bergmann, H. Stafast, Eur. Phys. J. Appl. Phys. **27**, 393, 2004

[85] H. Cao, J. Y. Wu, H. C. Ong, J. Y. Dai, R. P. H. Chang, Appl. Phys. Lett. **73**, 572, 1998

[86] A. Mitra, R. K. Thareja, Modern Physics Letters B **15**, 515, 2001

[87] G. Wang, G. T. Kiehne, G. K. L. Wong, J. B. Ketterson, X. Liu, R. P. H. Chang, Appl. Phys. Lett. **80**, 401, 2002

[88] T. Scheidt, E. G. Rohwer, H. M. von Bergmann, H. Stafast, phys. stat. sol. (c) **1**, 2243, 2004

[89] H. Bach, N. Neuroth (Editors), *The Properties of optical glass*, Springer, 1998

[90] H. R. Philipp, E. A. Taft, Phys. Rev. **120**, 37, 1960

[91] J. R. Chelikowsky, M. L. Cohen, Phys. Rev. B **14**, 556, 1976

[92] C. Yamada, T. Kimura, Phys. Rev. Lett. 70, 2344, 1993

[93] Z. H. Levine, D. C. Allan, Phys. Rev. B 44, 12781, 1991

[94] Z. H. Levine, Phys. Rev. B 49, 4532, 1994

[95] H. Iwanaga, A. Tomizuka, N. Shibata, K. Mochizuki, J. Cryst. Growth **74**, 113, 1986

[96] G. H. Sherman, P. D. Coleman, J. Appl. Phys. **44**, 238, 1973

[97] M. S. Piltch, C. D. Cantrell, R. C. Sze, J. Appl. Phys. **47**, 3514, 1976

[98] J. Xu, G. M. H. Knippels, D. Oepts, A. F. G. van der Meer, Opt. Comm. **197**, 379, 2001

[99] L. E. A. Berlouis, A. Wark, F. R. Cruickshank, R. Antoine, P. Galletto, P. F. Brevet, H. H. Girault, S. C. Gupta, F. R. Chavada, A. K. Garg, J. Cryst. Growth **184/185**, 691, 1998

Stellenbosch University http://scholar.sun.ac.za

[100] T. Scheidt, E. G. Rohwer, H. M. von Bergmann, H. Stafast, J. Appl. Phys. **97**, 103104, 2005

[101] T. Scheidt, E. G. Rohwer, H. M. von Bergmann, H. Stafast, South African Journal of Science **101**, 267, 2005

Stellenbosch University http://scholar.sun.ac.za

Acknowledgements

My sincere thank goes to:

- Erich Rohwer and his wife Ingrid for everything they did for me.
- Hubertus von Bergmann for his support and the freedom and independence he allowed me.
- A. W. R. Leitch and O. Pagni for the fruitful collaboration, the discussions and the supply of the ZnO layers.
- Edgardo Saucedo and his colleagues from Spain and Uruguay for their support and the delivery of the PbCdTe wafers.
- H. Stafast for his help and support from Germany and the SiC test samples.
- Gillian Arendse for the good times, the moral support and the advice of a married man.
- the laser group and staff of the University of Stellenbsoch for their help, support and friendship, in particular: U. Deutschländer, Prof. P. Walters, C. Steinmann, C. Ruperti, P. Neethling, A. du Plessis, T. Gordon, S. Ombinda, T. Stehmann, M. Bartolini, J. Burns, B. Botha, W. Gauernack, D. Pool, S. February, F. Timmey, S. Peterson and G. Hillhouse.
- Andy Thaller and Andreas Brodschelm for the help from overseas.
- the *Deutscher Akademischer Austauschdienst (DAAD) e.V.* for the financial support.
- the South African National Laser Centre and the University of Stellenbosch for the project support.
- all my South African friends, particularly my housemates Aty and Cathy.
- my family, German friends and Anika.